COMPARISON OF SINGLE, DUAL AND TRIPLE FREQUENCY CYCLE-SLIP DETECTION METHODS FOR MULTI-GNSS

ÇOKLU-GNSS İÇİN TEK, ÇİFT VE ÜÇLÜ FREKANS FAZ KAYMASI BELİRLEME YÖNTEMLERİNİN KARŞILAŞTIRILMASI

AHMET AGAN

ASSOC. PROF. DR. METİN NOHUTCU
Supervisor

Submitted to

Graduate School of Science and Engineering of Hacettepe University

as a Partial Fulfillment to the Requirements

for the Award of the Degree of Master of Science

in Geomatics Engineering

2023

ABSTRACT

COMPARISON OF SINGLE, DUAL AND TRIPLE FREQUENCY CYCLE-SLIP DETECTION METHODS FOR MULTI-GNSS

Ahmet AGAN

Master of Science, Geomatics Engineering
Supervisor: Assoc. Prof. Dr. Metin NOHUTCU
September 2023, 131 pages

Global Navigation Satellite Systems (GNSS) is now widely recognized as a revolutionary invention in navigation and precise positioning on the Earth. The development of positioning systems from space, which started with GPS and continued with GLONASS, BeiDou and Galileo, has now been an area that serves billions of users with number of satellites over a hundred and increased number of signal frequencies. Everyone living on the earth expects the solutions to be brought to their problems to be fast and with high accuracy, along with the rapid progress of technology. When this is the case, GNSS needs to maximize its positioning and navigation skills day by day. Carrier-phase measurements are the key to achieve high precision and accuracy in GNSS positioning. Discontinuities in a receiver's phase lock on a satellite's signal, i.e., cycle slips, degrades positioning accuracy if they are not detected. Cycle-slip detection has become relatively easy due to the incorporation of new frequencies and modifications to many of the existing methods. With this study, a new software called Cycle Slip Methods Comparison Tool (CSMCT) was developed to comparatively analyze the performance of the selected single, double, and triple frequency cycle slip detection methods, and their performances were examined by categorizing the artificial cycle slips added to the observation data based on the satellite elevation angles using multi-GNSS. For the time being, there is no software capable of analyzing cycle-slip methods, including single, dual, and triple frequencies. Using the CSMCT software, it is possible to determine the success rates of the cycle-slip detection methods with the desired data and test scenarios, which sheds light on the selection of the appropriate method for different kinds of applications. By analyzing the obtained datasets, it has been determined that the cycle slip detection methods demonstrate high success rates under test conditions. For multi-GNSS, cycle-slip methods have been tested for single, dual and triple frequency observations, and the results obtained for triple-frequency are found to be the most successful.

Keywords: Cycle-Slip Detection, MATLAB, Multi-GNSS, Single-Frequency, Dual-Frequency, Triple-Frequency

ÖZET

ÇOKLU-GNSS İÇİN TEK, ÇİFT VE ÜÇLÜ FREKANS FAZ KAYMASI BELİRLEME YÖNTEMLERİNİN KARŞILAŞTIRILMASI

Ahmet AGAN

Yüksek Lisans, Geomatik Mühendisliği
Danışman: Doç. Dr. Metin NOHUTCU
Eylül 2023, 131 sayfa

Küresel Navigasyon Uydu Sistemleri (GNSS), navigasyon ve Dünya üzerinde hassas konumlandırma alanında devrim niteliğinde bir buluş olarak artık geniş çapta tanınmaktadır. GPS ile başlayan, GLONASS, BeiDou ve Galileo ile devam eden uzaydan konumlandırma sistemlerinin gelişimi, yüzün üzerinde uydu sayısı ve artan sinyal frekansları ile milyarlarca kullanıcıya hizmet veren bir ortam haline gelmiştir. Teknolojinin hızla ilerlemesiyle birlikte yeryüzünde yaşayan herkes, sorunlarına getirilecek çözümlerin hızlı ve yüksek doğrulukta olmasını beklemektedir. Durum böyle olunca GNSS'in konumlandırma ve navigasyon becerilerini her geçen gün daha yüksek düzeye çıkarması gerekmektedir. Taşıyıcı faz ölçümleri, GNSS konumlandırmasında yüksek hassasiyet ve doğruluk elde etmenin anahtarıdır. Alıcının uydu sinyali üzerindeki faz kilidindeki süreksizlikler, yani faz kaymaları, tespit edilmedikleri takdirde konumlandırma doğruluğunu azaltmaktadir. Faz kaymasının tespiti, yeni frekansların eklenmesi ve mevcut yöntemlerin çoğuna yapılan değişiklikler nedeniyle nispeten kolay hale gelmiştir. Bu çalışma ile seçilen tek, çift ve üç frekanslı faz kayması tespit yöntemlerinin performanslarının karşılaştırmalı olarak analiz edilmesi amacıyla Faz Kayması Yöntemleri Karşılaştırma Aracı (CSMCT) adı verilen yeni bir yazılım geliştirilmiş ve eklenen yapay faz kaymaları, çoklu-GNSS uydu yükseklik açılarına göre sınıflandırılarak performansları incelenmiştir. Şimdilik tek, ikili ve üçlü frekanslar dahil olmak üzere faz kayması yöntemlerini analiz edebilecek bir yazılım bulunmamaktadır. CSMCT yazılımı kullanılarak istenilen veriler ve test senaryoları ile faz kayması tespit yöntemlerinin başarı oranlarının belirlenmesi mümkün olmakta ve bu da farklı türdeki uygulamalar için uygun yöntemin seçimine ışık tutmaktadır. Elde edilen veri setleri analiz edilerek, faz kayması tespit yöntemlerinin test koşullarında yüksek başarı elde ettiği görülmüştür. Çoklu-GNSS için tek, çift ve üçlü frekans gözlemleri için faz kayması metotları test edilmiş ve üçlü frekans için elde edilen sonuçların en başarılı sonuçlar olduğu görülmektedir.

Anahtar Kelimeler: Faz-Kayması Tespiti, MATLAB, Çoklu-GNSS, Tek-Frekans, Çift-Frekans, Üçlü-Frekans

ACKNOWLEDGEMENTS

First and foremost, I would like to thank my advisor, Assoc. Prof. Dr. Metin NOHUTCU, who provided his full support under all circumstances during the long period of writing this thesis and who, with his patience and tolerance, never undervalued his trust in me. I would also like to thank the professors on my thesis committee who have maintained their faith in me.

I would like to express my gratitude to both my father, Mehmet Nezih AGAN, who instilled in me the conviction that I will eventually see the results of my efforts in this exhausting process, and to my uncle, Mustafa Melih AGAN, who assisted me with my requirements with a great deal of perseverance.

I would like to express my gratitude to my dear friend Gökberk YILDIRIM, who was very helpful to me by sharing his knowledge with me while I was working on the software development procedures for my thesis.

The study in this thesis was accomplished as an extension for the cycle-slip analyses within the project which was supported by TÜBİTAK (the Scientific and Technological Research Council of Turkey) under grant number 118Y410.

TABLE OF CONTENTS

LIST OF FIGURES

LIST OF TABLES

ABBREVIATIONS

ANTEX : **ANT**enna **EX**change Format

BDS : **B**ei**D**ou Navigation Satellite **S**ystem

C/A : **C**oarse / **A**cquisition

CDMA : **C**ode **D**ivision **M**ultiple **A**ccess

CSMCT : **C**ycle **S**lip **M**ethods **C**omparison **T**ool

DMA : **D**ivision **M**ultiple **A**ccess

DoD : **D**epartment **o**f **D**efense

EU : **E**uropean **U**nion

EWL : **E**xtra **W**ide **L**ane

FDMA : **F**requency **D**ivision **M**ultiple **A**ccess

GIOVE : **G**alileo **I**n-**O**rbit **V**alidation **E**lement

GLONASS : **GLO**balnaya **NA**vigatsiyonnaya **S**putnikovskaya **S**istema

GEO : **G**eosynchronous **E**quatorial **O**rbit

GF : **G**eometry **F**ree

GNSS : **G**lobal **N**avigation **S**atellite **S**ystem

GPS : **G**lobal **P**ositioning **S**ystem

GUIDE : **G**raphical **U**ser **I**nterface **D**esign **E**nvironment

Hz : **H**ertz

IGSO : **I**nclined **G**eo**S**ynchronous **O**rbit

ISF : **I**onospheric **S**cale **F**actor

LLI : **L**oss of **L**ock **I**ndicator

MATLAB : **MAT**rix **LAB**oratory

MWWL : **M**elbourne-**W**übbena **W**ide **L**ane

MEO : **M**edium **E**arth **O**rbit

NL : **N**arrow **L**ane

OS : **O**perating **S**ystem

P : **P**recise

PPP : **P**recise **P**oint **P**ositioning

PRN : **P**seudo-**R**andom **N**oise

PZ : **P**arametry **Z**emli

RAM	:	**R**andom **A**ccess **M**emory
RINEX	:	**R**eceiver **In**dependent **Ex**change **F**ormat
SGS	:	**S**oviet **G**eodetic **S**ystem
SNR	:	**S**ignal to **N**oise **R**atio
SP3	:	**S**tandard **P**roduct **3**
SSI	:	**S**ignal **S**trength **I**ndicator
TEC	:	**T**otal **E**lectron **C**ontent
UI	:	**U**ser **I**nterface
US	:	**U**nited **S**tates
USA	:	**U**nited **S**tates of **A**merica
USSR	:	**U**nited of **S**oviet **S**ocialist **R**epublics
WL	:	**W**ide **L**ane

1. INTRODUCTION

1.1. Thesis Background

After the construction of satellite-navigation systems together with the experiences of humanity in the space race, a period has started where many large-scale applications that take a very long time can be done within seconds. While technology is advancing at great speeds in every field, with Global Navigation Satellite Systems (GNSS), it has become sufficient to simply turn a receiver on and read the position information to learn the location of a person or a moving object. Also, with the enhancement of GNSS over time, the position accuracies have been gradually increased.

To achieve high GNSS accuracy, carrier-phase observations are imperative as these signals allow very precise measurements with their relatively much shorter wavelengths with respect to code measurements. Cycle-slips are one of the most significant sources of error in carrier-phase measurements, and they must, at least, be detected for any application that requires high level of positioning accuracy. Since the early years of GNSS, numerous studies have been conducted and numerous methods have been offered for cycle-slip detection, each with strengths and weaknesses. Even though their flaws have been recognized and attempted to be covered, the existing methods have not changed significantly over time. There are few studies which compared cycle-slip methods, where the number of methods included in these studies is limited. On the other hand, comparing the cycle-slip detection methods within the same test environment would help to have an idea of the correct methods to be used based on the GNSS application of choice. It has been recognized, however, that cycle-slip detection methods are still an open area for development.

1.2. Research Objectives

With the rapid advancements in GNSS over the past few years and the introduction of new frequencies that can be employed, major improvements have been made in the detection and elimination of cycle slips using combinations that can be created. The primary objective of this thesis is to investigate various single, dual, and triple frequency cycle-slip algorithms for multi-GNSS observations, compare various aspects of these methods, and assess the performance of the algorithms with artificially added cycle-slips. It is aimed that the artificial cycle-slips to be added will simulate the natural occurrence of this error. For testing the algorithms, the elevation angles of the satellites in the GNSS constellations will be considered. In addition, it is aimed to perform the operations in post-processing environment.

A MATLAB based software is aimed to be developed to accomplish the related analysis through a user-interface and parameters selected by the user. By adding artificial cycle-slips with defined amplitudes to specific epochs of the observation arcs, which will be obtained from real RINEX observation files required for the program to run, it will be determined how many cycle-slips the algorithms correctly identify. This is done to demonstrate the overall performance of the algorithms and to assist GNSS users for the selection of the proper cycle-slip method for their applications. Priority will be placed on providing all results with percentage-based accuracy values.

A comparison tool capable of performing all the operations mentioned above was seen as a deficiency and it is thought that creating an environment that can provide analysis with high accuracy would contribute to the GNSS community. Besides, as an extension to this study, it is intended to develop a software for real-time cycle slip detection, as these analyses are desired to be obtained instantly and with high precision in many GNSS applications.

1.3. Thesis Outline

In this thesis, explanations will be made from general to specific within six chapters. The first chapter includes the motivation of the study besides the scope of the topics to be covered in the thesis.

In Chapter 2, information will be given regarding the history of GNSS constellations, the primary characteristics of each navigation system, and the number of satellites in each block. Additionally, the frequencies of each GNSS constellation are provided in detail. In general, the signal structure is specified because the majority of cycle-slip detection methods rely on data combinations. Since signal frequencies are utilized in each of these data combinations, they are added in table format. In addition, details about the most common GNSS data combinations will be given. The advantages and disadvantages of the most widely used combinations in cycle-slip detection methods are described. In addition, information is given regarding the contribution of data combinations to prevent satellite-clock errors, one of the most significant GNSS errors, enhancing position accuracy by minimizing errors caused by atmospheric delays. Systematic and non-systematic errors of GNSS are also discussed. Brief information was given about the sources of errors, and evaluations were conducted to determine if and to what extent they contributed to the possibility of the occurrence of cycle slip.

In Chapter 3, comprehensive information is given about what the cycle-slips are, since it is the special topic of the thesis. The underlying reasons for their occurrence, and the methods developed for detecting cycle-slips are described in detail. In addition, each method is categorized as single, dual, and triple-frequency detection methods and the detection processes with necessary thresholds for identifying them are described in general terms.

In Chapter 4, the cycle-slip detection methods and software developed to make easier the analysis processes are described in detail. Furthermore, it is explained how the data is stored and shared in the application, and how the software reaches the parameters related to cycle-slip detections based on the information in these data formats. The data processing stages of the software are labeled as file import, parameter selection, method selection, cycle-slip insertion, and analysis, with each step explained in detail. Screenshots of the developed software are also included.

In Chapter 5, a description of the data that was used in the case-study is presented. The most used single, dual, and triple-frequency methods were compared with each other. With the software, the results obtained as a result of the comparison of the cycle slip detection methods with each other and the success rates of the algorithm made in the detection of artificial cycle slips added are shown.

In Chapter 6, the information gathered about the advantages and disadvantages of the existing algorithms and the conformity of the results obtained in Chapter 5 with the results of the studies conducted in this field were examined. It also includes suggestions for improving the results obtained in the case study, as well as ideas that will enable those dealing with cycle-slip detection to get preliminary information about the steps in their projects before their work. With that, the last chapter states the summary of the thesis and future recommendations.

2. GLOBAL NAVIGATION SATELLITE SYSTEMS

GNSS, as one of the most important systems of our time has opened a new era in geodesy and navigation, and it has taken a huge workload from most business lines. With the great progress of GPS in the recent past and the modernization of the system, and with the activation of other GNSS constellations, significant progress has been made in the precision of applications in many different branches and solutions for error sources. Since it is the oldest satellite navigation system and a lot of research has been done on it for half a century, it can be easily said that the output source of the majority of technical solutions related to GNSS systems is GPS. Since the contents of other systems are similar to GPS, the main concepts will be presented in the following section.

2.1. GPS

2.1.1. History of the GPS

In 1973, the U.S. Department of Defense (DoD) issued a directive to establish a satellite-based positioning system, which led to the development and planning of the Global Positioning System (GPS). Since then, GPS has been continuously modernized and made accessible all over the world, and it has become an indispensable component of our daily lives [1]. In this context, the first GPS satellite was launched into orbit in 1978, and the remaining satellites of the first generation were deployed into space and successfully installed over the next seven years [2]. After the first generation of satellites began its operations, efforts continued toward the objective of launching the second and third generations into orbit and making the system accessible worldwide. As of 2023, the first block satellites have completed their lives and except for the second-generation satellites that have been decommissioned, the second and third block satellites continue to provide service.

2.1.2. Main Features of GPS

GPS operates by determining the locations of satellites sent into orbit and the coordinates of receivers acquired by users on Earth. The system offers high accuracy information on the location, time, and navigation of military and civilian users in the air, at sea, and land around the world [3]. The primary objective is to guarantee that the system can be utilized actively 24 hours a day, without interruption, as weather independent as possible, and that the user's receiver can view at least four satellites regardless of their location on Earth.

The United States (US) manages this first successful satellite-based positioning system, which is divided into three different segments: the user segment, the space segment, and the control segment [4–6]. The user segment of GPS, which attained its worldwide usage capability in the early 1990s, was first restricted to the US military before being accessible to civil use. Later, GPS ceased to be a military-only system and became a system that was actively used by the entire world. After being made accessible for civilian usage, the user segment grew from tens of thousands to millions, and today it is utilized practically everywhere in the world by a population of billions. Currently, the space segment of this system consists of a total of 31 functional satellites which belong to three main generations, i.e., satellite blocks [2,7,8].

These satellites are used in a variety of devices for scientific and nonscientific applications alike. These satellites rotate at an inclination angle of 55° with the equator,at an average of 20200 km above the earth, and transmit their position information via electromagnetic signals [9].

Satellites orbit the Earth twice on each sidereal day [10,11]. Each satellite is launched into space with a predetermined lifespan, and these satellites are decommissioned at the end of their mission or if the data flow is interrupted. The organizations in charge are responsible for planning the replacement of decommissioned satellites with new satellites to maintain the system's continual operation.

The control segment is the component that performs crucial operations such as processing the signals received from the satellites in the space segment, making the necessary error corrections, ensuring that the system is not interrupted in any way, synchronizing the clocks, and transmitting the signals to the satellites. The control segment also contains multiple components. These include the master control station, monitoring stations, and the main control center located inside a military base in Colorado [12]. The main control center here is responsible for assuring operational functionality and maintaining the optimal performance of GPS, in addition to generating navigation signals. There are a total of 16 monitoring stations that collect the parameters necessary for the generation of navigation messages from the observation and atmospheric data of GPS satellites passing over them and transmitting this information to the main control center. After the data has been transmitted to the main control center for processing, the processed data is transmitted to the satellites through a total of 11 ground antennas. The number of GPS satellites in each block and their launch dates are expressed as:

2.2. GLONASS

The GLONASS satellite-based positioning system, whose Russian acronym corresponds to the English term GNSS, was developed by the United of Soviet Socialist Republics (USSR) [1,13]. GLONASS is known for being a system that is established by prioritizing military purposes. During the Cold War, the USSR, which competed with the United States in almost every field, developed its satellite positioning system to avoid falling behind militarily. Initially, the development process has progressed almost in conjunction with the GPS. In the 1970s, based on its experience in the space race, the USSR commenced the GLONASS project and launched the prototype satellites into space in 1982 [14].

GLONASS, which is designed to have a total of 24 satellites, accomplished this objective in 1996 and became globally accessible [15]. The system, which was unable to reach this objective before the disintegration of the USSR, remained regional for an additional two decades, as the number of satellites decreased and the structure of 24 satellites could not be maintained because Russia, which left the union, went through a very precarious financial period. With Russia’s financial recovery, the system was expanded as rapidly as possible to restore it, supported by the country’s federal budget wherever necessary, and by the end of 2011, it resumed its place as the second fully operational, global navigation and positioning system [16]. It is currently governed by the Russian Federation’s “Roskosmos” organization.

2.2.1. History of GLONASS

Having almost the same basic purposes as GPS, GLONASS sent its first non-prototype satellite in 1985 [11]. Its primary objective is to provide position information to any location on Earth, regardless of the equipment or vehicle being used, at any hour of the day, and with the least amount of weather interference. GLONASS used Soviet Geodetic System (SGS)-85 as its coordinate system, but 9 years later this system was replaced by the Parametri Zemli (PZ)-90 [17].

GLONASS, the second system that can successfully provide worldwide positioning services after GPS, is divided into 3 segments which are space, ground control and user. The space segment consists of 24 operational satellites and these satellites orbit 17 times every 8 sidereal days, in 3 orbital planes, with equal spacing in each orbital plane and with an inclination angle of 64.8° [18].

2.2.2. Main Features of GLONASS

The control segment of GLONASS is responsible for system operation and maintenance, error correction, satellite orbital calculations, time synchronization, and satellite launch [14]. Unlike GPS, GLONASS's ground control stations are not globally distributed. The vast majority of control stations are geographically dispersed across the Russian Federation's territory. Except for the Russian Federation, control units have been installed in South America, Antarctica, and Africa, and negotiations are ongoing with other nations to expand this number to the desired level, not falling below 40. The main GLONASS control center is responsible for nearly all tasks required for the functionality of the system to be executed and monitored. Among the main tasks of the GLONASS main control station are satellite telemetry monitoring, satellite health monitoring, satellite retirement, and the transmission of orbit and clock information to satellites [19]. GLONASS's control stations, like GPS stations, regularly send all the data they collect to GLONASS's main control station.

2.3. Galileo

2.3.1. History of Galileo

Galileo satellite-based navigation system was developed under the auspices of the European Union (EU). This system was developed and is being operated with contributions from all members of the EU [20]. It is named after the astronomer Galileo Galilei, who lived about five centuries ago.

When deciding to develop this system, the EU considered it not just as a positioning system, but also as a marketing tool. As a result of research, it has been determined that it can offer alternate solutions to a variety of problems. With the deployment of Galileo, positioning and navigation services, which satellite-based satellite systems have dominated and made more accessible in recent years, have become more potent.

Countries that developed different GNSS constellations were essentially focused on military applications and did not interact with other nations or agencies. In this regard, the Galileo system has a different strategy. A development plan was made for civilian users rather than military purposes. Access for civilian users of Galileo can only be restricted under extreme circumstances, such as when the EU would be at war.

As the EU intends to move forward in accordance with international rules and standards, the Galileo system has maintained close contact with satellite-based system owners. In the context of these circumstances, the EU has considered cooperating with both the United States and Russia. However, due to the security risks of the member states, the EU has decided to develop a system that is compatible with other systems, but can be operated in Europe independently of them [1].

2.3.2. Main Features of Galileo

While developing Galileo, the EU aimed for a system based on civil use, offering the highest possible location and navigation accuracy, and interacting with other GNSS constellations [21]. The Galileo system is directly related to nearly all of the EU’s economic activities, transportation infrastructure, and maritime activities. For this reason, the EU has designed the Galileo system for a long time, because even minor system interruptions have the potential to cause billions of Euros in damage across the entire union.

Galileo is designed to have a total of 24 primary satellites in three orbits, with 8 satellites in each orbit. Moreover, it is a system with a 56° angle of inclination and the spare satellites, on the other hand, are 6 in total and are positioned as 2 in each orbit [19]. With Galileo, the EU increased the number of satellites visible from any location on Earth simultaneously. This number, which is a minimum of four with GPS, can increase to 11 with Galileo and decrease to 6 at low elevation angles if categorized according to elevation angles (minimum 5°). With this orbital structure, both the costs and the time required to deploy new satellites are reduced.

The Galileo system has similar segments with GPS. There are space-based units, control and monitoring stations, and the user side. Galileo's satellites form the space segment of this constellation. The system currently has 23 usable satellites in total and is expected to increase both the current number of satellites and the lifetime of the satellites as the new generation satellites are being sent to orbit. If one of the satellites must be deactivated for whatever reason, such as cessation of the data flow or end of the duty-cycle, the satellites are taken from their orbits and relocated to a higher orbit, and a spare satellite is installed in the deactivated satellite's position.Unlike other GNSS constellations, the control segment's main control station consists of two control stations. One is located in Germany, while the other is in Italy. While a few of the telemetry stations are in Europe, the rest of them are situated on French-held island territories. In this way, in contrast to GLONASS, they spread globally.

2.4. BeiDou

2.4.1. History of BeiDou

Following the successful moves of the United States and Russian Federation in global navigation systems, the Chinese government has initiated plans to produce its system. In 1993, during the Yinhe Incident, Chinese authorities made attempts to develop an independent global positioning system for China when the United States shut down the

GPS in the maritime domain where the Yinhe container ship was situated, halting the ship's movement [22,23].

The Chinese government chose the moniker BeiDou for the independent satellite positioning system. This term is derived from the Big Dipper, which was utilized for decades to locate the North Star [24]. Although BeiDou was specifically developed for military services and regional use, it has since been expanded for civil use.

2.4.2. Main Features of BeiDou

In practice, the components of each stage of BeiDou's three-stage system have evolved. Similar to other GNSS constellations, the BeiDou system is composed of three segments. These segments are classified as ground, user, and space. In the ground segment, there are the main and secondary control stations that collect the satellite signals, as well as the management and sustainability centers. The BeiDou Navigation Satellite System, BDS system provides antennas, microchips, positioning services, and software for the user segment. The space segment is comprised of satellites in orbit and is classified as Geostationary Orbit (GEO), Medium Earth Orbit (MEO), and Inclined Geosynchronous Orbit (IGSO). The distribution of these satellites has been determined to be 5 GEO, 27 MEO, and 3 IGSO. It is anticipated that there will be a total of 35 of them. IGSO and MEO satellites have the same altitude and inclination angle, 35,786 kilometers and 55°, respectively [25,26]. MEO satellites are also at an altitude of 21500 km, and have an inclination angle of 55° [27]. BeiDou, or BDS (BeiDou Navigation Satellite System) as it is known, designed and started to implement a three-way plan from its inception until it was fully commissioned. These systems are named BeiDou-1, BeiDou-2, and BeiDou-3, and they serve regionally, Asia-Pacific Region, and worldwide, respectively. More details will be given briefly in the following subsections.

2.4.3. BeiDou-1 (Experimental)

As mentioned in Section 2.4.2, the BeiDou-1 system is the foundation upon which other advanced systems will be constructed as part of the Chinese government's program. BDS-1 was initially developed for military purposes, and it was not until the first few months of 2004 that it was made available for civilian use. BDS-1, whose first satellite was launched in 2000, became operational with the launch of the third satellite in the summer of 2003, including in China and some neighboring states [28,29]. These satellites were supported by two additional satellites that would be launched in subsequent years. The BDS-1 system, unlike other GNSS constellations, employs GEO satellites rather than MEO satellites.

The BeiDou-1 satellites are designated BeiDou 1A, BeiDou 1B, and BeiDou 1C, respectively, in alphabetical order [30]. The BDS-1 satellites were decommissioned at the end of 2011 and are no longer part of the system. Since the system's positioning accuracy was as low as 100m and its accuracy can only be increased by using Chinese calibration stations, it cannot serve as a substitute for modern systems [31].

2.4.4. BeiDou-2 (Extended)

BeiDou-2 began serving Chinese users and, by the end of 2012, also began serving the Pacific region. With BeiDou-2, which became fully operational at the end of 2012, China transitioned from geostationary satellites to a hybrid system by deploying satellites in three distinct orbits (IGSO, MEO, GEO) [32]. BeiDou-2, which was anticipated to be more accurate than BeiDou-1, consists of a total of 14 satellites. BeiDou-2 is designed to be compatible with other systems, and it aims to improve positioning precision by combining data from these systems. This reduced the accuracy to 10 meters. The satellites, with orbital altitudes of approximately 21,500 kilometers, are located between the orbits of GPS and Galileo [33]. The clocks on this system are atomic clocks with rubidium oscillators, and the system has been designed for global coverage.

2.4.5. BeiDou-3 (Global Coverage)

The Republic of China has expanded its satellite presence in space with the BeiDou-3 system, and one of the greatest benefits of this system is that the satellites can communicate with one another [34]. With these satellites of the latest generation, China has reduced the need for satellites to connect with terrestrial segments. With the BeiDou-3 system, it is now possible to transmit signals at a total of five different frequencies; this has led to significant improvements in positional accuracy and the elimination of observation-based errors for comprehensive analysis. BeiDou-3 satellites are also equipped with two distinct types of clocks: rubidium clocks from the previous system and hydrogen oscillator atomic clocks with the next generation. The total number of satellites is 30, with 24 MEO satellites, 3 GEO satellites, and 3 IGSO satellites [35,36]. The Chinese government has placed the majority of satellites of this generation into orbit at an astounding rate of three years.

2.5.GNSS Signal Structures

GNSS receivers detect and process the signals transmitted by the satellites via an antenna. Since GPS is the first and most widely used global positioning system, band selection will be explained using GPS as an example.

Also, a very important criterion is the determination of transmitted signals of the satellites. Consequently, the GPS's development has necessitated the selection of a specific signal band. The L-band in microwave size was selected because it satisfies more criteria than other bands. The most significant advantage of selecting the L-band is that it can reach the planet regardless of the weather. It is between 1 GHz and 10 GHz, a range where ionospheric factors do not have a significant impact, and it can be delivered to the receiver on earth with minimal signal degradation due to other atmospheric effects [11]. In addition, at frequencies much higher than the L band, mobile users will likely be at a significant performance disadvantage, as the antenna type (beam antenna) must be altered for civilian users to receive these signals.

Using two frequencies from this band, GPS satellites provide positioning services. By modulating navigation data and ranging code, however, carrier signals with only specific wavelengths are transformed into a package that can contain a great deal of information.

The Pseudo Random Noise (PRN) code is a series of randomly arranged binary (0-1) numbers, but since the receiver is aware of this random sequence, it is more accurate to refer to it as pseudo-random [37]. PRN codes are used to determine the length of time the signal spent traveling from the satellite transmitter to the receiver. The distance between the satellite and the receiver is determined by multiplying this time by the speed of light in a vacuum. In the literature, PRN codes are also known as range codes. Each GPS satellite has a unique PRN code generated with modulation technique known as Code Division Multiple Access (CDMA) [38].

Besides GPS, Galileo and BeiDou also use CDMA. This technique enables a single receiver to process multiple satellite signals, with each satellite having a unique PRN code. GLONASS employs the Frequency Division Multiple Access (FDMA) technique rather than the CDMA technique [39]. In the FDMA technique, each satellite’s PRN code is identical, but the frequencies are different.

GLONASS continues its efforts to change the different DMA method it currently employs and to use the same DMA structure with all modernized GNSS components [40]. The reason for this is that the components of FDMA-compatible receivers are more expensive than those of CDMA-compatible receivers. By employing CDMA with its new signals, GLONASS hopes to increase its compatibility with other GNSS constellations and avoid being less efficient with FDMA than with other techniques. The GNSS carrier-frequencies are listed in Table 2.1:

Table 2.1. GNSS Signal Structure

GNSS Signal Structure							
Carrier-Frequency (MHz)							
GPS		GLONASS		Galileo		BeiDou	
L1	1575.4200	G1	1602+k*9/16	E1	1575.420	B1	1575.420
L2	1227.6000	G1a	1600.995	E5	1191.795	B2a	1176.450
L3	1381.0500	G2	1246+k*7/16	E5a	1176.450	B2b	1207.140
L4	1379.9133	G2a	1248.06	E5b	1207.140	B2	1191.795
L5	1176.4500	G3	1202.03	E6	1278.750	B3	1268.520
MA-Technique							
CDMA		FDMA		CDMA		CDMA	
GNSS Time							
GPST		GLONASS Time		GST		BST	
GLONASS Slots (k)							
1, -4, 5, 6, 1, -4, 5, 6, -2, -7, 0, -1, -2, -7, 0, -1, 4, -3, 3, 2, 4, -3, 3, 2, 0, 0							

2.6. GNSS Observables

2.6.1. Code-Pseudorange Observables

In GNSS, a code-pseudorange observable is a measurement of the time delay between the transmission of a code sequence from the satellite and the reception of the same code sequence at the receiver. The code measurement is typically made by comparing the received code sequence to a locally generated replica of the code sequence at the receiver. The code measurement is typically made using a technique called cross-correlation.

The main reason why it is called pseudorange, not just range, is since this signal transmission time, which we multiplied by the speed of light constant, is not pure due to the errors in the clocks of both the receiver and the satellite [11]. The pseudorange CP can be expressed as:

$$CP = c(\Delta t) \tag{2.1}$$

where, c represents the speed of light constant in vacuum, Δt is the travel time of the signal. The accuracy of this distance is far from being acceptable. Even satellite and receiver clock errors result in distance errors for kilometers. In particular, the effect of receiver clock errors can be huge, if the receiver is not of good quality, a negative pseudorange may be obtained. Including the clock errors pseudorange equation can be written as:

$$CP = c\ ((t^{rec} + dt^{rec})\text{-}(t^{sat} + dt^{sat})) \tag{2.2}$$

where, c indicates the speed of light constant, t^{sat} is the emission time, dtsat represents the satellite clock, t^{rec} is the reception time and dtrec is the receiver clock error. Both satellite and receiver clocks must be in the relevant GNSS time scale. Assuming that the satellite transmits this signal at t^{sat} without error and the receiver receives this signal at trec without error, it will give us the true geometric distance.

If the previous equation is written with all the error sources affecting the GNSS code-pseudorange:

$$C_{P_{f_n}} = \rho + c(dt^{rec} + dt^{sat}) + Trop + a_{fn}TEC + \beta r_{P_{f_n}} - \beta s_{P_{f_n}} + M_{P_{f_n}} + E_{P_{f_n}} \tag{2.3}$$

where $CP_{L_{f_n}}$ is the code-pseudorange measurement, f is the signal frequency, n indicates the frequency number, ρ is the geometric distance between receiver and satellite, c is the speed of light constant, dt^{rec} is the receiver clock error, dt^{sat} is the satellite clock error, $Trop$ is the tropospheric delay, $a_{fn}TEC$ is the first-order ionospheric delay, $\beta r_{L_{f_n}}$ is the frequency-dependent delay due to on receiver hardware, $\beta s_{L_{f_n}}$ is the frequency-dependent delay due to satellite hardware delay and $M_{L_{f_n}}$ is the multipath delay. In the $E_{L_{f_n}}$ term, code measurement noise, relativity, ocean tides, solid ground tides, satellite and receiver antenna phase center variation can be added.

2.6.2. Carrier-Phase Observables

In the production phase of the signal, there is an electric field and a magnetic field valid for all electromagnetic waves. As the GNSS signal travels, there is both an electric field and a magnetic field around it. The relationship between the electric field and the magnetic field is evaluated according to the direction of rotation. If the vector of the electric field is traveling clockwise, the electromagnetic wave is called right-handed polarized, and if it travels in the opposite direction, it is called left-handed polarized.

The reason for using circular polarization in GNSS signals is that the signal passes through the ionosphere layer. A linearly polarized signal becomes circularly polarized as it passes through the ionosphere. Therefore, GNSS signals are sent in circularly polarized form from the very beginning. A general representation of an electromagnetic signal is given in Figure 2.1 [1]:

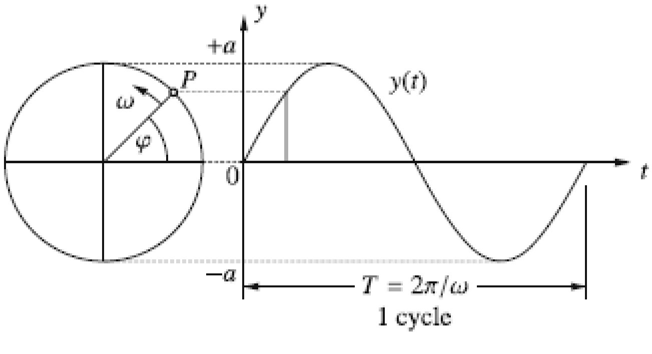

Figure 2.1. Representation of Electromagnetic Signal [1]

GNSS signals are obtained from the oscillation of the charged particle. Let us assume that the particle in the figure is P and that this particle belongs to the L1 frequency of GPS. In this case, we can say that this P particle rotates about 1.5 billion times in a second.

While GPS was in the planning phase, phase observations were not a work of purpose. It was later realized that the accuracy of code observations could be increased enormously by using phase observations as the chip length for the Coarse Acquisition (C/A) code is 293 meters, while the wavelength for the L1 carrier signal is approximately 19 cm [41]. It is known that the accuracy of these observations is %1 of wavelength, it is approximately 2.93 meters for C/A, and 1.9 cm for L1 carrier frequency signal. In other words, according to the precision that can be reached in code-pseudorange observation, it can be deduced that the precision of phase observations can be reduced to the level of millimeters. Just like in code-pseudorange observations, carrier-phase observables are also subject to various error sources. Most of the errors contained in both observations are similar, while carrier-phase measurements include additional error terms. The carrier-phase observations can be represented by the Equation 2.4:

$$\Lambda_{L_{f_n}}\phi_{L_{f_n}} = \rho + c(dt^{rec} + dt^{sat}) + Trop - a_{fn}TEC + \beta r_{L_{f_n}} - \beta s_{L_{f_n}} + \Lambda_{L_{f_n}}N_{L_{f_n}} + \Lambda_{L_{f_n}}w + M_{L_{f_n}} + E_{L_{f_n}} \quad (2.4)$$

where $\Lambda_{L_{f_n}}\phi_{L_{f_n}}$ is the carrier-phase measurement in meters, n is the signal frequency number, ρ is the geometric distance, c is the speed of light constant in vacuum, dt^{rec} is the receiver clock error, dt^{sat} is the satellite clock error, $Trop$ is the tropospheric delay, $a_{fn}TEC$ is the ionospheric delay, $\beta r_{L_{f_n}}$ is the receiver hardware delay, $\beta s_{L_{f_n}}$ is the satellite hardware delay, $\Lambda_{L_{f_n}}N_{L_{f_n}}$ is the integer ambiguity term in the unit of meters, $\Lambda_{L_{f_n}}w$ is the phase wind-up effect, $M_{L_{f_n}}$ is the carrier-phase multipath, and $E_{L_{f_n}}$ is the carrier-phase measurement noise. Each equation parameter where L_{f_n} term appears should be accepted as frequency dependent.

The most important term in the carrier-phase observation is the ambiguity term, which is the initially unknown number of full carrier cycles between the satellite and the receiver.

The process of solving this expression is called ambiguity resolution and many algorithms are used.

When an earth-based receiver is locked to any GNSS satellite, the phase observation is equal to the $N_{L_{f_n}}$ term in between. If we assume that the receiver’s lock to the satellite is not broken while the satellite is moving, the receiver can follow the phase difference resulting from this movement and counts it as a function of time. Since the $N_{L_{f_n}}$ term which is an unknown, will never change throughout the continuous observation arc of the GNSS satellite and the motion of the satellite can be obtained very precisely with the help of multiple phase observations. However, in case of any interruption (loss-of-lock), the continuous observation arc of the satellite is disrupted. The ambiguity term will be re-initialized when the receiver and satellite are locked again.

If the precision to be achieved is at the level of a few centimeters depending on the requirement of the GNSS application, carrier-phase measurement is so important that it is almost indispensable, otherwise it is not easy to achieve this precision. Therefore, all GNSS receivers used for geodetic applications can process phase observations.

2.7. GNSS Data Combinations

Combining the signals sent by the same satellite and processed within the same receiver during the same epochs is the process of producing different signals that are suitable for the intended purpose. Combinations of GNSS data are simple and primarily utilized to reduce or eliminate the sources of error mentioned before for carrier-phase and code-pseudorange measurements.

The purpose of creating combinations is to facilitate the computation of specific parameters or terms. These combinations vary for single, dual, and triple frequency receivers.

When creating GNSS data combinations, the following equation can be used for the new wavelengths and frequencies to be generated [1]:

$$\phi = x\phi_n + y\phi_m \tag{2.5}$$

Here, ϕ_n and ϕ_m represent any two carrier signals where $n \neq m$, broadcast from the same constellation to be selected, including the modernized carrier signals (e.g., L5). By multiplying these frequencies with two random integers to choose from, the frequency of the new carrier signal is obtained:

$$f_{new} = xf_n + yf_m \tag{2.6}$$

The wavelength of this frequency f_{new} is obtained from Table 2.1.

Widely used GNSS data combinations that are explained in the subsequent sub-chapters are listed below:

- Geometry-Free Combination
- Ionosphere-Free Combination
- Wide-Lane Combination
- Narrow-Lane Combination
- Melbourne-Wübbena Combination
- Ultra Wide-Lane Combination

2.7.1. Geometry-Free Combination

Geometry-free combination cancels the frequency-independent terms in GNSS observables, including the geometric range, satellite and receiver clock errors and tropospheric delay, and leaves frequency-dependent error sources such as ionospheric refraction, hardware delays and wind-up effect. This combination can be obtained by differencing code-pseudorange or carrier-phase observables of two distinct frequencies of the same constellation.

While the geometry-free combination can be used to determine the ionospheric electron content, numerous methods for detecting cycle-slip also utilize this combination. Below is the carrier-phase equation utilized for the geometry-free combination, e.g., utilizing L1 and L2 signals of GPS:

$$\phi_{GF}=\phi_{1} + \phi_{2} \tag{2.7}$$

The equation for code-pseudorange observations is quite similar to Equation 2.7 and is given below:

$$CP_{GF} = C_{1} - C_{2} \tag{2.8}$$

2.7.2. Ionosphere-Free Combination

Ionosphere-free combinations are made to eliminate almost all first-order ionospheric effects [16,17,42]. This is because the ionosphere is the most difficult parameter to model for each observation type. Ionosphere-free combinations for code-pseudorange and carrier-phase observations are written individually. Ionosphere-free combination for dual-frequency carrier-phase measurements can be expressed as:

$$\phi_{IFree}=\frac{f_{1}^{2}\phi_{L_{1}}+f_{2}^{2}\phi_{L_{2}}}{f_{1}^{2}-f_{2}^{2}} \tag{2.9}$$

The Equation 2.9 can be expressed for code-pseudorange by simply changing the carrier-phase expression as follows:

$$CP_{IFree}=\frac{f_{1}^{2}CP_{L_{1}}+f_{2}^{2}CP_{L_{2}}}{f_{1}^{2}-f_{2}^{2}} \tag{2.10}$$

One of the reasons why ionosphere-free combinations are created is because rapid changes in the ionosphere have a very disruptive effect on the signals. In addition, cycle-slip algorithms frequently misjudge ionospheric variations for cycle-slips, resulting in false cycle-slip detection. If high-rate data are used, the ionospheric variation is small and stable, this term can be removed from the equations [1]. The complex carrier-phase and code-pseudorange ionosphere-free formula is as follows:

$$\Lambda_{L_{f_3}} \phi_{L_{f_3}} = \rho + c(dt^{rec} + dt^{sat}) + Trop + \beta r_{L_{f_3}} - \beta s_{L_{f_3}} + \Lambda_{L_{f_3}} N_{L_{f_3}} + \Lambda_{L_{f_3}} w + M_{L_{f_3}} + E_{L_{f_3}} \quad (2.11)$$

$$C_{P_{f_3}} = \rho + c(dt^{rec} + dt^{sat}) + Trop + \beta r_{P_{f_3}} - \beta s_{P_{f_3}} + M_{P_{f_3}} + E_{P_{f_3}} \quad (2.12)$$

These parameters can be independently applied to each GNSS constellation and are designed for dual frequencies. Because there is only one possible combination for dual-frequency, the total number of possible combinations is one [20]. The new signal generated here is mostly categorized as P3 and L3. As new frequencies enter the field of GNSS, the equations created for this dual frequency can be combined in three diverse ways (e.g., [L1-L2], [L1-L5], [L2-L5] for GPS) as dual-frequencies.

2.7.3. Wide-Lane Combination

The purpose of using wide-lane combinations is to produce other signals with significantly longer wavelengths. One of the great advantages of creating long wavelengths is that it is frequently used to detect cycle-slips occur on carrier-phase observations [11]. This combination yields a new signal that is not used for positioning, but rather allows the elimination of various defects in the observations.

The wide-lane combination used for carrier-phase measurement is expressed by the following equation:

$$\phi_{WL} = \frac{f_1 \phi_1 - f_2 \phi_2}{f_1 - f_2} \quad (2.13)$$

This combination can also be used on code-pseudorange observations. The combination used for code-pseudorange is expressed by the following equation:

$$CP_{WL}=\frac{f_1 CP_1 - f_2 CP_2}{f_1 - f_2} \tag{2.14}$$

2.7.4. Narrow-Lane Combination

In the narrow-lane combination, a new signal is created by generating shorter wavelengths than those of the signals transmitted by satellites. The primary objective of this combination is to reduce existing signal noise by shortening wavelengths. When the cycle-slip detection process is performed on the new signal obtained by reducing the noise level, the mixing of the noise level and cycle-slips can be avoided. Nonetheless, the wavelength derived from this combination can also produce unsatisfactory results in the detection of cycle-slips.

$$\phi_{NL}=\frac{f_1\phi_1 + f_2\phi_2}{f_1 + f_2} \tag{2.15}$$

If the Equation 2.15 is given for code-pseudorange observations:

$$CP_{WL}=\frac{f_1 CP_1 + f_2 CP_2}{f_1 + f_2} \tag{2.16}$$

2.7.5. Melbourne-Wübbena Combination

This combination firstly developed by Hatch [43], further Melbourne [44] and Wübbena [45] used it. Melbourne-Wübbena (MW) combination is a technique used to improve the accuracy of position estimates by combining the results of multiple GNSS observations. The MW combination is based on a linear model that considers correlations between the errors in the observations and the differential ionospheric delay between the GNSS constellations.

When precise positioning information is required in geodetic and geophysical applications, the Melbourne-Wübbena combination is widely applied. It is especially useful when multiple GNSS systems are used simultaneously, such as in multi-GNSS receiver systems or GPS/GLONASS receiver systems. Cycle-slip detection methods are one of the major uses of this combination. However, this combination has both pros and cons. The MW combination does not mark cycle-slips in a continuous satellite arc as cycle-slips and accepts them all as normal. Depending on the satellite-elevation angles, there may be situations in which the performance of this combination falls significantly below the acceptable level.

2.7.6. Ultra Wide-Lane Combination

Dual and triple-frequency generally uses ultra-wide-lane combinations; this has been the case since the introduction of modernized signals into the GNSS world. This method can be expressed as follows for dual-frequency and uses MW triple combinations:

$$UWL = \frac{f_1 - f_2}{f_1 + f_2} \left(\frac{CP_1}{\Lambda_1} + \frac{CP_2}{\Lambda_2} \right) - (\phi_1 - \phi_2) \tag{2.17}$$

2.8. GNSS Error Sources

The rapid advancement in technology has resulted in a discernible improvement in the point positioning accuracy of suitable navigation systems. The errors on GNSS began to be modeled more accurately, as one of the effects that led to this advancement was the development of devices and the improvement of their software. With this capability, the majority of positioning errors result in a significantly improved strategy or method for error elimination.

This section will focus on reducing the effects of GNSS errors through modeling or, if possible, eliminating them.

2.8.1. Tropospheric Delay

The troposphere is the part of the Earth's atmosphere structure that is closest to the surface of the planet. Almost all weather events that we are exposed to daily occur in this layer. The troposphere comprises more than 75% of the total mass of the atmosphere. The majority of causes of tropospheric effects originate in the troposphere's lowest levels. Temperatures decrease by 6.5° C per kilometer as we ascend. This layer contains the most of the atmosphere's pollution and vapor. Between 20 and 50 kilometers is the stratosphere, the second layer of the atmosphere. This layer is devoid of clouds and has a constant temperature. The most significant aspect of this layer is that it contains ozone, which shields the Earth from harmful radiations.

The effects of the troposphere are extremely important for geodetic applications, but their effects can be negligible in some cycle-slip detection process scenarios. Nevertheless, they must be modeled because the tropospheric delays cannot be eliminated using differencing techniques. Tropospheric delays can be calculated with some models. The Saastamoinen model can be given as an example of the most well-known of these and this is a mathematical model used in geodesy and satellite navigation to account for the delay caused by the Earth's troposphere. The Saastamoinen model provides a method for calculating the zenith delay caused by the atmosphere and correcting the measured signal travel time. The model takes into account parameters such as temperature, pressure, and humidity to estimate the tropospheric delay [46].

While the Saastamoinen model is adequate for the majority of practical applications, some more sophisticated models incorporate additional factors and refinements to improve accuracy, such as the Niell Mapping Function and the Global Mapping Function [47].

2.8.2. Ionospheric Delay

In terms of signal propagation, the ionosphere is the second atmospheric structure to be discussed. The ionosphere is the layer of the atmosphere that follows the stratosphere, and it accepted to begin between the first 50 and 70 kilometers and extends up to 1100 kilometers or more.

The ionosphere's layers are not precisely defined. Undefined transition parts of these layers have "pause" added to them [21]. The vertical structure of the ionosphere is divided into 4 different layers with different characteristics. These layers are given in Table 2.2 below:

Table 2.2. Ionospheric Layers

Approximate Height (km)	**Region**
50-90	D
90-140	E (E1, E2, Es)
140-500	F (F1, F2)

The D layer is only active during the day and loses its functionality at night. It is considered active during the day due to the ions that cause the production of X-rays. 90 kilometers separate the end of the D layer from the beginning of the E layer. The E layer can be subdivided into three distinct sub-layers, each with distinct properties. They are active day and night and reflect rather than transmit low-frequency radio waves. In general, the literature considers the F layer to have two sub-layers. In addition to the outermost layer having the highest electron density, the electron density increases as one ascends. Within these layers, the temperature begins to decrease as height increases.

This part of the atmosphere can also cause significant GNSS signal disturbances. The ionosphere can have far more detrimental effects than anticipated on the desired precision. To be more specific, the measurement method employed, the type of observation, and the processing methods also alter the effect of the ionosphere's disruptive effect on the process. Depending on the location of the receiver, the effects of the ionosphere on observation techniques can also vary.

It is necessary to understand the electron density encountered by the transmitted signal in the ionosphere. This is done to determine how the charged particles present in the ionosphere inhibit the signal's progression. Due to the structure of the ionosphere, signals with certain small frequencies cannot reach space and cannot pass through the ionosphere, so they are reflected to Earth. For signals to avoid the ionosphere's reflective effect, their frequencies must exceed a certain threshold. To counteract the effect of the ionosphere's reflection, GNSS satellites transmit signals between 1-2 GHz [42].

TEC (Total Electron Content) is characterized by the total amount of electrons that these signals sent from orbiting satellites and absorbed by the receivers encounter while passing through the ionosphere [11]:

$$TEC = \int_{Satellite}^{Receiver} Ne(s)ds \tag{2.18}$$

Equation 2.18 is used to calculate the electron density per square meter. Since the total number of electrons is quite large, a TEC constant has been derived to simplify the understanding of the processes. This constant is known as TEC Unit and its equation is as follows [11]:

$$TECu = 1*10^{16}\ electrons\,/\,m^2 \tag{2.19}$$

The effects of the ionosphere on cycle-slip are dependent on the number of frequencies utilized by the receivers. If processing is performed using a single-frequency receiver and the location of this receiver is in an ionosphere-active region, then ionospheric models are required. This is due to the likelihood of false alarms in the determination of cycle-slips in the observation data received from the single-frequency receiver in the event of rapid ionosphere changes. There are several methods for modeling ionospheric data from a single receiver. The Klobuchar model is one of the most frequently used of these models [48–50].

GNSS data combinations can eliminate ionospheric effects if dual-frequency receivers are available. In this regard, however, there is an exception for receivers that can decode dual-frequency P(Y) code. These devices can eliminate ionosphere interference with incoming signals [51]. Each additional frequency increases the probability that the ionosphere's effects will be eliminated. Details on ionosphere-free combination are given in Section 2.7.2.

2.8.3. Satellite Clock Error

Errors in satellite clocks are crucial for providing precise positioning in satellite-based navigation systems [19,20]. The cause of these errors is the discrepancy between the accuracy of the clocks installed in the satellites and their actual time. The clocks used in satellites are atomic clocks with extreme precision and have no relation to the clocks used in daily life. As is the case with everything human-made, there will inevitably be variations following the passage of time, even if it is known to be relatively accurate. Satellite clock errors can be eliminated via the parameters in the navigation file [52]. Different techniques can eliminate satellite clock errors [53].

2.8.4. Receiver Clock Error

The difference between the clocks available in GNSS receivers and the related GNSS-time is the receiver clock bias. The receivers' clocks are quartz oscillator clocks, which are less precise than atomic clocks.

While the effects on the bias of receiver clocks are expressed in milliseconds, the effects on satellite-clocks can reach hundreds of meters [54]. Single-difference methods formed between satellites can eliminate biases due to receiver's clock.

2.8.5. Multipath Error

Today, with the rapid advancement of GNSS receiver technology, the effects of certain errors on precise and accurate positioning have diminished. Despite these advancements, the multipath effect, one of the most significant effects in GNSS positioning, continues to exist. Multipath is the single or multiple reflections of satellite signals before they reach the receivers due to external factors such as tall buildings, trees, scattering from the ground, and the presence of multiple reflective surfaces [55]. Multipath effect is larger for the signals from satellites at a low elevations.

Multipath errors are present in both carrier phase and code-pseudorange measurements, but their effects are much lower in carrier-phase observables.

The effect of multipath on C/A and P codes is measured in meters and to eliminate these errors, it is necessary to select a location for the receiver that eliminates the effect of reflective surfaces [56]. This is the most efficient elimination method for both measurement techniques.

Choke-ring receivers are optimal for reducing multipath errors and can be chosen in either of two varieties.

2.8.6. Hardware Delays

Hardware-related delays are due to the hardware components such as circuits, cables antennas etc. Receivers and satellites have different hardware delays. These delays are unidirectional and generate systematic error. Hardware delays are not random occurrences. That is why they are considered reasonably stable throughout the day. In each satellite-based system, signal and frequency-specific delays vary. In addition, they vary for each code-pseudorange and carrier-phase observation.

It was stated that receiver and satellite clock biases could be eliminated using data combination techniques. However, it is impossible to eliminate the effects of both satellite and receiver hardware delays on observations. After using these combinations, the hardware delay differences remain unchanged. Observations involving code-pseudorange, these are referred to as Differential Code Bias.

3. CYCLE-SLIP DETECTION

3.1. Definition of Cycle-Slips

In the previous Section 2.6. and 2.7., while giving the definitions of code-pseudorange and carrier phase observations, the errors that occurred in these observations were also mentioned. The precision levels of these observations are quite different from each other. The basic principle in applications to achieve precision is to eliminate the sources of error as much as possible, to reduce their effects to negligible levels.

It is essential to use carrier-phase observables in very precise operations such as geodetic applications and deformation analysis [57]. Although the precision of these observations is remarkably high, some effects can impair this precision. One of the most important of these effects is called cycle-slips.

Cycle-slips, as the name suggests, are not present in code-pseudorange observations, they are unique to carrier-phase observables [58]. When a GNSS receiver is activated, it is locked to visible satellite signals while the initial integer number of full carrier cycles between the satellite and the receiver, i.e., the ambiguity term is unknown. The ambiguity is constant as long as there is no discontinuity exists in the tracked carrier phase signal. A cycle-slip is the temporary loss of lock of a tracked GNSS signal. Each of the intervals that a receiver can receive satellite signal without interruption is called an observation arc. These arcs are continuous until the satellite ceases to be visible or some sort of cycle-slip occurs. However, these continuous arcs are corrupted when the cycle-slip occurs, and the ambiguity term is rebuilt with a jump of integer number of wavelength of the carrier signal [59]. This both causes a new observation arc to start and seriously affects the precision. This both causes a new observation arc to start and degrades the precision. Figure 3.1 represents a generic cycle-slip.

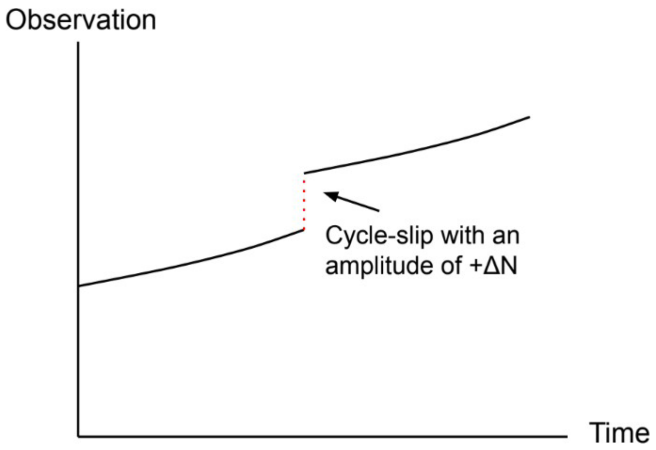

Figure 3.1. Representation of Cycle Slip

It is not possible to definitively prevent all causes of cycle-slips in carrier-phase observables under all circumstances. Some of these conditions are due to the nature of satellite-based navigation systems. Apart from the nature of satellite navigation systems that would increase the probability of their formation, there are other reasons as well. In today's conditions, the possibility of signals contacting reflective surfaces and distortion of observations due to these effects has increased. From this point of view, the most probable cause of cycle-slips is the objects that the signal encounters on its arrival path.

If the GNSS receiver is standing too close to reflective surfaces, or if there are dense, human-made structures and natural formations such as trees along the path of the satellite's signal that will block its path, the chances of the signal being interrupted increase considerably. The reason why there are signal interruptions in contact with these objects is the elevation angles of the GNSS satellites [60]. The lower the GNSS satellite elevation angles, the higher the possibility of the signals to contact the objects. In addition, low GNSS satellite elevation angles introduce errors that can affect observation such as tropospheric effects, ionospheric effects, and code-pseudorange noise [49]. The higher the GNSS satellite elevation angles, the higher the accuracy of the detection of cycle-slips. Another reason for the formation of cycle-slip is the signal strength [61]. Signal-to-noise ratio (SNR) values are numbered from 1 to 9. If this SNR value is below 5 (30 - 35 db-HZ), the probability of cycle-slip formation increases. Although it is very rare, another reason for the cycle-slip to occur is due to malfunctions in the hardware or software [62]. However, nowadays, with the incredible advances in receiver technologies, the probability of encountering software or hardware errors is gradually decreasing.

Cycle-slip detection and repair are performed in the data-preprocessing step in GNSS data analysis. Because it is not possible to expect the precision to reach the desired level without repairing the cycle-slips or starting a new observation arc in the data. Even a deviation of one integer-cycle will deviate as much as the wavelength of the signal sent by a satellite of the GNSS constellation whose observation values are received (e.g., L5 ≈ 15 cm) [59]. If it is not corrected, the expected millimeter-level precision cannot be achieved in carrier-phase observations.

There are a few steps to overcome the effects of cycle-slips. Each of these steps should be handled carefully and it should be ensured that the actions taken are correct. Because cycle-slips cannot be modeled precisely like some other effects on observations, they occur randomly. Therefore, it is quite common to make false detections. The steps of detecting and removing cycle-slips from the carrier-phase observation can be categorized as follows [63]:

- Cycle-slip detection
- Cycle-slip determination
- Cycle-slip validation
- Cycle-slip removal

The last three steps are called cycle-slip repairing. Since topics other than cycle-slip detection are not evaluated within the scope of the thesis, they will not be explained in this chapter. Note that once a cycle-slip is detected, instead of its removal, the related epoch can be assigned as a starting point for a new continuous arc as an alternative.

3.2. Cycle-Slip Detection

Cycle-slip detection is one of the most important steps for GNSS data-preprocessing. The cycle-slip detection steps vary according to the number of frequencies that will be processed. In addition, this should not be overlooked when working with multi-GNSS, as the different constellations of GNSS do not have the same frequency. When performing cycle-slip detection, threshold parameters must be determined well, otherwise errors may occur in the results. Although this situation may reveal false detection, they cause incorrect data to be obtained for repair steps. To successfully implement a cycle-slip detection process, each processing step must be executed with extreme caution.

The general steps for cycle-slip detection in a stored GNSS observation data under dual-frequency conditions are as follows:

1. Read the GNSS data file line-by-line: The first step is to download the observation file and afterwards read the GNSS data file line-by-line, where each line contains the observation data for a specific epoch. The RINEX observation data typically includes the pseudorange and carrier phase measurements for each satellite signal tracked by the receiver. After extracting Loss of Lock Indicator (LLI) and Signal Strength Indicator (SSI) values, the data should be organized and stored. Observation data from epochs with an LLI equal to 1 should not be used.
2. Calculating satellite coordinates and elevation angles (Optional): Satellite coordinates must be calculated if elevation angles are to be used as a comparison factor for cycle-slip detection results. Afterwards, elevation and azimuth angles must be computed for every epoch.
3. Form single, dual or triple frequency combinations: The next step is to compute the single, dual or triple-frequency combinations, such as the geometry-free combination or the Melbourne-Wübbena Wide Lane combination. Dual-frequency observations are used in cycle-slip detection mostly because they are less affected by common errors and biases than single-frequency observations. Alternatively, triple-frequency observations may be used if available. Note that triple-frequency observations allow forming many more observation combinations with larger wavelengths.
4. Computing phase differences: To detect cycle-slips, the phase differences between consecutive epochs for each satellite signal need to be computed. The phase difference is computed by subtracting the previous carrier-phase measurement from the current carrier-phase measurement.
5. Apply outlier rejection (Optional): Outlier rejection is typically applied to the phase differences to remove any measurement errors or biases. Common methods

for outlier rejection include median filtering or statistical tests such as the Grubb's test or the Student's t-test.

6. Compute cycle-slip indicators: Cycle-slip indicators are computed based on the phase differences and the outlier-rejected phase differences. The most common cycle-slip indicators are the cycle-slip ratio and the geometry-free phase combinations. After developing or using the detection algorithm, each cycle-slip index must be flagged and if the algorithm allows size determination, they must be stored in an array.
7. Applying cycle-slip detection threshold: The cycle-slip detection threshold is applied to the cycle-slip indicators to determine whether a cycle-slip has occurred. The threshold value depends on the receiver and the specific measurement scenario. Common threshold values range from 0.2 to 1.0 cycles. The threshold value should be set sufficiently high to avoid false-positive cycle-slip detection caused by noise or other sources of errors mentioned in Section 2.8, while remaining sensitive enough to detect real cycle-slips. Setting the threshold to a few times the expected standard deviation of the phase difference between consecutive epochs is a good starting point.
8. Correct cycle-slips: If a cycle-slip is detected, the carrier phase measurements for the affected satellite signal need to be corrected. In some cases, the carrier-phase observations can be corrected with a simple cycle-slip repair algorithm. If cycle-slip repair is possible, it is recommended to apply them after the cycle-slip detection and make the carrier-phase observations cycle-slip free.
9. Write the corrected data to a new file: Finally, the corrected GNSS data can be written to a new file for further processing or analysis. The specific implementation may depend on the data format and the cycle-slip detection algorithm used.

3.3. Single-Frequency Cycle-Slip Detection

The solutions that can be obtained with single-frequency are affected by the errors that can be eliminated with the combinations that can be obtained with the help of additional frequencies.

The route quickly turned to dual-frequency since the performance of the single-frequency cycle-slip detection and repair algorithms made in the early years of GPS was not at the desired level and a large number of error factors needed to be eliminated to achieve precise positioning, in addition to creating too much computational burden. However, nowadays, single-frequency cycle-slip methods have started to become popular again due to the extensive number of low cost receivers and their ability to provide the required proficiency in some areas [64]. Cycle-slip detection and repair are of great importance in every scenario where single-frequency is used, although it is not preferred for static applications and the scenarios that require high precision. The only cycle-slip detection method included in the study is described in the following sub-chapter.

3.3.1. Phase-Code Comparison

The best-known and most legacy method for single-frequency cycle-slip detection is the technique of taking the difference between carrier-phase and code-pseudorange. Code-pseudorange observations are used to eliminate geometry term, receiver and satellite clock errors and other non-dispersive errors according to Equation 2.3 and Equation 2.4 [65]. After subtracting the carrier-phase and code-pseudorange observations, only ionospheric term and integer-ambiguity remain. The formula of this subtraction is as follows:

$$C_{P_{f_n}} - \Lambda_{L_{f_n}} \phi_{L_{f_n}} = k * I - \lambda N + \epsilon \tag{3.1}$$

where, $n = 1$, $C_{P_{f_n}}$ is the code-pseudorange observations in meters, $\Lambda_{L_{f_n}} \phi_{L_{f_n}}$ is the carrier phase observations in meters, I is the ionospheric term with k factor of 2. λN indicates the integer ambiguity and ϵ is the after-combination error.

$$\delta = C_{P_{f_n}} - \Lambda_{L_{f_n}} \phi_{L_{f_n}} \tag{3.2}$$

The applied threshold of single-frequency is as follows:

$$|\delta| > \sqrt{2} * 4 * \sigma_{\epsilon} \qquad (3.3)$$

where, σ_{ϵ}, is the standard deviation of code-pseudorange observation noise, 4 is the factor of σ_{ϵ}, if $|C_{P_{f_n}} - \Lambda_{L_{f_n}} \phi_{L_{f_n}}|$ exceeds the applied threshold, it indicates that the cycle-slip occurred.

This combination is a simple way to detect cycle-slips, but it should be noted that the success rates mainly depend on the σ_{ϵ} It should be carefully considered that this combination cannot detect small cycle-slips accurately. If the σ_{ϵ} values are high, the success rates of code-phase comparison decrease significantly.

3.4. Dual-Frequency Cycle-Slip Detection

With an additional frequency, it is possible to form linear combinations in GNSS observations. In the following subsections, dual-frequency post-processing algorithms that are included in the study will be explained with their pros and cons.

3.4.1. Melbourne-Wübbena Wide-Lane Combination

The Melbourne-Wübbena is a widely-used combination GNSS positioning technique. Applied primarily to eliminate effects that are non-dispersive, Melbourne-Wübbena combination makes it simpler to detect cycle-slips in observations due to the longer wavelength and reduced noise in the observations [66].

GNSS signals encounter various layers of charged particles of the ionosphere, as they travel through the Earth’s atmosphere. The ionosphere can delay and alter the path of signals, leading to errors in position estimations. Melbourne-Wübbena Wide Lane combination is also known to cancel the first-order ionospheric refraction.

The MW combination is performed by taking the linear combination of the phase measurements from two frequencies, and its formulae is as follows:

$$MW_{WL}=\phi_n-\phi_m-\frac{f_n-f_m}{f_n+f_m}\left(\frac{CP_n}{\lambda_n}+\frac{CP_m}{\lambda_m}\right) \tag{3.4}$$

for the indices n and m are indicates L1 and L2 signals, ϕ_n and ϕ_m is the carrier-phase measurements, CP_n and CP_m is the code-pseudorange measurements, λ_n and λ_m is the wavelengths of the signals, f_n and f_m is the carrier frequencies of the signals, respectively. Related GNSS frequencies can be found in Table 2.5. Wide-lane ambiguity is calculated as follows:

$$N_{MWWL}=\phi_n-\phi_m-\frac{f_nCP_n-f_mCP_m}{\lambda_{WL}(f_n+f_m)} \tag{3.5}$$

$$\lambda_{WL}=c\frac{1}{(f_n-f_m)} \tag{3.6}$$

Cycle-slip detection is performed by taking mean values for each epoch and comparing them with each other. Related equation is shown below:

$$\overline{N_{MWWL}}(i)=N_{MWWL}(i)-N_{MWWL}(i-1) \tag{3.7}$$

where i is the current epoch and N_{MWWL} is the mean value of the two consecutive epochs. After the calculation of the standard deviation of the ambiguities, the cycle-slip threshold can be given as:

$$\left|\overline{N_{MWWL}}-N_{MWWL}\right|\geq K^*\sigma_{MWWL} \tag{3.8}$$

where K is the sensitivity factor, it can be valued as 4. Under specific scenarios, K can be equal to 3. If the condition in Equation 3.8 is satisfied, it can be declared that the cycle-slip is found and it can be flagged.

3.4.2. Traditional Turbo-Edit Algorithm

The TurboEdit algorithm is one of the legacy cycle-slip detection and repair methods and is widely used. This algorithm was first developed for dual-frequency, and modernized versions are available. TurboEdit does not need single, dual, or triple differencing like most other algorithms, and the difference that makes it important is that it can be used in real-time [67].

TurboEdit algorithm uses MWWL combination and geometry-free combination as cycle-slip detection methods, and ionospheric combination for cycle-slip repair [67–69]. Using Equation 2.14:

$$\lambda_{WL}=\frac{c}{f_1-f_2}=0.86192 \tag{3.09}$$

$$\phi_{WL}=\phi_1-\phi_2 \tag{3.10}$$

where ϕ_{WL} is the wide-lane carrier-phase observation and λ_{WL} is the wide-lane wavelength,

$$L_{WL}=\phi_{WL}*\lambda_{WL} \tag{3.11}$$

Where L_{WL} is the wide-lane carrier-phase observation in the unit of meters. After the Melbourne-Wübbena Wide Lane combination is obtained, it is evaluated whether there is a cycle-slip in the wide-lane observations with the recursive filter of the TurboEdit algorithm and the following formulas are used for the i-th epoch [67]:

$$\overline{N_{WL}}(i)=N_{WL}(i-1)+\frac{1}{i}\left(N_{WL}(i)-\overline{N_{WL}}(i-1)\right) \tag{3.12}$$

$$\overline{\sigma^2}(i) = \sigma^2(i-1) + \frac{1}{i}\,(N_{WL}(i) - \overline{N_{WL}}(i-1)^2 - \sigma^2(i-1)) \qquad (3.13)$$

where i is the current epoch and $i-1$ represents the previous epoch, $\overline{N_{WL}}$ is the mean value of the wide-lane ambiguity and the variance of N_{WL} at epoch i. In TurboEdit algorithm, the threshold value and the conditions of the occurrence of cycle-slip as follows:

$$\left|N_{WL}(i) - \overline{N_{WL}}(i-1)\right| \geq f * \sqrt{(\sigma^2(i))} \qquad (3.14)$$

$$|N_{WL}(i+1) - N_{WL}(i)| \leq 1 \qquad (3.15)$$

where $N_{WL}(i+1)$ is the next epoch of wide-lane ambiguity. If Equation 3.8 are satisfied, the cycle-slip is considered to have occurred and is marked. Note that TurboEdit algorithm cannot detect very small cycle-slips as it uses the Melbourne-Wübbena Wide Lane combination [68].

3.4.3. Geometry-Free Combination with Different Thresholds

The geometry-free combination is formed via Equation 2.7 and 2.8. As described in Section 2.7.1, the satellite to receiver range, clock errors and tropospheric delay can be eliminated with this combination. If the ionosphere is sufficiently quiet, geometry-free observations will appear quite smooth, and any cycle-slips will be easy to detect. However, if the ionospheric refraction is high enough, low satellite elevation angles can change the smooth image of geometry-free observations, and in addition, observations with low sampling rates can produce the same effect [70].

After the geometry-free observation is obtained, the cycle-slips are determined by comparing the threshold obtained with the help of the following equations and geometry-free observations. Two different threshold approaches can be considered for this purpose. One of them is the sampling rate and the other is elevation angle dependent threshold. The threshold based on sampling rate can be given by the following formula [71]:

$$GF_{threshold}=a_0-a_1*exp(-\frac{\delta_i}{T_0}) \quad (3.16)$$

where i is the current epoch and $\delta_i = i_1 - i_0$, and,

$$a_0=3\left(\frac{\lambda_2 - \lambda_1}{4}\right),\ a1=\frac{a_0}{2}\ ,\ T_0=60\ seconds \quad (3.17)$$

Another threshold method is available for geometry-free cycle-slip detection where satellite elevation angles are taken into account and time signatures are not considered. This is because in the case of low elevation angles, false-positive rates may increase if the standard deviation values are kept low [70]. The elevation angle-dependent threshold is as follows [72]:

$$\sigma_{GF} = \sqrt{(2*\sigma_n^2 + \sigma_m^2)}\ M(E) \quad (3.18)$$

$$M(E) = 1 + 10exp - \frac{E}{10} \quad (3.19)$$

where σ_n^2 and σ_m^2 is the standard deviations of carrier frequencies of $n = 1$ and $m = 2$, respectively. *E* represents the satellite elevation angles in the unit of degrees and *M(E)* is the scaling factor.

3.4.4. MWWL and GF Hybrid Method

Cycle-slip detection success rate can be improved by using the mutual use of Melbourne Wübbena Wide Lane and Geometry-Free Combination methods [73]. With the help of this method, both the deficiencies in the Melbourne-Wübbena combination are covered and almost all false-positive rates that can be seen in the cycle-slip detection process can be eliminated. Also, the Melbourne Wübbena Wide Lane combination fails to detect some specific cycle-slip pairs. The most well-known of these are 77 for L1 and 60 for L2. In addition, the MWWL combination does not have significant success in the 1-2 cycle range and cannot be detected if cycle-slip occurs at the same amplitude at both frequencies. It is expected to overcome these problems by using the combination of MWWL and GF together.

3.4.5. Scheme of Differences

This method is known as the “easiest way” to detect cycle-slips in carrier-phase measurements. With the help of this method, errors and cycle-slip amplitudes on the measurement can be seen much more clearly. These differences are determined by subtracting each epoch from the previous value. These differences are known as geometry-free combination in first-order differences. Usually, these differences give reasonable results in the third order, but the fourth-order differences are shown in the diagram below so that they can be properly explained as an example [1]:

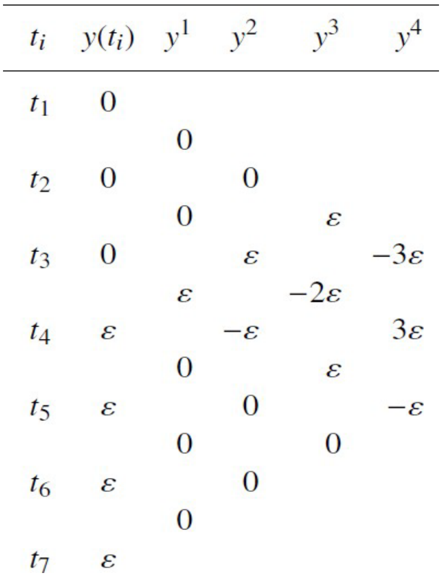

t_i	$y(t_i)$	y^1	y^2	y^3	y^4
t_1	0				
		0			
t_2	0		0		
		0		ε	
t_3	0		ε		-3ε
		ε		-2ε	
t_4	ε		$-\varepsilon$		3ε
		0		ε	
t_5	ε		0		$-\varepsilon$
		0		0	
t_6	ε		0		
		0			
t_7	ε				

Figure 3.2. Scheme of Differences [1]

For each *ti* value *i = 1,...,7* observation epochs, *y(ti)* testing quantities with cycle-slip, yk, *k = 1, 2, 3, 4* for first to fourth-differences [64].

3.5. Triple-Frequency Cycle-Slip Detection Methods

The term “triple frequency” refers to the satellites ability to transmit carrier-phase measurements at three different frequencies [74]. Many different combinations can be created using triple-frequency signals. Considering the triple-frequency cycle-slip detection, while one detection combination is not sufficient to detect cycle-slips on each carrier-phase observations, it is necessary to use three detection combinations to determine the cycle-slip sizes at each individual frequency. Determining cycle-slip sizes with triple-frequency is relatively easier than single and dual-frequency cycle-slip detection as well as the repair processes. Detection parameters suitable for special scenarios can be created with many combinations. In consequence, with triple-frequency, it adds more depth to the cycle-slip detection procedures.

3.5.1. Fundamentals of Triple-Frequency Cycle-Slip Detection

In triple-frequency, the approach is to reduce the observation noise in addition to getting much longer wavelengths. Consequently, detection success rates for cycle-slip increase. Note that no differenced observations are involved, the following sections are for undifferenced observations.

First of all, linearly combined phase must be created for triple-frequency. The formula used for this process is given below [75]:

$$\phi_{a,b,c} = \frac{af_1\phi_1 + bf_2\phi_2 + cf_3\phi_3}{af_1 + bf_2 + cf_3} \tag{3.20}$$

where, $\phi_{a,b,c}$ is linearly combined phase observation in meters, f_1 , f_2 , f_3 are the frequencies of each GNSS signals, respectively. Most important part of the this linearly combined phase observation, are the integer coefficients which are a, b and c, respectively. These coefficients must be an integer to keep the integer nature of carrier-phase ambiguities. Frequency and wavelength of linearly combined phase observation are as follows:

$$f_{a,b,c} = af_1 + bf_2 + cf_3 \tag{3.21}$$

$$\lambda_{a,b,c} = \frac{c}{f_{a,b,c}} \tag{3.22}$$

where, c is the speed of light in meters. For triple-frequency frequencies, the following conditions must be satisfied and expressed as [76]:

$$f_1 > f_2 > f_3 \tag{3.23}$$

$$f_2 - f_5 < f_1 - f_2 \tag{3.24}$$

For triple-frequency, the code-pseudorange observations can be defined via the following equations [77]:

$$CP_{a,b,c} = \frac{af_1 CP_1 + bf_2 CP_2 + cf_3 CP_3}{af_1 + bf_2 + cf_3} \tag{3.25}$$

After triple-frequency linearly combined phase and code-pseudorange observations, the ionospheric scale factor (ISF) and phase noise factor must be determined via following equations [75,78]

$$ISF_{a,b,c} = \frac{f_1^2 (a/f_1 + b/f_2 + c/f_3)}{af_1 + bf_2 + cf_3} \tag{3.26}$$

$$\epsilon^2_{a,b,c} = \frac{(af_1)^2 + (bf_2)^2 + (cf_3)^2}{f^2_{a,b,c}} \tag{3.27}$$

where, $ISF_{a,b,c}$ is the ionospheric scale factor, $\epsilon^2_{a,b,c}$ a,b,c is the phase noise factor. After all these parameters are obtained, the triple-frequency cycle-slip detection steps can be initialized.

3.5.2. Triple-Frequency Cycle-Slip Detection Approach

Triple-frequency cycle-slip detection is performed in three main steps and one extra step for detection of insensitive cycle-slips. Since insensitive cycle-slip pairs are not included in the thesis, they will not be explained in detail.

In the first of these three main steps, the Extra Wide-Lane (EWL) combination is used with the aim of obtaining very long wavelengths, eliminating the disruptive effect of the ionosphere on the signal and eliminating the tropospheric delay, which is another atmospheric effect, with the aim of creating a geometry-free observation. After all of these errors are eliminated, only the EWL ambiguity term remains. The ambiguity term of the EWL combination can be formed using the combination Hatch-Melbourne-Wübbena as follows:

$$N_{[EWL]}(t)=\left(\frac{f_2 CP_2(t)+f_3 CP_3(t)}{f_2+f_3}-\frac{f_2\phi_2(t)+f_3\phi_3(t)}{f_2+f_3}\right)/\lambda_{[EWL]} \tag{3.28}$$

where, *t* is the current epoch, and note that the original carrier-phase and code-pseudorange observations are used in Equation 3.28. In addition, carrier-phase observations are in meters.

The cycle-slips containing in the EWL combination can be obtained via differencing the ambiguity terms epoch-by-epoch:

$$N_{[EWL]}(t)-N_{[EWL]}(t-1)=\left(\begin{matrix}\dfrac{f_2 CP_2(t)-CP_2(t)+f_3\left(CP_3(t)-CP_2(t-1)\right)}{f_2+f_3}-\\ \dfrac{f_2(\phi_2(t)-\phi_2(t-1))+f_3(\phi_3(t)-\phi_3(t-1))}{f_2+f_3}\end{matrix}\right)/\lambda_{[EWL]} \tag{3.29}$$

where, t is the current epoch and $(t - 1)$ is the previous epoch. γ [EWL] is the cycle-slip term in the EWL combination. The sizes of the cycle-slips in EWL combination can be simply found by rounding the cycle-slip value. This equation is as follows:

$$\bar{\gamma}_{[EWL]} = round(\gamma_{[EWL]}) \tag{3.30}$$

After the sizes of cycle-slips of EWL combination is calculated, the threshold value should be applied. To determine the cycle-slips in the current epoch, b γ [EWL] value must exceed the applied threshold:

$$\bar{\gamma}_{[EWL]} > 0.5 \tag{3.31}$$

The threshold is applied as 0.5 cycles. If $\bar{\gamma}_{[EWL]}$ exceeds 0.5 cycles, it means that the EWL cycle-slip is found in that epoch. After the size and location of cycle-slips in all epochs are determined, the values of EWL combination can be repaired at epoch t by the Equation 3.32:

$$\phi_{[EWL]}(t) = \phi_{[EWL]}(t) + \bar{\gamma}_{[EWL]}\,\lambda_{[EWL]} \tag{3.32}$$

After the repair of EWL combination, the second step of the triple-frequency can begin. In this step, Wide-Lane combination are determined together with the repaired EWL combinations. The ambiguity term of the Wide-Lane combination is expressed in Equation 3.33:

$$N_{[WL]} = \frac{\phi_{[EWL]}(t) - \phi_{[WL]}(t)}{\lambda_{[WL]}} \tag{3.33}$$

where, $\phi_{[EWL]}$ is the repaired EWL combination, $\phi_{[WL]}$ is the Wide-Lane combination $\lambda_{[WL]}$ is the wavelength of the Wide-Lane combination. The cycle-slip values of Wide-Lane combinations are calculated as follows:

$$N_{[WL]}(t) = \frac{\phi_{[EWL]}(t) - \phi_{[WL]}(t)}{\lambda_{[WL]}} \tag{3.34}$$

The sizes of the Wide-Lane cycle-slips are determined same as the determination of EWL cycle-slips. The equation is as follows:

$$\overline{\omega}_{[WL]} = round(\omega_{[WL]}) \tag{3.35}$$

where, $\overline{\omega_{[WL]}}$ is the integer cycle-slip of Wide-Lane combination. After the $\overline{\omega_{[WL]}}$ is successfully determined, the repair of the Wide-Lane combination should be done. The applied threshold of the Wide-Lane combination is as follows:

$$\overline{\omega}_{[WL]} > 0.5 \tag{3.36}$$

The repair of Wide-Lane (WL) combination is same as the EWL combination and as follows:

$$\phi_{[WL]}(t) = \phi_{[WL]}(t) + \overline{\omega}_{[WL]}\, \lambda_{[WL]} \tag{3.37}$$

For the third step of the triple-frequency cycle-slip detection, one more combination must be utilized to detect the cycle-slips of the Narrow-Lane combination. In this combination, the effects of ionospheric delay are far more severe, as the wavelength of the signal is significantly shorter than in the case of EWL and WL. For this reason, this effect, which can be neglected in the WL combination, must be used in the Narrow-Lane (NL) combination. The equations of the NL combination are given below:

$$N_{[NL]} = \frac{\phi_{[WL]}(t) - \phi_{[NL]}(t) - \left(ISF_{[WL]} - ISF_{[NL]}\right) I(t)}{\lambda_{[WL]}} \tag{3.38}$$

where, *ISF* is the ionospheric scale factor of each combination, *I* is the ionospheric delay parameter. The cycle-slip value can be determined via following equation:

$$\tau_{[NL]} = N_{[NL]}(t) - N_{[NL]}(t - 1) \tag{3.40}$$

$$\tau_{[NL]} = \left(\phi_{[WL]}(t) - \phi_{[WL]}(t-1)\right) - \left(\phi_{[NL]}(t) - \phi_{[NL]}(t-1)\right) - \frac{\left(ISF_{[WL]} - ISF_{[NL]} I(t) - I(t-1)\right)}{\lambda_{[NL]}} \tag{3.41}$$

After the cycle-slip term is found in NL combination, the rounding function is applied to find the integer-size of the cycle-slip:

$$\bar{\tau}_{[NL]} = round(\tau_{[NL]}) \tag{3.42}$$

To repair cycle-slips on each original carrier-phase observations, NL cycle-slips should be repaired. After the rounding function is applied, repaired NL combination is expressed as:

$$\bar{\tau}_{[NL]} > 0.5 \tag{3.43}$$

$$\phi_{[NL]}(t) = \phi_{[NL]}(t) + \bar{\tau}_{[NL]} \lambda_{[WL]} \tag{3.44}$$

All parameters for GLONASS triple-frequency cycle-slip detection steps are given in Table 3.1:

Table 3.1. GLONASS parameters for triple-frequency cycle-slip detection methods

	Extra Wide-Lane		**Wide-Lane**		**Narrow-Lane**	
	Frequency (MHz)	*Wavelength (m)*	*Frequency (MHz)*	*Wavelength (m)*	*Frequency (MHz)*	*Wavelength (m)*
R01	44.4125	6.7502	400.5375	0.7485	1958.6875	0.1531
R02	42.2250	7.0999	397.7250	0.7538	1955.2500	0.1533
R03	46.1625	6.4943	402.7875	0.7443	1961.4375	0.1528
R04	46.6000	6.4333	403.350	0.7433	1962.1250	0.1528
R05	44.4125	6.7502	400.5375	0.7485	1958.6875	0.1531
R06	42.2250	7.0999	397.7250	0.7538	1955.2500	0.1533
R07	46.1625	6.4943	402.7875	0.7443	1961.4375	0.1528
R08	46.6000	6.4333	403.3500	0.7433	1962.1250	0.1528
R09	43.1000	6.9557	398.8500	0.7516	1956.6250	0.1532
R10	40.9125	7.3276	396.0375	0.7570	1953.1875	0.1535
R11	43.9750	6.8173	399.9750	0.7495	1958.0000	0.1531
R12	43.5375	6.8858	399.4125	0.7506	1957.3125	0.1532
R13	43.1000	6.9557	398.8500	0.7516	1956.6250	0.1532
R14	40.9125	7.3276	396.0375	0.7570	1953.1875	0.1535
R15	43.9750	6.8173	399.9750	0.7495	1958.0000	0.1531
R16	43.5375	6.8858	399.4125	0.7506	1957.3125	0.1532
R17	45.7250	6.5564	402.2250	0.7453	1960.7500	0.1529
R18	42.6625	7.0271	398.2875	0.7527	1955.9375	0.1533
R19	45.2875	6.6198	401.6625	0.7464	1960.0625	0.1530
R20	44.8500	6.6843	401.1000	0.7474	1959.3750	0.1530
R21	45.7250	6.5564	402.2250	0.7453	1960.7500	0.1529
R22	42.6625	7.0271	398.2875	0.7527	1955.9375	0.1533
R23	45.2875	6.6198	401.6625	0.7464	1960.0625	0.1530
R24	44.8500	6.6843	401.1000	0.7474	1959.3750	0.1530
R25	43.9750	6.8173	399.9750	0.7495	1958.0000	0.1531
R26	43.9750	6.8173	399.9750	0.7495	1958.0000	0.1531

In this table, GLONASS slots numbers (*k*) are taken from Table 2.5. The parameters of those with equal slot numbers are also equal to each other. In addition, phase noise and ionospheric scale factors are close to each other.

4. SOFTWARE DEVELOPMENT

The cycle-slip detection methods can be categorized from simple to complex. To implement a detection method, it is necessary to follow the necessary steps in sequential order. During the development of these algorithms, the processing burden of the computer can increase significantly. For the steps to proceed sequentially and for retroactive arrangements to be made, it has become necessary to utilize programming languages and develop software for this purpose. In this context, there has been a search for a programming language that can accommodate a high processing burden, allows the mathematical operations of methods to be encoded in a simpler manner than other languages, and has an environment conducive to interface development.

The Matrix Laboratory (MATLAB) programming language has been chosen because it is simple to perform matrix operations, widely used in academic research, and creation of the user interface is much less complicated [79]. The programming language used, interface description, and function files created for the process steps will be described in detail.

4.1. Programming Language

MATLAB is a highly powerful and versatile programming language that provides numerous advantages to users in many fields. It is well-suited for numerical computation, data analysis, and data visualization due to its wide variety of built-in tools and functions. MATLAB is good at solving difficult mathematical problems, implementing complex algorithms, and simulating dynamic systems. Its simple syntax and user-friendly environment make it ideal for rapid prototyping and iteration. In addition, MATLAB offers seamless integration with other programming languages and software, allowing you to reuse existing code and collaborate with a variety of tools. MATLAB enables you to handle real-world issues swiftly and effectively, making it a useful asset in your computational toolkit whether you are a scientist, engineer, researcher, or student.

MATLAB is a commercial product, but its developers are eager to grant academic licenses. Alternatively, GNU Octave is available to other users, but it should be noted that

GNU Octave is not as rapid as MATLAB and does not contain some of the tools that MATLAB has.

In search of application development, the toolboxes of MATLAB were investigated. After examination, it was determined that the App Designer tool could be utilized. Previously, GUIDE was used for application development, and these applications can be challenging for individuals with limited knowledge and experience. App Designer has replaced the GUIDE as the standard interface design tool for MATLAB as a result of recent software updates. App Designer is an application development environment in MATLAB, which allows users to create interactive applications. App Designer simplifies the process of building MATLAB applications by providing a visual representation of the UI and allowing users to design the layout and appearance of their applications easily. It also provides an integrated editor for writing the underlying code that controls the application's functionality. It has been determined that App Designer is adequate for this academic application, and no other programming language or tool is required to create the UI.

4.1.1. Building up the Application

Information about the planning and development processes of the software to be developed for all the requirements described in Section 4.1 will be given in this section. The name "Cycle-Slip Methods Comparison Tool" was selected for the software. During the process of development, a UI has been created so that the results of the mathematical calculations and statistical tests do not need to be entered repeatedly into the function files. To avoid complexity, function files and scripts written for each stage are organized into folders. Each tab in the user interface corresponds to different stages of the software. These stages are listed in the order below:

1. File Importing
2. Parameter Selection
3. Method Selection
4. Cycle-Slip Insertion
5. Detection Analysis

4.1.2. File Import

“File Import” tab allows users to introduce the required files which will be used within the processes (Figure 4.1). These files include:

- RINEX Observation File version 3.0x
- Standard Product 3 File
- Clock Data File
- ANTEX File

To use the CSMCT, RINEX Observation File and Standard Product File is mandatory. RINEX observation files are required to gather the both carrier-phase and code-pseudorange observations. User must choose the satellite clock correction to calculate the coordinates of satellites precisely. Clock data or “.sp3” file must be selected to further the progress, otherwise the error message will pop-up.

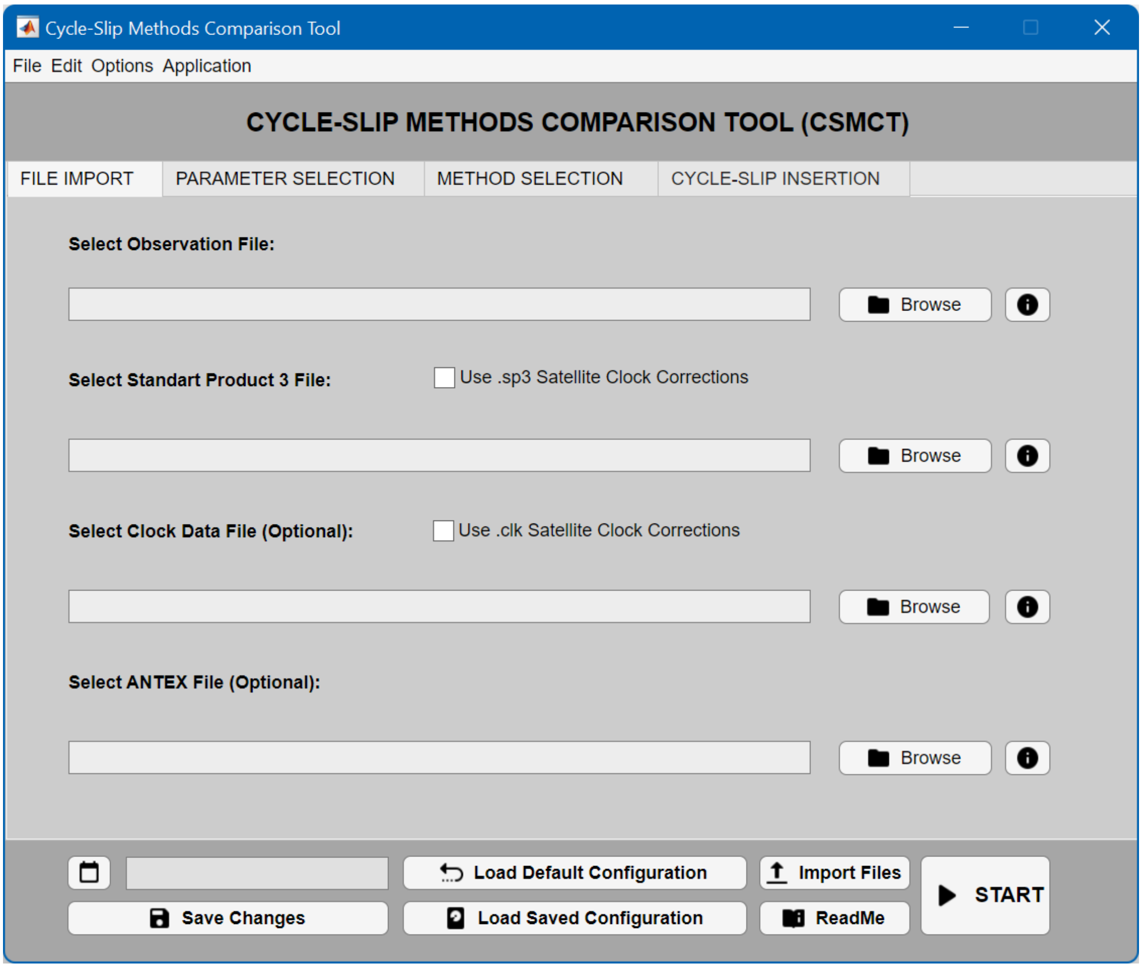

Figure 4.1. File Import Stage of CSCMT

After browsing, the locations of each of the files in the OS are shown so that users can check whether they have selected the correct file. Things to consider about file formats while selecting each file are shared with help buttons. If the files are not on the user's computer, the links to download them from the internet are also included in the UI.

For each of the files to be utilized in the subsequent steps, the data they contain must be collected and saved. Currently, only RINEX v3.0x files required for the observation data are available. The CSMCT divides RINEX v3.0x files into the "Header" and "Observation" sections. While the Header reads and saves all the data available in the RINEX v3.0x files, The "Observation" section collects and stores the (epoch x satellite number)-shaped observation data of the satellites. CSMCT can also read the values of signal strength and loss of lock indicators. SSI and LLI, which are important in detecting cycle-slips, are collected from the file and stored in a structure called "Indicators".

Standard Product (SP) files are precise orbital information files that were originally produced for GPS, but later on, with the creation of other GNSS constellations, they contain the orbit information needed and other data required for many applications. SP files provide the positions, velocity and clock corrections of satellites required for precise positioning.

These precise orbit information files, which are called SP3 as abbreviation and have the file extension with the same name (.sp3), are also produced and stored in a unique format. As the name suggests, these file types, which are a product, are produced by institutions. This data format, which was first produced in the 1980s, has been versioned a total of 3 times. SP1, which was the first produced version, was released, then SP2 and the version used today, SP3, are available. There are also four side versions of the SP3 main version. These versions are denoted by letters, from “a” to “d”. In addition, unlike RINEX observation files, the lines with the data are character-limited, which reduces the processing burden for software development processes for file reading.

Satellite clock corrections are one of the most important parameters for high-precision positioning performance of GNSS. Satellite clock corrections are also provided with the SP3 file format. The unit of these satellite clock corrections in the data part of the file is microseconds [22]. In addition to all of these files, antenna calibration files can also be used. These files are known as the antenna calibration files, known as ANTEX, are a standard format, used for correcting the phase center variations and phase center offsets of both receiver and satellite antennas. Users can simply browse these files to use it.

4.1.3. Parameter Selection

CSMCT can read all observation data in RINEX v3.0x. All GPS, GLONASS, Galileo, and BeiDou observation data can be saved, if available in the downloaded file. For this, from the UI, it will be sufficient to mark the constellations whose data is requested. With the rapid development of GNSS technology, the available frequencies have also increased. The frequencies in these four constellations are added in a checkbox-tree structure. In this regard, it is important to note that the checkbox-tree component was added to App Designer with the R2021a update of MATLAB. Users must install this update to use the program without experiencing any issues. If requested by the user, cycle-slip detection stages can be performed not only with legacy signals but also with modernized signals. It is emphasized because the number of possible signal combinations increases, allowing the success rates of cycle-slip detection to be improved. Another important thing to note that is at least one GNSS constellation must be selected. Although GPS is selected by default, all constellations that the user wants to select can be chosen either individually or together based on their particular requirements. Observations of the selected constellation are also marked in the "Available Frequencies" panel. The desired observations can be selected in the checkbox-tree structure of the constellation, or the default selected ones can be removed, but at least one observation must be selected.

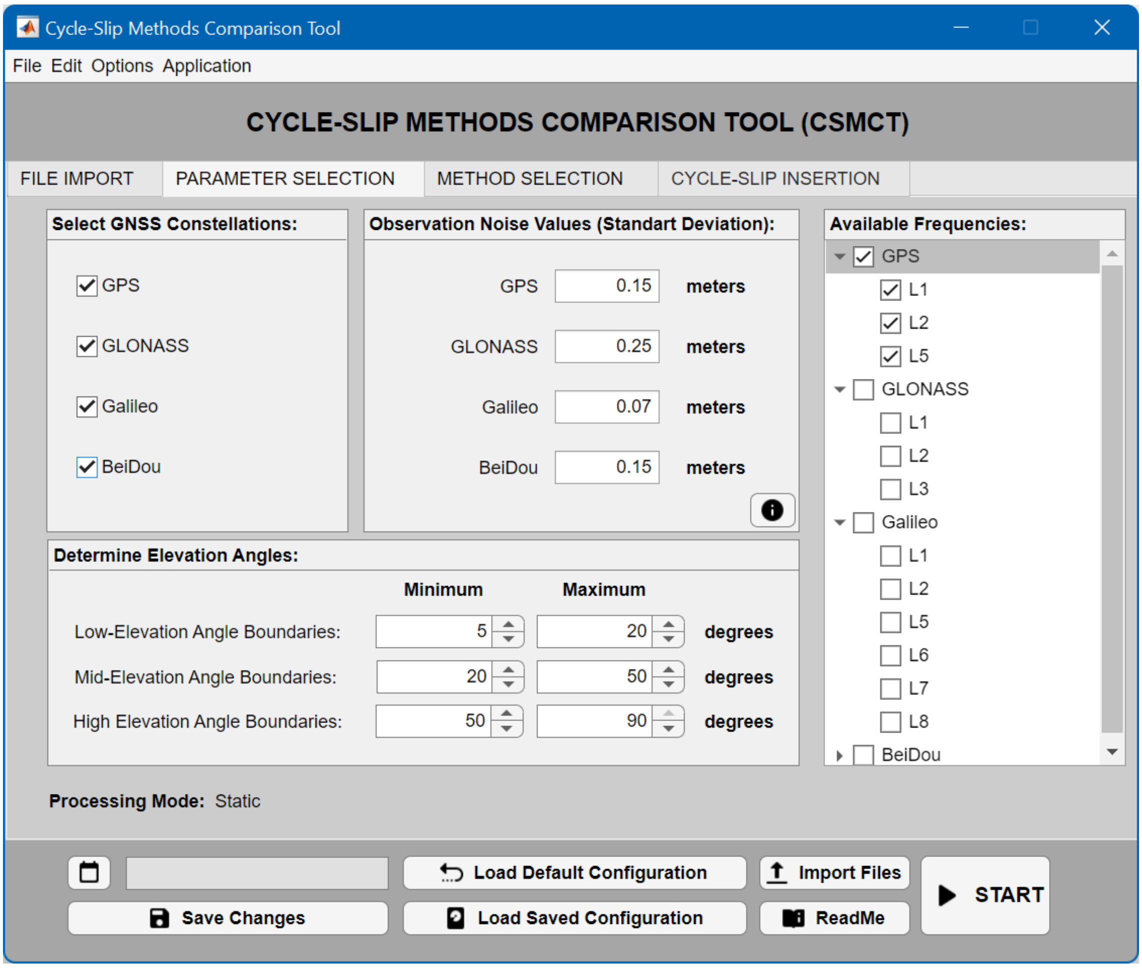

Select GNSS Constellations:

☑ GPS
☑ GLONASS
☑ Galileo
☑ BeiDou

Observation Noise Values (Standart Deviation):

GPS 0.15 meters
GLONASS 0.25 meters
Galileo 0.07 meters
BeiDou 0.15 meters

Determine Elevation Angles:

	Minimum	Maximum	
Low-Elevation Angle Boundaries:	5	20	degrees
Mid-Elevation Angle Boundaries:	20	50	degrees
High Elevation Angle Boundaries:	50	90	degrees

Available Frequencies:

- ☑ GPS
  - ☑ L1
  - ☑ L2
  - ☑ L5
- ☐ GLONASS
  - ☐ L1
  - ☐ L2
  - ☐ L3
- ☐ Galileo
  - ☐ L1
  - ☐ L2
  - ☐ L5
  - ☐ L6
  - ☐ L7
  - ☐ L8
- ☐ BeiDou

Processing Mode: Static

Figure 4.2. Parameter Selection Stage of CSMCT

The elevation angles of satellites are divided into three parts. Due to the GNSS signal's longer path through the atmosphere before reaching the receiver at low elevation angles, it is more susceptible to disturbance effects, resulting in a low SNR [80]. As satellite elevation angles increase, these effects occur less frequently. The user can distinguish these angles between the minimum edit-field of the “low-elevation angle boundaries” to maximum of the “high-elevation angle boundaries”, and establish their limits. The important things to note are as follows:

1. The minimum of the “low-elevation angle boundaries” is also set as the satellite elevation mask angle. The user has the option to increase this number as much as desired, but the minimum allowed value is 5°. For accurate determination of the satellite observation arcs, it should be noted that this number cannot exceed 20°.
2. The maximum of the “high-elevation angle boundaries” cannot exceed 90°. If the user enters a value greater than 90°, the system automatically replaces it with 90°.
3. The term low, mid and high elevation angle has been chosen only for the convenience of users who will choose between 5° and 90°. Users can select the maximum of the “high-elevation angle boundaries” below 90°.

4.1.4. Method Selection

Three different panels were created for CSMCT method selection. These panels are separated into single-frequency, dual-frequency, and triple-frequency methods. Each method may be selected individually or together. Notably, these methods are intended for use in a post-processing environment. Methods with varying frequencies cannot be combined. These methods have been carefully selected from the most well-known cycle-slip detection applications. With additional future updates, the vast majority of the GNSS community is going to be able to make use of it.

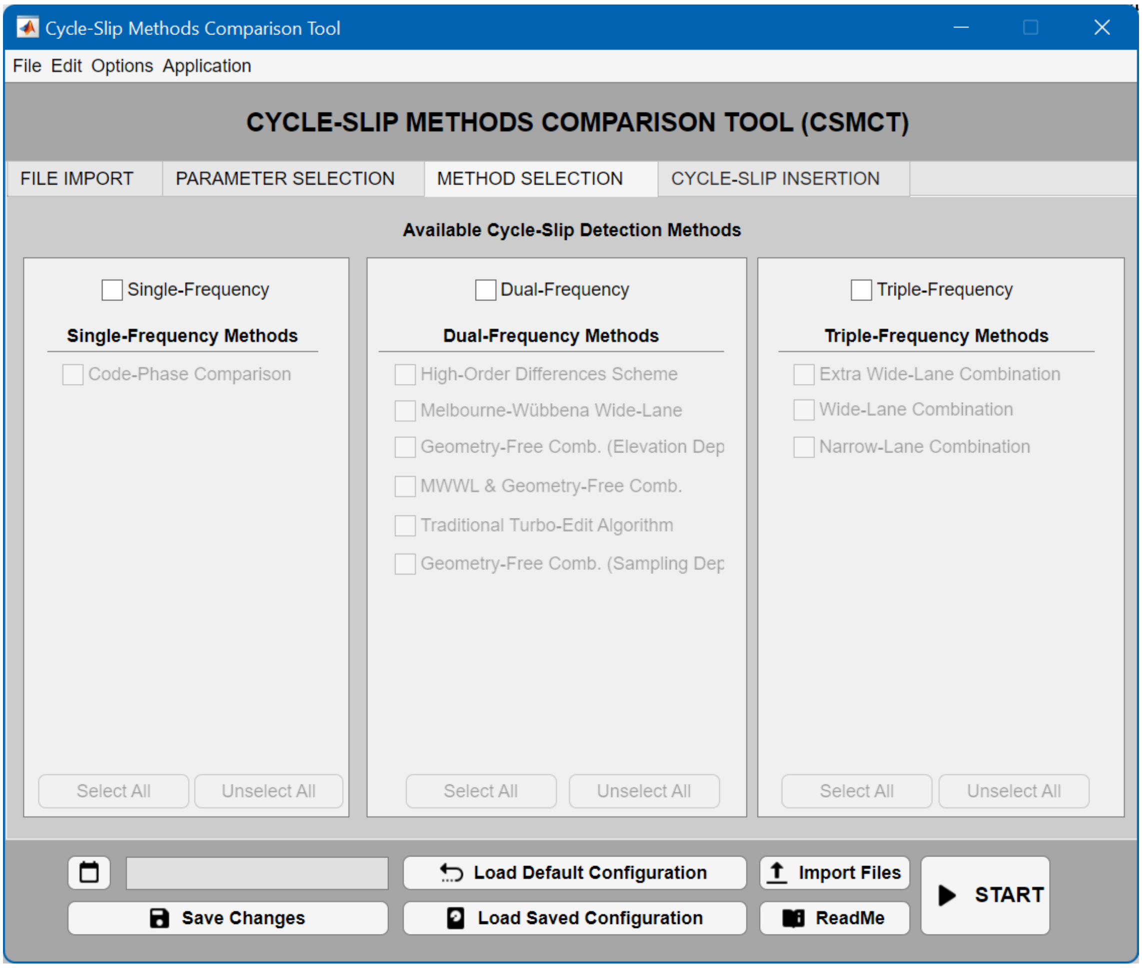

Figure 4.3. Method Selection Stage of CSMCT

4.1.5. Artificial Cycle-Slip Insertion

In some cases, cycle-slip detection algorithms may not work as expected with RINEX raw data. The reason for this is related to the conditions at the time the data was collected by the receiver. If these data are collected on days with high ionospheric activity or in an environment where it can be exposed to multipath effects and are not free of other errors mentioned in Section 2.7, the detection rate in the algorithms can decrease significantly. Once RINEX data can be manipulated with MATLAB, algorithms can be tested through inserting artificial cycle-slips into the observation data. In addition, algorithmic flaws and strengths can be identified, and more accurate results can be obtained in a variety of particular scenarios. In order to analyze how to obtain results with existing algorithms in various scenarios, CSMCT has been enhanced to allow for the insertion of artificial cycle-slip. These artificial cycle-slips are placed at a random epoch and amplitude in accordance with the nature of the occurrence of a cycle-slip.

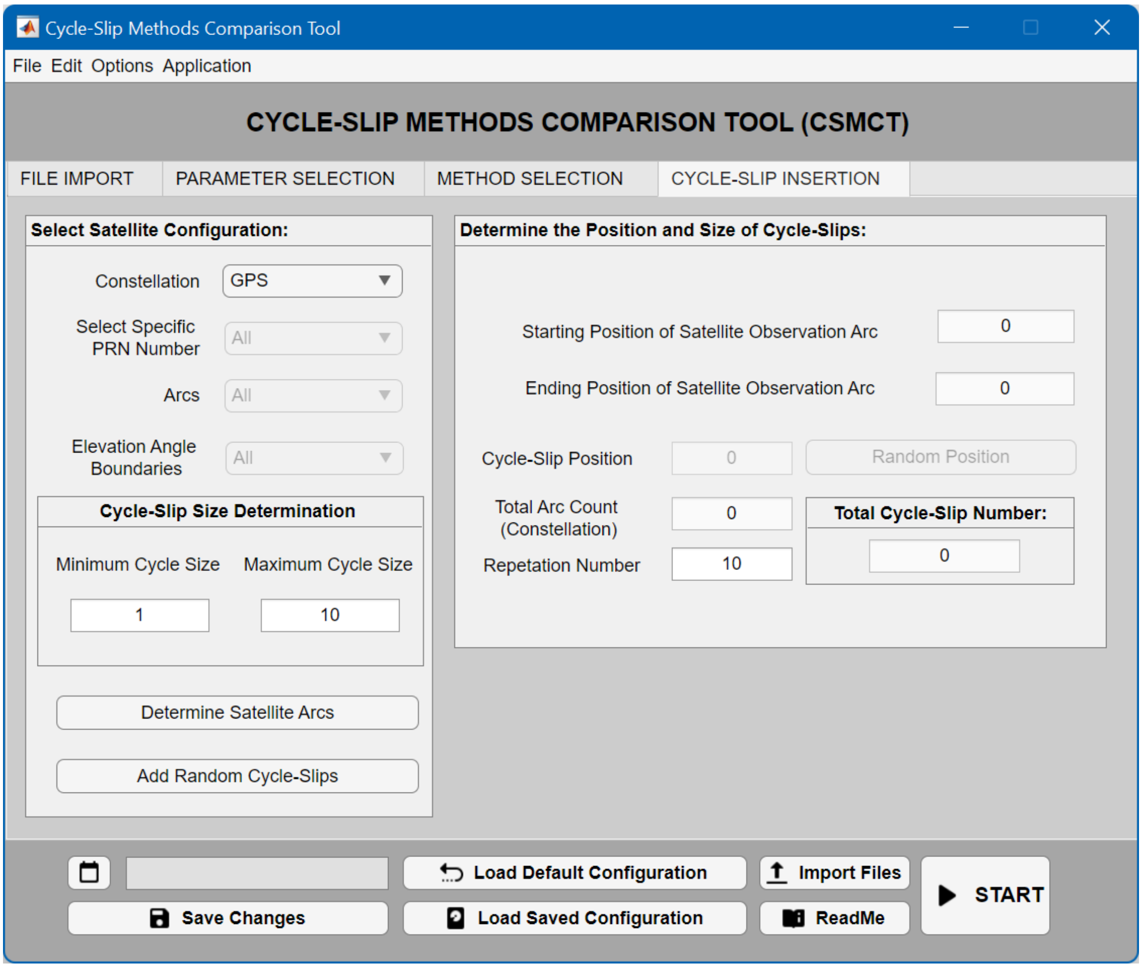

Select Satellite Configuration:

Constellation: GPS
Select Specific PRN Number: All
Arcs: All
Elevation Angle Boundaries: All

Cycle-Slip Size Determination

Minimum Cycle Size: 1
Maximum Cycle Size: 10

Determine the Position and Size of Cycle-Slips:

Starting Position of Satellite Observation Arc: 0
Ending Position of Satellite Observation Arc: 0
Cycle-Slip Position: 0
Total Arc Count (Constellation): 0
Repetation Number: 10
Total Cycle-Slip Number: 0

Figure 4.4. Cycle-Slip Insertion Stage of CSMCT

All parameters selected in the first three stages must be processed and saved with the “Import Files” button. If the “Import Files” button is not used, CSMCT cannot perform any operation. After clicking the “Import Files” button, it takes approximately 25-75 seconds depending on the size of the file. After the successful process of reading the files, the data will be saved and the application will send the parameters selected by the user to the next step. Subsequently, it is necessary to determine the continuous satellite observation arcs for each constellation from the obtained observation data. Because satellites cannot receive data in all epochs of the day. The artificial cycle-slips should be added within the data-receiving intervals. Otherwise, adding only a few centimeters of observations to the currently empty observation data results in extremely erroneous outputs from all functions using observation data. To prevent this issue, the limits of the data ranges were determined and data-editing outside of these limits was prohibited.

An algorithm has been developed that inserts artificial cycle-slips into the data. This algorithm initially retrieves all satellite information for the selected constellation. If artificial cycle-slips are to be inserted on all satellites, the default value may be preserved. In addition, cycle-slip insertion can be made on only one selected satellite with CSMCT. Based on this, it is determined how many observation arcs each satellite has. Thus, it must be determined whether data will be inserted to all satellite observation arcs or to a single observation arc. In addition, CSMCT can also input data only to arcs within the desired limits by dividing these arcs according to specified intervals.

The test performance of the algorithms can be examined by selecting the amplitude of the cycle-slip to be added. In most detection methods, algorithms are less likely to catch cycle-slips at low cycle sizes. In addition, for dual frequency, if the amplitudes of the cycle-slips placed at different frequencies are the same, the algorithms cannot determine these cycle-slips (e.g., Melbourne-Wübbena Combination).

If all PRN and arcs are included in the process, the total arcs of the satellites in all constellations are displayed in the “Total Arc Count” heading in the upper right panel. The key points are as follows:

1. In the first iteration, the cycle-slip index equal to the number of “Total Arc Count” is determined to be randomly distributed in each observation arc. It is aimed to create a normal distribution for elevation angles by repeating this procedure as many as the number of iterations selected by the user. The following formula is used to calculate the total number of cycle-slips to be included:

$$\text{Total Cycle-Slip} = \text{Total Arc Count} * \text{Repetition Number} \tag{4.1}$$

2. If one of the three elevation angle ranges are chosen to place the cycle-slips, the observation arcs are divided according to these intervals. The individual satellite is excluded from the operations if there are no observation arcs that can be divided into intervals determined in the data of the satellites. Cycle-slip attributes data is not filled while the data of the related satellite is reflected in the result table.
3. After the cycle-slip indexes are determined, amplitude determinations are made. Size selections cannot be determined randomly. The reason for this is that the cycle-slip sizes are categorized within the scope of the thesis.

4. After the user determines cycle-slip sizes, these are written into the data. However, the algorithm does not allow the same cycle-slip sizes to be inserted. The reason for this is that if there are insensitive cycle-slip pairs, the discarded sizes will not be detected, and the success rate of the created scenario will decrease.

4.1.6. Detection Analysis

While all of the operations specified in the first four items are carried out in the CSMCT interface, an auxiliary application has been created for the analysis stage. In this application, graphical representations of continuous satellite observation arcs derived from RINEX v3.0x and SP3 data are displayed. Users are also presented with a table containing the metadata of artificial cycle-slips.

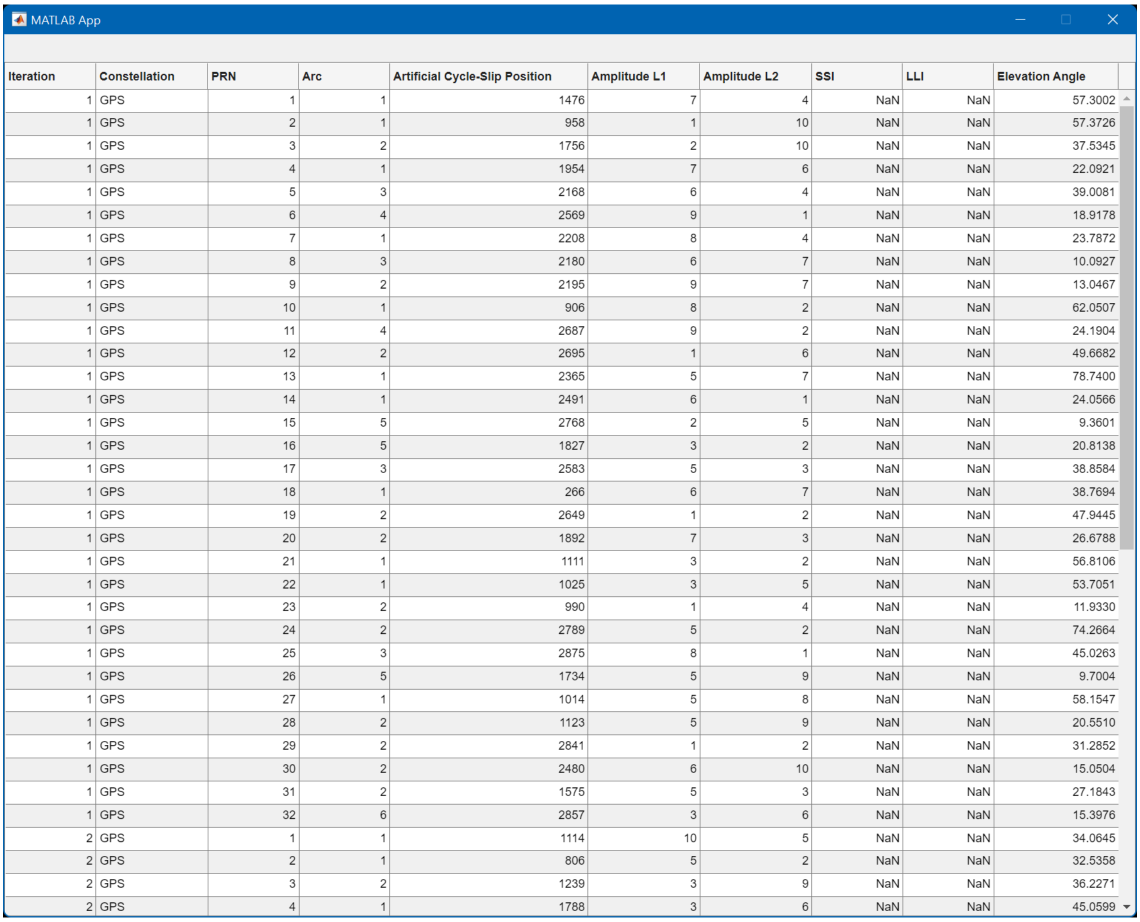

Iteration	Constellation	PRN	Arc	Artificial Cycle-Slip Position	Amplitude L1	Amplitude L2	SSI	LLI	Elevation Angle
1	GPS	1	1	1476	7	4	NaN	NaN	57.3002
1	GPS	2	1	958	1	10	NaN	NaN	57.3726
1	GPS	3	2	1756	2	10	NaN	NaN	37.5345
1	GPS	4	1	1954	7	6	NaN	NaN	22.0921
1	GPS	5	3	2168	6	4	NaN	NaN	39.0081
1	GPS	6	4	2569	9	1	NaN	NaN	18.9178
1	GPS	7	1	2208	8	4	NaN	NaN	23.7872
1	GPS	8	3	2180	6	7	NaN	NaN	10.0927
1	GPS	9	2	2195	9	7	NaN	NaN	13.0467
1	GPS	10	1	906	8	2	NaN	NaN	62.0507
1	GPS	11	4	2687	9	2	NaN	NaN	24.1904
1	GPS	12	2	2695	1	6	NaN	NaN	49.6682
1	GPS	13	1	2365	5	7	NaN	NaN	78.7400
1	GPS	14	1	2491	6	1	NaN	NaN	24.0566
1	GPS	15	5	2768	2	5	NaN	NaN	9.3601
1	GPS	16	5	1827	3	2	NaN	NaN	20.8138
1	GPS	17	3	2583	5	3	NaN	NaN	38.8584
1	GPS	18	1	266	6	7	NaN	NaN	38.7694
1	GPS	19	2	2649	1	2	NaN	NaN	47.9445
1	GPS	20	2	1892	7	3	NaN	NaN	26.6788
1	GPS	21	1	1111	3	2	NaN	NaN	56.8106
1	GPS	22	1	1025	3	5	NaN	NaN	53.7051
1	GPS	23	2	990	1	4	NaN	NaN	11.9330
1	GPS	24	2	2789	5	2	NaN	NaN	74.2664
1	GPS	25	3	2875	8	1	NaN	NaN	45.0263
1	GPS	26	5	1734	5	9	NaN	NaN	9.7004
1	GPS	27	1	1014	5	8	NaN	NaN	58.1547
1	GPS	28	2	1123	5	9	NaN	NaN	20.5510
1	GPS	29	2	2841	1	2	NaN	NaN	31.2852
1	GPS	30	2	2480	6	10	NaN	NaN	15.0504
1	GPS	31	2	1575	5	3	NaN	NaN	27.1843
1	GPS	32	6	2857	3	6	NaN	NaN	15.3976
2	GPS	1	1	1114	10	5	NaN	NaN	34.0645
2	GPS	2	1	806	5	2	NaN	NaN	32.5358
2	GPS	3	2	1239	3	9	NaN	NaN	36.2271
2	GPS	4	1	1788	3	6	NaN	NaN	45.0599

Figure 4.5. Auxiliary Application of CSMCT

Each row represents an inserted cycle slip into a specific satellite observation arc and includes all metadata of the artificial cycle slip. The amplitudes of cycle-slips vary between 1 to 10 in Figure 4.5. The SSI and LLI values of each artificial cycle-slip are shown. The values in the “Iteration” column indicate how many times the application added artificial cycle-slips in the observation structure.

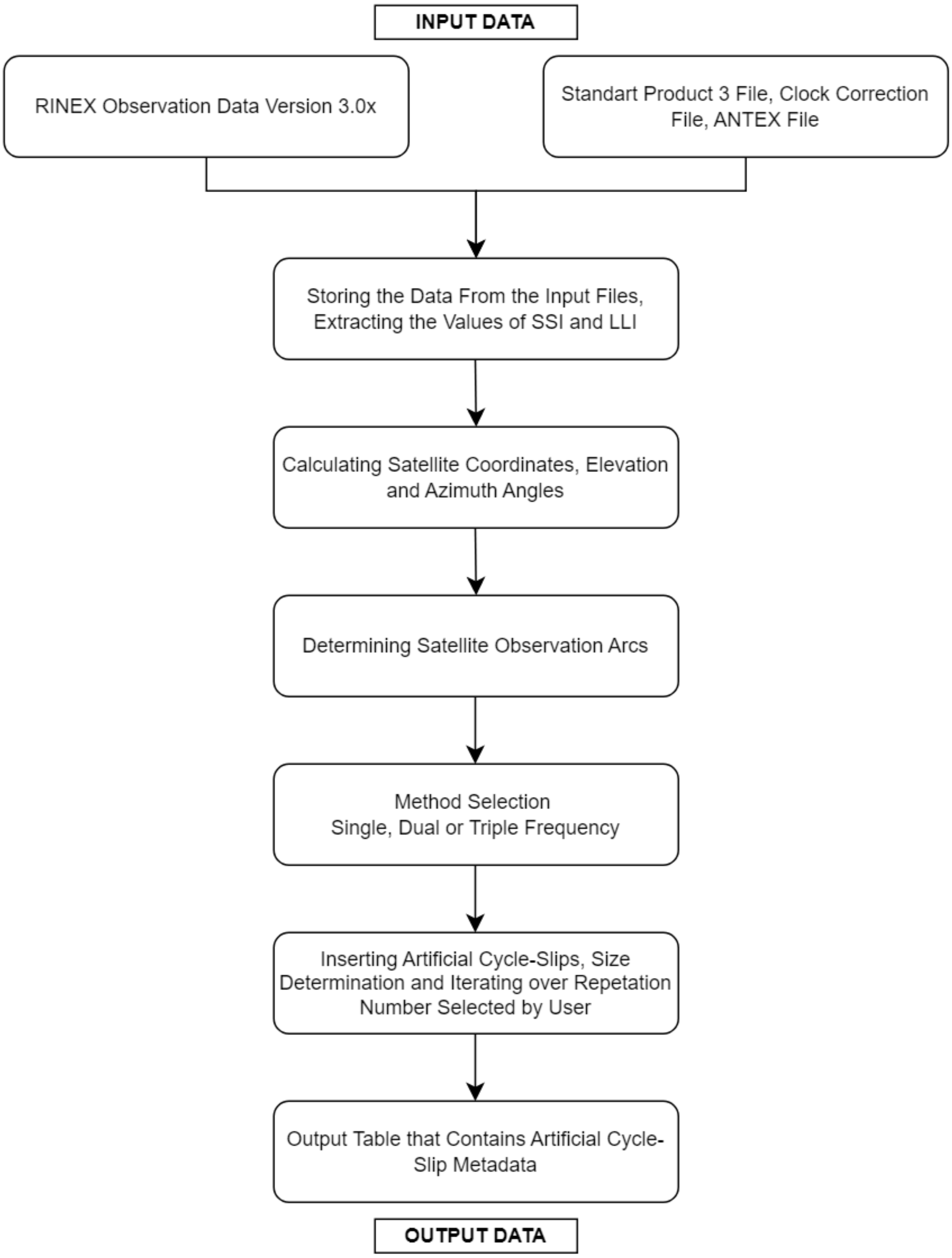

Figure 4.6. Work Diagram of CSMCT

5. COMPARISON OF CYCLE-SLIP DETECTION METHODS WITH CSMCT

In this chapter, there will be detailed analysis of the success of the methods in the light of the results of the CSMCT software created for obtaining the necessary data and comparing the cycle-slip detection methods.

5.1. Description of the Data

First, a test study was conducted for the algorithm to be executed behind the interface proposed. For this test, two different datasets were constructed over the course of two days. It has been determined that the first day will have strong ionospheric activity, while the second day will have average activity. Care was taken to select the datasets spread around the world, and attention was paid to include at least three frequencies for GPS, GLONASS, Galileo and BeiDou constellations. The datasets are added to the datasets folder of CSMCT, by adding all the necessary files for file import, thus enabling other users to test the same algorithms later.

The datasets for the test run will be in one day long, MIXED observation file in Hatanaka compressed format. All observation files must be downloaded in the MIXED format, and all constellations that CSMCT can read have been included. For the days of testing, observation files, precise ephemerides files (with the extension ".sp3"), and clock data files for satellite clock error are downloaded from the related webpages.

Observation files to be downloaded within the scope for the test are in RINEX format. This format is available in NASA's daily archive with ".crx" extension and the files are converted to RINEX ".rnx" format by Hatanaka conversion [81]. Precise ephemerides files with ".sp3" extension in ASCII format can be used without any conversion. In addition, clock product files for correcting satellite clock errors are also downloaded from IGS as well as CDDIS and containing corrections according for GPS, GLONASS, Galileo and BeiDou. For ANTEX files, version 1.4 can be used. The data sampling intervals for RINEX files are 30 seconds, for ".sp3" files are 300 seconds and for clock correction files, it is 30 seconds. They are well-suited for multi-GNSS.

Four stations are selected for the cycle-slip detection experiment. In the observation data collected by these stations, there are at least three different frequencies for each GNSS constellation. All observation data in the RINEX observation files generated by these stations were successfully read by CSMCT. The metadata of the stations for the cycle-slip detection experiment are listed in Table 5.1:

Table 5.1. Stations selected for the case study and their attributes

Station Name	Country Code	Country Name	Latitude	Longitude
PTRF	CAN	Canada	48.54420	-124.41299
FFMJ	DEU	Germany	50.09058	8.66497
LPGS	ARG	Argentina	-34.90674	-57.93230
MIZU	JPN	Japan	39.13517	141.13283

The RINEX observation data of each of these stations were downloaded for the dates 27.02.2023 and 25.05.2023. The reason for choosing these dates is to examine the effects of the ionosphere, which is one of the biggest influences on the success rates of cycle-slip detection methods for single, dual and triple-frequency. One of the most important reasons for using Kp indexes is that the activity of the ionosphere can be understood much more easily during the day and in addition, Kp indexes are categorized with values between 0-9 [82]. This categorization is in the Table 5.2:

Table 5.2. Kp-index categorization

Kp-Index	Interval
0 - 1	Very Quiet, Steady
1 - 4.5	Moderately Active
4.5 - 9	Highly Active

Data on this effect are kept by the GFZ-Potsdam in three-hour periods. The intervals of Kp index data of GFZ Potsdam shown in Table 5.2. Daily average of Kp indexes for the day 27.02.2023 is 6.21 and for the day 25.05.2023 is 2.42, respectively.

Geomagnetic Kp indexes are quietly moderate unlike the first day. The values on the first day indicate a serious geomagnetic activity. Since the most active geomagnetic effects in three-hour periods in 2023 were detected on this day, the first dataset for the case study was created from the collected station data of this day. The second dataset was formed from the station data collected from the second day.

For cycle-slip detection experiment, single, dual and triple-frequency observations are needed. For each of these observations, civilian signals of each GNSS constellation have been determined. These signals are selected from those generally preferred in cycle-slip detection methods found in the literature. The frequencies to be processed in the case study, for each GNSS constellation, are shown in Table 5.3:

Table 5.3. Frequencies selected for cycle-slip detection in each GNSS constellation

	Constellation			
Frequencies	**GPS**	**GLONASS**	**Galileo**	**BeiDou**
Single-Frequency	L1	G1	E1	B1
Dual-Frequency	L1, L2	G1, G2	E1, E5a	B1, B2
Triple-Frequency	L1, L2, L5	G1, G2, G3	E1, E5a, E5b	B1, B2, B3

The values of each frequency listed here are shown in Table 2.1.

5.2. Test Scenario

RINEX observation files have been converted to tabular format and divided into two separate categories as “RINEX Header” and “RINEX Observation”, and “.m” file of each these categories have been produced. All the data that will be needed in the algorithm have been recorded in “RINEX Header” and the parts containing detailed information have been added to the result output. With the “RINEX Observation” file, the observations of single, dual and triple-frequency signals were arranged and recorded for each satellite available in the file.

In order to obtain satellite-clock errors of the observations and the velocity and positions of the satellites, corrections taken from the “.sp3” file were included in the processes and accuracy was increased. Parameters taken from the “.sp3” file will be used to calculate the coordinates of the satellites. In addition, the effects of satellite clock errors have been minimized and the required accuracy for satellite elevation angles has been carefully studied. Clock jumps have to be eliminated to increase the accuracy of the scheme of differences [70]. For each step that is not calculated precisely, many epochs actually included in the algorithm can be lost.

In the next step, satellite coordinates and satellite elevation angles were calculated. While calculating the satellite coordinates, all necessary corrections in the “.sp3”, “.clk” and “.atx” files were made to calculate the coordinates precisely. Within the scope of the cycle-slip detection experiment, single, dual and triple-frequency cycle-slip detection success rates will be evaluated according to elevation angles. Satellite coordinates and satellite elevation angles were calculated for each observed epoch. By calculating the satellite elevation angles and satellite coordinates, the intervals at which each satellite transmits uninterrupted signals are determined. In the datasets produced daily, the majority of satellites do not give uninterrupted signals. Removing many empty sections in the process phase speeds up the steps, making them look simpler and easier.

In the process, these satellite elevation angles are categorized and are divided into three as low, medium and high elevation angles. These satellite elevation angle ranges were chosen as follows:

- Low elevation angle intervals: 5°- 20°
- Mid elevation angle intervals: 20° - 50°
- High elevation angle intervals: 50° - 90°

respectively. This is to examine the effects of satellite elevation angles on cycle-slip detection algorithms. In general, the minimum acceptable elevation angle should be between 5° and 8°. In this experiment, the satellite elevation mask angle is chosen as 5°. This is because as many epochs as possible are required to be tested.

First, the positions of the randomly selected cycle-slips in the divided continuous observation arcs were determined. For each arc, cycle-slips are placed with random locations.

In addition, the amplitude of each inserted cycle-slip has been determined in accordance with the nature of its occurrence. These amplitudes are randomly placed within the specified ranges. These intervals will be in the range of (1-10) and (10-100) cycles. The important part in this is that all cycle-slip values must be an integers. The obtained values were recorded as “Success Rate” values. These values were obtained from the number of artificial cycle-slips caught by the algorithms.

The total number of artificially added cycle-slips is obtained by multiplying the number on which the algorithm is looped by the total continuous observation arcs. All of the obtained values are given in the tables in Section 5.3. In the table, “Rep Num” means how many times the software iterated over, “Inserted CS” represents the total artificially added cycle-slips, “Small CS” is the 1-10 cycle intervals, “Large CS” represents 10-100 cycle intervals.

The cycle-slip detection methods used in this experiment for single, dual and triple frequencies are listed in Table 5.4:

Table 5.4. Cycle-slip detection methods for each frequency

Frequencies	**Cycle-Slip Detection Methods List**
Single-Frequency	1) Code-Phase Comparison
Dual-Frequency	1) Scheme of Differences 2) Melbourne-Wübbena Wide-Lane Combination (MWWL) 3) Geometry-Free Combination with Elevation Dependent Threshold 4) MWWL and Geometry-Free Combined Method 5) Traditional Turbo-Edit Algorithm 6) Geometry-Free Combination with Sampling Interval Threshold
Triple-Frequency	1) Extra Wide-Lane Combination 2) Wide-Lane Combination 3) Narrow-Lane Combination

With the algorithm, the existing cycle-slips were cleaned. The reason for this is that in the process of detecting the cycle-slips added artificially, other cycle-slips in the data are also detected and it is requested not to reduce the accuracy of the evaluation to be made. With the raw form of the cleaned data, the other steps of the algorithm were initialized.

5.2.1. Performance Evaluation of Cycle-Slip Detection Methods

Here, the results of all CSMCT-based tests of the aforementioned processes will be described. Each table listed here contains the results obtained by processing the original station observations as part of the cycle-slip detection experiment. These results were categorized according to single, dual and triple-frequency observations. In addition, the data obtained are grouped according to ionospheric delays.

5.2.2. Results for Single-Frequency Cycle-Slip Detection

CSMCT uses the code-phase comparison method described in Section 3.3.1 for single-frequency cycle-slip detection. The success rate of code-phase comparison is affected by constellation-wise code-pseudorange observation noises. The threshold values used for single-frequency cycle-slip detection is derived from standard deviation of code-pseudorange observation noise values. When the code-observation noises are amplified, the success rates of cycle-slip detection decrease. From the literature [83,84], code-observation noise values for single-frequency, for GPS, it is 0.15 m, for GLONASS, it is 0.25 m, for Galileo, it is 0.08 and for BeiDou, it is 0.15 m. According to the code-observation noise values, the success rates of detecting cycle-slips is higher with Galileo system and the lowest of them with GLONASS. Tables for the day 27.02.2023 and 25.05.2023 with single-frequency algorithm are as follows:

Table 5.5 PTRF-CAN station results for single-frequency for the day 27.02.2023

Constellation	**Elevation Angle Boundaries**	**Rep. Number**	**Inserted CS**	**Small CS (1-10)%**	**Large CS (10-100)%**	**Method**
GPS	All	110	8580	79.19	98.58	1
GLONASS	All	120	7560	62.45	97.42	1
Galileo	All	150	6660	94.90	99.15	1
BeiDou	All	140	7280	83.50	99.40	1
GPS	Low	110	8580	79.11	98.44	1
GLONASS	Low	120	7560	63.27	96.77	1
Galileo	Low	150	6660	94.99	99.30	1
BeiDou	Low	140	7280	83.67	99.27	1
GPS	Mid	110	5720	78.57	100	1
GLONASS	Mid	120	4680	62.57	98.55	1
Galileo	Mid	150	4650	95.47	99.98	1
BeiDou	Mid	140	4760	82.99	100	1
GPS	High	110	3520	81.23	100	1
GLONASS	High	120	2880	56.59	97.39	1
Galileo	High	150	2400	96.04	100	1
BeiDou	High	140	7280	83.05	99.96	1

Table 5.6. FFMJ-DEU station results for single-frequency for the day 27.02.2023

Constellation	**Elevation Angle Boundaries**	**Rep. Number**	**Inserted CS**	**Small CS (1-10)%**	**Large CS (10-100)%**	**Method**
GPS	All	110	7590	79.64	99.17	1
GLONASS	All	120	7440	50.85	96.35	1
Galileo	All	150	5100	95.80	100	1
BeiDou	All	110	8030	95.64	99.47	1
GPS	Low	110	7590	80.12	99.47	1
GLONASS	Low	120	7320	51.08	96.19	1
Galileo	Low	150	5100	95.72	99.98	1
BeiDou	Low	110	8030	96.00	99.20	1
GPS	Mid	110	5940	80.96	99.76	1
GLONASS	Mid	120	5400	46.50	96.50	1
Galileo	Mid	150	4200	96.32	100	1
BeiDou	Mid	110	5830	95.07	99.86	1
GPS	High	110	3300	82.95	100	1
GLONASS	High	120	3000	58.16	100	1
Galileo	High	150	3000	96.14	99.58	1
BeiDou	High	110	2750	96.52	100	1

Table 5.7. MIZU-JPN station results for single-frequency for the day 27.02.2023

Constellation	**Elevation Angle Boundaries**	**Rep. Number**	**Inserted CS**	**Small CS (1-10)%**	**Large CS (10-100)%**	**Method**
GPS	All	120	7200	72.37	99.46	1
GLONASS	All	140	7280	63.36	97.54	1
Galileo	All	200	6200	90.25	98.37	1
BeiDou	All	100	7900	87.96	99.36	1
GPS	Low	120	7200	72.50	99.29	1
GLONASS	Low	140	7280	63.53	97.75	1
Galileo	Low	200	6200	90.08	97.76	1
BeiDou	Low	100	7500	89.19	99.46	1
GPS	Mid	120	5760	73.29	99.88	1
GLONASS	Mid	140	5040	62.49	97.82	1
Galileo	Mid	200	5000	91.50	100	1
BeiDou	Mid	100	5600	88.72	99.91	1
GPS	High	120	4080	77.60	99.90	1
GLONASS	High	140	3780	64.91	97.09	1
Galileo	High	200	3400	92.34	100	1
BeiDou	High	100	3700	88.92	100	1

Table 5.8. LPGS-ARG station results for single-frequency for the day 27.02.2023

Constellation	**Elevation Angle Boundaries**	**Rep. Number**	**Inserted CS**	**Small CS (1-10)%**	**Large CS (10-100)%**	**Method**
GPS	All	100	7700	73.33	98.18	1
GLONASS	All	130	7020	54.78	90.29	1
Galileo	All	130	7150	95.53	99.37	1
BeiDou	All	110	7590	88.07	98.93	1
GPS	Low	100	7600	72.36	97.09	1
GLONASS	Low	130	6890	55.06	88.89	1
Galileo	Low	130	7020	95.33	99.39	1
BeiDou	Low	110	7590	87.21	98.11	1
GPS	Mid	100	4900	74.17	99.65	1
GLONASS	Mid	130	4550	54.16	97.44	1
Galileo	Mid	130	3640	95.98	100	1
BeiDou	Mid	110	4290	87.11	99.88	1
GPS	High	100	2900	74.29	100	1
GLONASS	High	130	3250	54.44	96.70	1
Galileo	High	130	2210	95.23	100	1
BeiDou	High	110	2750	89.13	100	1

Table 5.9. FFMJ-DEU station results for single-frequency for the day 25.05.2023

Constellation	Elevation Angle Boundaries	Rep. Number	Inserted CS	Small CS (1-10)%	Large CS (10-100)%	Method
GPS	All	110	7150	81.75	99.86	1
GLONASS	All	120	6840	61.50	98.50	1
Galileo	All	170	6970	95.43	99.47	1
BeiDou	All	100	6700	95.61	99.64	1
GPS	Low	110	7150	81.52	99.70	1
GLONASS	Low	120	6840	59.11	98.68	1
Galileo	Low	170	6970	95.22	99.35	1
BeiDou	Low	100	6700	96.03	99.53	1
GPS	Mid	110	5720	81.11	99.02	1
GLONASS	Mid	120	5160	59.59	99.35	1
Galileo	Mid	170	5100	96.09	100	1
BeiDou	Mid	100	5100	96.38	99.98	1
GPS	High	110	3520	82.55	100	1
GLONASS	High	120	3000	61.53	100	1
Galileo	High	170	3060	96.82	100	1
BeiDou	High	100	2500	97.42	100	1

Table 5.10. PTRF-CAN station results for single-frequency for the day 25.05.2023

Constellation	Elevation Angle Boundaries	Rep. Number	Inserted CS	Small CS (1-10)%	Large CS (10-100)%	Method
GPS	All	100	7900	82.94	98.76	1
GLONASS	All	120	8040	70.24	98.38	1
Galileo	All	190	7980	95.22	99.49	1
BeiDou	All	150	7800	85.48	99.44	1
GPS	Low	100	7800	84.28	98.66	1
GLONASS	Low	120	8040	70.18	97.80	1
Galileo	Low	190	7980	95.51	99.72	1
BeiDou	Low	150	7800	86.48	99.29	1
GPS	Mid	100	5200	82.98	99.86	1
GLONASS	Mid	120	4200	65.69	100	1
Galileo	Mid	190	5700	95.17	99.69	1
BeiDou	Mid	150	5100	84.22	99.76	1
GPS	High	100	3100	84.13	100	1
GLONASS	High	120	2760	70.78	100	1
Galileo	High	190	3230	95.36	100	1
BeiDou	High	150	2850	84.30	100	1

Table 5.11. LPGS-ARG station results for single-frequency for the day 25.05.2023

Constellation	Elevation Angle Boundaries	Rep. Number	Inserted CS	Small CS (1-10)%	Large CS (10-100)%	Method
GPS	All	100	7600	73.28	97.73	1
GLONASS	All	170	7650	57.67	98.32	1
Galileo	All	120	7920	94.37	98.82	1
BeiDou	All	120	8040	91.25	99.08	1
GPS	Low	100	7400	71.25	96.36	1
GLONASS	Low	170	7480	60.04	96.72	1
Galileo	Low	120	7920	93.37	98.62	1
BeiDou	Low	120	7800	90.92	98.48	1
GPS	Mid	100	5100	75.58	100	1
GLONASS	Mid	170	5780	53.14	96.26	1
Galileo	Mid	120	3360	96.42	100	1
BeiDou	Mid	120	4920	90.31	100	1
GPS	High	100	3000	75.28	100	1
GLONASS	High	170	4080	55.02	100	1
Galileo	High	120	2160	96.37	100	1
BeiDou	High	120	3000	88.58	100	1

Table 5.12. MIZU-JPN station results for single-frequency for the day 25.05.2023

Constellation	Elevation Angle Boundaries	Rep. Number	Inserted CS	Small CS (1-10)%	Large CS (10-100)%	Method
GPS	All	120	7440	72.16	98.81	1
GLONASS	All	150	7200	63.13	99.40	1
Galileo	All	200	7000	90.66	99.53	1
BeiDou	All	100	7600	87	99.50	1
GPS	Low	120	7440	71.11	98.40	1
GLONASS	Low	150	7200	63.21	99.19	1
Galileo	Low	200	7000	91.51	98.99	1
BeiDou	Low	100	7300	87.04	99.28	1
GPS	Mid	120	5400	73.83	99.94	1
GLONASS	Mid	150	5400	62.88	99.70	1
Galileo	Mid	200	5200	90.60	99.34	1
BeiDou	Mid	100	5600	87.97	100	1
GPS	High	120	3840	75.24	100	1
GLONASS	High	150	3750	64.72	100	1
Galileo	High	200	3600	92.06	100	1
BeiDou	High	100	3800	85.54	100	1

5.2.4. Results for Dual-Frequency Cycle-Slip Detection

A total of six methods have been used for dual-frequency cycle-slip detection. For different elevation angle boundaries have been used for each GNSS constellation. At least 100 repetitions applied to each continuous satellite observation arc. For each method and elevation angle boundaries, sufficient number of artificial cycle-slips have been inserted. The size of artificial cycle-slips insertions for each observation epoch have been divided into groups as (1-10) and (10-100) integer-cycles. The success rates of each station for dual-frequency cycle-slip detection methods for each day and method have been listed from Table 5.13 through Table 5.43:

Table 5.13. PTRF-CAN station results for dual-frequency GPS observations for the day 27.02.2023

Constellation	**Elevation Angle Boundaries**	**Rep. Number**	**Inserted CS**	**Small CS (1-10)%**	**Large CS (10-100)%**	**Method**
GPS	All	120	9600	74.84	92.32	1
GPS	All	120	9600	75.02	97.92	2
GPS	All	120	9600	96.12	98.31	3
GPS	All	120	9600	83.09	95.42	4
GPS	All	120	9600	75.5	94.09	5
GPS	All	120	9600	94.86	97.91	6
GPS	Low	120	9360	73.82	90.6	1
GPS	Low	120	9360	73.25	97.86	2
GPS	Low	120	9360	95.48	98.29	3
GPS	Low	120	9360	74.58	93.92	4
GPS	Low	120	9360	63.18	92.28	5
GPS	Low	120	9360	94.72	97.72	6
GPS	Mid	120	6240	77.58	97.37	1
GPS	Mid	120	6240	78.66	99.87	2
GPS	Mid	120	6240	98.59	99.77	3
GPS	Mid	120	6240	90.96	98.64	4
GPS	Mid	120	6240	84.51	97.79	5
GPS	Mid	120	6240	96.62	99.56	6
GPS	High	120	3840	78.85	96.64	1
GPS	High	120	3840	79.88	99.62	2
GPS	High	120	3840	99.27	99.63	3
GPS	High	120	3840	99.19	99.19	4
GPS	High	120	3840	98.49	99.09	5
GPS	High	120	3840	96.69	99.33	6

Table 5.14. PTRF-CAN station results for dual-frequency GLONASS observations for the day 27.02.2023

Constellation	**Elevation Angle Boundaries**	**Rep. Number**	**Inserted CS**	**Small CS (1-10)%**	**Large CS (10-100)%**	**Method**
GLONASS	All	140	9660	73.90	92.62	1
GLONASS	All	140	9660	68.67	90.66	2
GLONASS	All	140	9660	89.33	91.30	3
GLONASS	All	140	9660	73.08	88.71	4
GLONASS	All	140	9660	63.84	86.72	5
GLONASS	All	140	9660	92.73	95.76	6
GLONASS	Low	140	9100	72.69	91.29	1
GLONASS	Low	140	9100	93.05	94.85	2
GLONASS	Low	140	9100	71.83	95.83	3
GLONASS	Low	140	9100	67.83	90.13	4
GLONASS	Low	140	9100	55.95	88.18	5
GLONASS	Low	140	9100	92.41	95.56	6
GLONASS	Mid	140	5460	77.89	96.69	1
GLONASS	Mid	140	5460	77.29	97.26	2
GLONASS	Mid	140	5460	96.37	97.84	3
GLONASS	Mid	140	5460	86.88	96.45	4
GLONASS	Mid	140	5460	79.36	95.49	5
GLONASS	Mid	140	5460	93.95	97.54	6
GLONASS	High	140	3360	77.95	97.83	1
GLONASS	High	140	3360	76.77	96.02	2
GLONASS	High	140	3360	96.30	97.14	3
GLONASS	High	140	3360	96.21	96.27	4
GLONASS	High	140	3360	95.34	95.90	5
GLONASS	High	140	3360	93.04	96.71	6

Table 5.15. PTRF-CAN station results for dual-frequency Galileo observations for the day 27.02.2023

Constellation	**Elevation Angle Boundaries**	**Rep. Number**	**Inserted CS**	**Small CS (1-10)%**	**Large CS (10-100)%**	**Method**
Galileo	All	210	9450	76.28	92.62	1
Galileo	All	210	9450	76.31	98.15	2
Galileo	All	210	9450	96.40	98.39	3
Galileo	All	210	9450	82.36	95.28	4
Galileo	All	210	9450	74.52	94.26	5
Galileo	All	210	9450	94.09	97.90	6
Galileo	Low	210	9450	75.32	90.98	1
Galileo	Low	210	9450	76.46	97.72	2
Galileo	Low	210	9450	95.48	98.02	3
Galileo	Low	210	9450	74.29	93.91	4
Galileo	Low	210	9450	63.15	92.28	5
Galileo	Low	210	9450	93.89	97.41	6
Galileo	Mid	210	6440	80.54	96.70	1
Galileo	Mid	210	6440	78.44	99.29	2
Galileo	Mid	210	6440	98.37	99.30	3
Galileo	Mid	210	6440	90.86	99.30	4
Galileo	Mid	210	6440	84.11	97.59	5
Galileo	Mid	210	6440	95.84	98.97	6
Galileo	High	210	3360	80.70	96.54	1
Galileo	High	210	3360	78.22	99.87	2
Galileo	High	210	3360	98.79	99.90	3
Galileo	High	210	3360	99.94	99.87	4
Galileo	High	210	3360	99.49	99.81	5
Galileo	High	210	3360	96	99.27	6

Table 5.16. PTRF-CAN station results for dual-frequency BeiDou observations for the day 27.02.2023

Constellation	Elevation Angle Boundaries	Rep. Number	Inserted CS	Small CS (1-10)%	Large CS (10-100)%	Method
BeiDou	All	140	9520	75.17	91.56	1
BeiDou	All	140	9520	74.20	97.37	2
BeiDou	All	140	9520	94.04	97.53	3
BeiDou	All	140	9520	77.17	93.96	4
BeiDou	All	140	9520	66.36	92.30	5
BeiDou	All	140	9520	93.76	97.10	6
BeiDou	Low	140	8960	73.28	89.89	1
BeiDou	Low	140	8960	73.03	97.46	2
BeiDou	Low	140	8960	93.49	97.55	3
BeiDou	Low	140	8960	71.18	93.42	4
BeiDou	Low	140	8960	56.72	90.91	5
BeiDou	Low	140	8960	94.07	97.29	6
BeiDou	Mid	140	5040	77.86	95.84	1
BeiDou	Mid	140	5040	78.35	99.16	2
BeiDou	Mid	140	5040	97.31	99.02	3
BeiDou	Mid	140	5040	87.39	96.98	4
BeiDou	Mid	140	5040	79.20	95.90	5
BeiDou	Mid	140	5040	95.31	98.76	6
BeiDou	High	140	2800	78.72	96.65	1
BeiDou	High	140	2800	81.02	100	2
BeiDou	High	140	2800	98.91	100	3
BeiDou	High	140	2800	98.80	100	4
BeiDou	High	140	2800	97.41	99.85	5
BeiDou	High	140	2800	95.71	99.59	6

Table 5.17. FFMJ-DEU station results for dual-frequency GPS observations for the day 27.02.2023

Constellation	**Elevation Angle Boundaries**	**Rep. Number**	**Inserted CS**	**Small CS (1-10)%**	**Large CS (10-100)%**	**Method**
GPS	All	110	9790	74.51	92.04	1
GPS	All	110	9790	73.39	97.43	2
GPS	All	110	9790	92.70	97.32	3
GPS	All	110	9790	88.01	95.53	4
GPS	All	110	9790	81.64	94.39	5
GPS	All	110	9790	94.85	98.03	6
GPS	Low	110	7150	78.78	97.05	1
GPS	Low	110	7150	73.66	99.20	2
GPS	Low	110	7150	94.23	99.16	3
GPS	Low	110	7150	90.01	98.79	4
GPS	Low	110	7150	83.32	98.10	5
GPS	Low	110	7150	96.15	99.35	6
GPS	Mid	110	5720	77.56	95.56	1
GPS	Mid	110	5720	77.34	98.31	2
GPS	Mid	110	5720	96.92	98.32	3
GPS	Mid	110	5720	97.79	98.23	4
GPS	Mid	110	5720	96.19	98.06	5
GPS	Mid	110	5720	95.90	98.02	6
GPS	High	110	3520	78.15	96.74	1
GPS	High	110	3520	79.88	99.82	2
GPS	High	110	3520	98.83	99.85	3
GPS	High	110	3520	99.65	99.88	4
GPS	High	110	3520	99.65	99.88	5
GPS	High	110	3520	96.60	99.50	6

Table 5.18. FFMJ-DEU station results for dual-frequency GLONASS observations for the day 27.02.2023

Constellation	**Elevation Angle Boundaries**	**Rep. Number**	**Inserted CS**	**Small CS (1-10)%**	**Large CS (10-100)%**	**Method**
GLONASS	All	130	9100	75.67	93.19	1
GLONASS	All	130	9100	69.44	92.46	2
GLONASS	All	130	9100	92.88	95.16	3
GLONASS	All	130	9100	87.48	92.53	4
GLONASS	All	130	9100	80.58	90.65	5
GLONASS	All	130	9100	93.66	96.22	6
GLONASS	Low	130	8190	75.87	94.42	1
GLONASS	Low	130	8190	71.34	95.66	2
GLONASS	Low	130	8190	92.98	96.39	3
GLONASS	Low	130	8190	86.03	95.41	4
GLONASS	Low	130	8190	78.26	94.22	5
GLONASS	Low	130	8190	94.53	96.73	6
GLONASS	Mid	130	5720	78.62	95.35	1
GLONASS	Mid	130	5720	73.02	94.01	2
GLONASS	Mid	130	5720	94.44	95.40	3
GLONASS	Mid	130	5720	93.08	94.83	4
GLONASS	Mid	130	5720	89.09	93.08	5
GLONASS	Mid	130	5720	93.42	95.81	6
GLONASS	High	130	3250	77.95	97.08	1
GLONASS	High	130	3250	79.29	100	2
GLONASS	High	130	3250	99.26	100	3
GLONASS	High	130	3250	99.29	99.87	4
GLONASS	High	130	3250	98.27	99.67	5
GLONASS	High	130	3250	96.47	99.78	6

Table 5.19. FFMJ-DEU station results for dual-frequency Galileo observations for the day 27.02.2023

Constellation	**Elevation Angle Boundaries**	**Rep. Number**	**Inserted CS**	**Small CS (1-10)%**	**Large CS (10-100)%**	**Method**
Galileo	All	180	9000	77.36	93.29	1
Galileo	All	180	9000	72.22	98.15	2
Galileo	All	180	9000	94.91	98.78	3
Galileo	All	180	9000	90.33	96.53	4
Galileo	All	180	9000	85.23	95.66	5
Galileo	All	180	9000	95.58	98.65	6
Galileo	Low	180	6120	80.51	97.07	1
Galileo	Low	180	6120	75.34	99.36	2
Galileo	Low	180	6120	96.38	99.44	3
Galileo	Low	180	6120	92.61	99.02	4
Galileo	Low	180	6120	86.23	98.13	5
Galileo	Low	180	6120	97.15	99.46	6
Galileo	Mid	180	5040	80.64	98.00	1
Galileo	Mid	180	5040	77.26	100	2
Galileo	Mid	180	5040	98.74	100	3
Galileo	Mid	180	5040	99.54	100	4
Galileo	Mid	180	5040	98.50	99.96	5
Galileo	Mid	180	5040	96.81	99.95	6
Galileo	High	180	3600	79.50	96.90	1
Galileo	High	180	3600	77.54	99.65	2
Galileo	High	180	3600	98.13	99.59	3
Galileo	High	180	3600	99.06	99.44	4
Galileo	High	180	3600	99.01	99.44	5
Galileo	High	180	3600	96.17	99.36	6

Table 5.20. FFMJ-DEU station results for dual-frequency BeiDou observations for the day 27.02.2023

Constellation	Elevation Angle Boundaries	Rep. Number	Inserted CS	Small CS (1-10)%	Large CS (10-100)%	Method
BeiDou	All	80	9520	78.84	91.76	1
BeiDou	All	80	9520	72.48	97	2
BeiDou	All	80	9520	92.44	97.52	3
BeiDou	All	80	9520	85	95.16	4
BeiDou	All	80	9520	75.42	93.15	5
BeiDou	All	80	9520	94.29	97.69	6
BeiDou	Low	80	6320	78.48	95.26	1
BeiDou	Low	80	6320	74.84	98.49	2
BeiDou	Low	80	6320	94.86	98.54	3
BeiDou	Low	80	6320	85.46	96.67	4
BeiDou	Low	80	6320	74.63	95.19	5
BeiDou	Low	80	6320	95.52	98.56	6
BeiDou	Mid	80	4240	79.95	96.61	1
BeiDou	Mid	80	4240	78.53	99.71	2
BeiDou	Mid	80	4240	98.53	99.62	3
BeiDou	Mid	80	4240	95.48	98.85	4
BeiDou	Mid	80	4240	89.30	98.32	5
BeiDou	Mid	80	4240	97.12	99.52	6
BeiDou	High	80	2000	79.01	98.23	1
BeiDou	High	80	2000	80.52	100	2
BeiDou	High	80	2000	99.11	100	3
BeiDou	High	80	2000	100	100	4
BeiDou	High	80	2000	99.53	100	5
BeiDou	High	80	2000	97.66	100	6

Table 5.21. MIZU-JPN station results for dual-frequency GPS observations for the day 27.02.2023

Constellation	**Elevation Angle Boundaries**	**Rep. Number**	**Inserted CS**	**Small CS (1-10)%**	**Large CS (10-100)%**	**Method**
GPS	All	120	7920	76.02	97.68	1
GPS	All	120	7920	74.4	98.48	2
GPS	All	120	7920	96.87	99.18	3
GPS	All	120	7920	91.99	97.73	4
GPS	All	120	7920	86.97	97.12	5
GPS	All	120	7920	96.76	99.26	6
GPS	Low	120	7080	77.52	96.38	1
GPS	Low	120	7080	72.9	99.25	2
GPS	Low	120	7080	96.74	99.5	3
GPS	Low	120	7080	87.28	97.87	4
GPS	Low	120	7080	79.02	96.75	5
GPS	Low	120	7080	97.22	99.57	6
GPS	Mid	120	5760	78.22	96.38	1
GPS	Mid	120	5760	76.77	99.36	2
GPS	Mid	120	5760	98.17	99.49	3
GPS	Mid	120	5760	97.41	99.02	4
GPS	Mid	120	5760	95.71	98.78	5
GPS	Mid	120	5760	96.77	99.29	6
GPS	High	120	3960	78.67	96.74	1
GPS	High	120	3960	79.17	100	2
GPS	High	120	3960	99.14	100	3
GPS	High	120	3960	99.74	100	4
GPS	High	120	3960	99.75	100	5
GPS	High	120	3960	97.42	99.8	6

Table 5.22. MIZU-JPN station results for dual-frequency GLONASS observations for the day 27.02.2023

Constellation	Elevation Angle Boundaries	Rep. Number	Inserted CS	Small CS (1-10)%	Large CS (10-100)%	Method
GLONASS	All	120	7680	74.76	93.29	1
GLONASS	All	120	7680	67.67	90.37	2
GLONASS	All	120	7680	91.96	94.40	3
GLONASS	All	120	7680	82.16	89.80	4
GLONASS	All	120	7680	75.16	88.25	5
GLONASS	All	120	7680	94.27	96.53	6
GLONASS	Low	120	6240	76.47	95.70	1
GLONASS	Low	120	6240	70.33	95.42	2
GLONASS	Low	120	6240	93.38	97.09	3
GLONASS	Low	120	6240	79.49	93.81	4
GLONASS	Low	120	6240	69.69	92.19	5
GLONASS	Low	120	6240	93.89	96.63	6
GLONASS	Mid	120	4320	75.79	95.74	1
GLONASS	Mid	120	4320	74.45	96.43	2
GLONASS	Mid	120	4320	96.86	98.74	3
GLONASS	Mid	120	4320	91.62	95.64	4
GLONASS	Mid	120	4320	87.14	94.76	5
GLONASS	Mid	120	4320	94.79	98.14	6
GLONASS	High	120	3240	78.08	97.76	1
GLONASS	High	120	3240	76.41	96.70	2
GLONASS	High	120	3240	98.43	99.10	3
GLONASS	High	120	3240	97.21	97.21	4
GLONASS	High	120	3240	96.76	96.83	5
GLONASS	High	120	3240	95.90	98.24	6

Table 5.23. MIZU-JPN station results for dual-frequency Galileo observations for the day 27.02.2023

Constellation	**Elevation Angle Boundaries**	**Rep. Number**	**Inserted CS**	**Small CS (1-10)%**	**Large CS (10-100)%**	**Method**
Galileo	All	210	7560	78.91	94.63	1
Galileo	All	210	7560	72.78	95.70	2
Galileo	All	210	7560	94.79	97.29	3
Galileo	All	210	7560	91.93	95.36	4
Galileo	All	210	7560	88.20	94.68	5
Galileo	All	210	7560	92.99	96.52	6
Galileo	Low	210	6510	78.60	93.46	1
Galileo	Low	210	6510	73.05	97.54	2
Galileo	Low	210	6510	95.25	97.67	3
Galileo	Low	210	6510	88.54	95.33	4
Galileo	Low	210	6510	82.84	94.60	5
Galileo	Low	210	6510	94.29	97.60	6
Galileo	Mid	210	5460	81.83	97.64	1
Galileo	Mid	210	5460	74.44	95.89	2
Galileo	Mid	210	5460	96	97.28	3
Galileo	Mid	210	5460	95.66	96.34	4
Galileo	Mid	210	5460	94.91	95.94	5
Galileo	Mid	210	5460	92.78	96.30	6
Galileo	High	210	3570	79.35	96.93	1
Galileo	High	210	3570	78.07	99.49	2
Galileo	High	210	3570	98.33	99.58	3
Galileo	High	210	3570	99.58	99.55	4
Galileo	High	210	3570	97.70	99.56	5
Galileo	High	210	3570	95.51	99.29	6

Table 5.24. MIZU-JPN station results for dual-frequency BeiDou observations for the day 27.02.2023

Constellation	**Elevation Angle Boundaries**	**Rep. Number**	**Inserted CS**	**Small CS (1-10)%**	**Large CS (10-100)%**	**Method**
BeiDou	All	100	8500	78.52	94.80	1
BeiDou	All	100	8500	76.93	98.25	2
BeiDou	All	100	8500	96.24	98.26	3
BeiDou	All	100	8500	92.63	97.27	4
BeiDou	All	100	8500	86.98	96.43	5
BeiDou	All	100	8500	95.87	98.44	6
BeiDou	Low	100	7700	78.99	96.96	1
BeiDou	Low	100	7700	74.59	99	2
BeiDou	Low	100	7700	94.25	98.96	3
BeiDou	Low	100	7700	87.38	97.79	4
BeiDou	Low	100	7700	76.71	96.58	5
BeiDou	Low	100	7700	95.58	98.97	6
BeiDou	Mid	100	5800	79.51	96.35	1
BeiDou	Mid	100	5800	78.70	99.51	2
BeiDou	Mid	100	5800	98.12	99.40	3
BeiDou	Mid	100	5800	96.58	99.23	4
BeiDou	Mid	100	5800	93.04	98.75	5
BeiDou	Mid	100	5800	96.44	99.19	6
BeiDou	High	100	3700	80.92	98.11	1
BeiDou	High	100	3700	80.11	100	2
BeiDou	High	100	3700	99.17	100	3
BeiDou	High	100	3700	100	100	4
BeiDou	High	100	3700	100	100	5
BeiDou	High	100	3700	97.28	100	6

Table 5.25. LPGS-ARG station results for dual-frequency GPS observations for the day 27.02.2023

Constellation	**Elevation Angle Boundaries**	**Rep. Number**	**Inserted CS**	**Small CS (1-10)%**	**Large CS (10-100)%**	**Method**
GPS	All	110	8470	72.42	90.26	1
GPS	All	110	8470	74.46	97.09	2
GPS	All	110	8470	96.29	97.93	3
GPS	All	110	8470	84.81	94.53	4
GPS	All	110	8470	77.47	93.24	5
GPS	All	110	8470	93.73	97.15	6
GPS	Low	110	8250	68.83	84.46	1
GPS	Low	110	8250	72.14	95.5	2
GPS	Low	110	8250	94.25	96.72	3
GPS	Low	110	8250	74.15	90.61	4
GPS	Low	110	8250	63.1	88.58	5
GPS	Low	110	8250	92.04	95.49	6
GPS	Mid	110	5390	75.89	94.31	1
GPS	Mid	110	5390	76.31	97.28	2
GPS	Mid	110	5390	96.1	97.32	3
GPS	Mid	110	5390	89.34	96.1	4
GPS	Mid	110	5390	83.3	95.27	5
GPS	Mid	110	5390	93.56	97.01	6
GPS	High	110	3190	79.32	98.02	1
GPS	High	110	3190	78.99	100	2
GPS	High	110	3190	99.64	100	3
GPS	High	110	3190	100	100	4
GPS	High	110	3190	100	100	5
GPS	High	110	3190	97.05	100	6

Table 5.26. LPGS-ARG station results for dual-frequency GLONASS observations for the day 27.02.2023

Constellation	**Elevation Angle Boundaries**	**Rep. Number**	**Inserted CS**	**Small CS (1-10)%**	**Large CS (10-100)%**	**Method**
GLONASS	All	160	8640	73.84	91.73	1
GLONASS	All	160	8640	66.84	87.09	2
GLONASS	All	160	8640	91.40	93.04	3
GLONASS	All	160	8640	73.71	85.29	4
GLONASS	All	160	8640	66.20	83.61	5
GLONASS	All	160	8640	88.42	91.50	6
GLONASS	Low	160	8160	71.78	88	1
GLONASS	Low	160	8160	65.06	87.03	2
GLONASS	Low	160	8160	91.51	93.76	3
GLONASS	Low	160	8160	61.18	82.06	4
GLONASS	Low	160	8160	49.38	79.51	5
GLONASS	Low	160	8160	87.33	90.01	6
GLONASS	Mid	160	5440	77.97	96.67	1
GLONASS	Mid	160	5440	76.21	96.70	2
GLONASS	Mid	160	5440	97.44	98.69	3
GLONASS	Mid	160	5440	84.39	95.15	4
GLONASS	Mid	160	5440	76.19	93.81	5
GLONASS	Mid	160	5440	93.30	96.65	6
GLONASS	High	160	4000	78.33	97.06	1
GLONASS	High	160	4000	74.84	95.89	2
GLONASS	High	160	4000	95.65	96.69	3
GLONASS	High	160	4000	95.55	96.09	4
GLONASS	High	160	4000	93.41	95.65	5
GLONASS	High	160	4000	91.59	95.52	6

Table 5.27. LPGS-ARG station results for dual-frequency Galileo observations for the day 27.02.2023

Constellation	**Elevation Angle Boundaries**	**Rep. Number**	**Inserted CS**	**Small CS (1-10)%**	**Large CS (10-100)%**	**Method**
Galileo	All	160	8960	73.72	88.85	1
Galileo	All	160	8960	73.19	96.85	2
Galileo	All	160	8960	96.11	98.06	3
Galileo	All	160	8960	77.67	92.06	4
Galileo	All	160	8960	68.97	91.01	5
Galileo	All	160	8960	92.61	96.70	6
Galileo	Low	160	8800	71.19	86.19	1
Galileo	Low	160	8800	72.85	95.88	2
Galileo	Low	160	8800	95.72	97.28	3
Galileo	Low	160	8800	69.36	89.72	4
Galileo	Low	160	8800	68.13	88.12	5
Galileo	Low	160	8800	92.50	95.78	6
Galileo	Mid	160	4480	79.40	96.83	1
Galileo	Mid	160	4480	80.39	100	2
Galileo	Mid	160	4480	98.70	100	3
Galileo	Mid	160	4480	91.04	98.80	4
Galileo	Mid	160	4480	84.84	98.19	5
Galileo	Mid	160	4480	95.32	99.56	6
Galileo	High	160	2720	81.45	97.54	1
Galileo	High	160	2720	78.56	100	2
Galileo	High	160	2720	99.26	100	3
Galileo	High	160	2720	100	100	4
Galileo	High	160	2720	100	100	5
Galileo	High	160	2720	95.63	100	6

Table 5.28. LPGS-ARG station results for dual-frequency BeiDou observations for the day 27.02.2023

Constellation	**Elevation Angle Boundaries**	**Rep. Number**	**Inserted CS**	**Small CS (1-10)%**	**Large CS (10-100)%**	**Method**
BeiDou	All	140	8820	74.69	90.62	1
BeiDou	All	140	8820	74.11	96.98	2
BeiDou	All	140	8820	95.65	97.74	3
BeiDou	All	140	8820	76.12	93.06	4
BeiDou	All	140	8820	65.70	91.44	5
BeiDou	All	140	8820	93.24	96.71	6
BeiDou	Low	140	8820	69.98	85.94	1
BeiDou	Low	140	8820	71.01	95.14	2
BeiDou	Low	140	8820	93.08	95.86	3
BeiDou	Low	140	8820	63.36	89.25	4
BeiDou	Low	140	8820	55.84	86.19	5
BeiDou	Low	140	8820	91.43	94.98	6
BeiDou	Mid	140	5600	79.74	96.67	1
BeiDou	Mid	140	5600	74.73	95.93	2
BeiDou	Mid	140	5600	97.78	99.47	3
BeiDou	Mid	140	5600	82.05	93	4
BeiDou	Mid	140	5600	72.91	91.90	5
BeiDou	Mid	140	5600	91.96	95.60	6
BeiDou	High	140	3500	79.49	97.86	1
BeiDou	High	140	3500	80.42	100	2
BeiDou	High	140	3500	99.29	100	3
BeiDou	High	140	3500	99.23	100	4
BeiDou	High	140	3500	96.46	99.88	5
BeiDou	High	140	3500	95.80	99.97	6

Table 5.29. PTRF-CAN station results for dual-frequency GPS observations for the day 25.05.2023

Constellation	**Elevation Angle Boundaries**	**Rep. Number**	**Inserted CS**	**Small CS (1-10)%**	**Large CS (10-100)%**	**Method**
GPS	All	110	9350	73.85	91.35	1
GPS	All	110	9350	73.92	97.39	2
GPS	All	110	9350	93.59	97.09	3
GPS	All	110	9350	81.13	94.32	4
GPS	All	110	9350	72.29	92.77	5
GPS	All	110	9350	93.38	97.15	6
GPS	Low	110	9130	72.68	90.15	1
GPS	Low	110	9130	72.76	97.14	2
GPS	Low	110	9130	92.05	96.78	3
GPS	Low	110	9130	72.75	92.86	4
GPS	Low	110	9130	60.67	91.12	5
GPS	Low	110	9130	92.9	96.96	6
GPS	Mid	110	5940	78.27	96.52	1
GPS	Mid	110	5940	77.6	99.43	2
GPS	Mid	110	5940	97.41	99.45	3
GPS	Mid	110	5940	89.28	98.3	4
GPS	Mid	110	5940	82.81	97.53	5
GPS	Mid	110	5940	95.49	99.03	6
GPS	High	110	3410	79.18	97.42	1
GPS	High	110	3410	80.09	100	2
GPS	High	110	3410	99	100	3
GPS	High	110	3410	100	100	4
GPS	High	110	3410	99.88	100	5
GPS	High	110	3410	96.15	99.81	6

Table 5.30. PTRF-CAN station results for dual-frequency GLONASS observations for the day 25.05.2023

Constellation	**Elevation Angle Boundaries**	**Rep. Number**	**Inserted CS**	**Small CS (1-10)%**	**Large CS (10-100)%**	**Method**
GLONASS	All	130	9100	74.33	91.64	1
GLONASS	All	130	9100	71.24	94.88	2
GLONASS	All	130	9100	90.88	94.64	3
GLONASS	All	130	9100	74.57	91.98	4
GLONASS	All	130	9100	64.86	89.92	5
GLONASS	All	130	9100	93.19	97.10	6
GLONASS	Low	130	8840	71.26	88.56	1
GLONASS	Low	130	8840	71.46	96.61	2
GLONASS	Low	130	8840	91.81	96.30	3
GLONASS	Low	130	8840	67.21	92.09	4
GLONASS	Low	130	8840	54.58	89.58	5
GLONASS	Low	130	8840	92.70	96.40	6
GLONASS	Mid	130	4550	78.44	97	1
GLONASS	Mid	130	4550	79	100	2
GLONASS	Mid	130	4550	97.71	99.93	3
GLONASS	Mid	130	4550	90.42	98.82	4
GLONASS	Mid	130	4550	82.87	98.05	5
GLONASS	Mid	130	4550	95.79	99.77	6
GLONASS	High	130	2990	78.71	97.41	1
GLONASS	High	130	2990	80.17	100	2
GLONASS	High	130	2990	98.88	100	3
GLONASS	High	130	2990	100	100	4
GLONASS	High	130	2990	99.13	100	5
GLONASS	High	130	2990	95.98	99.74	6

Table 5.31. PTRF-CAN station results for dual-frequency Galileo observations for the day 25.05.2023

Constellation	Elevation Angle Boundaries	Rep. Number	Inserted CS	Small CS (1-10)%	Large CS (10-100)%	Method
Galileo	All	200	8600	78.21	95.05	1
Galileo	All	200	8600	75.35	98.96	2
Galileo	All	200	8600	94.67	98.62	3
Galileo	All	200	8600	84.49	96.74	4
Galileo	All	200	8600	76.80	95.56	5
Galileo	All	200	8600	93.71	98.57	6
Galileo	Low	200	8400	77.28	93.54	1
Galileo	Low	200	8400	74.12	98.49	2
Galileo	Low	200	8400	93.71	98.17	3
Galileo	Low	200	8400	74.40	94.55	4
Galileo	Low	200	8400	63.57	93.15	5
Galileo	Low	200	8400	93.95	98.07	6
Galileo	Mid	200	6000	80.99	96.84	1
Galileo	Mid	200	6000	79.60	99.50	2
Galileo	Mid	200	6000	97.78	99.38	3
Galileo	Mid	200	6000	92.29	98.60	4
Galileo	Mid	200	6000	85.86	98.09	5
Galileo	Mid	200	6000	95.37	99.07	6
Galileo	High	200	3400	80.84	97.25	1
Galileo	High	200	3400	77.91	100	2
Galileo	High	200	3400	97.41	100	3
Galileo	High	200	3400	100	100	4
Galileo	High	200	3400	100	100	5
Galileo	High	200	3400	95.47	99.56	6

Table 5.32. PTRF-CAN station results for dual-frequency BeiDou observations for the day 25.05.2023

Constellation	**Elevation Angle Boundaries**	**Rep. Number**	**Inserted CS**	**Small CS (1-10)%**	**Large CS (10-100)%**	**Method**
BeiDou	All	130	8970	75.71	92.64	1
BeiDou	All	130	8970	72.61	96.89	2
BeiDou	All	130	8970	90.34	94.40	3
BeiDou	All	130	8970	76.23	93.31	4
BeiDou	All	130	8970	76.13	91.53	5
BeiDou	All	130	8970	93.11	97.13	6
BeiDou	Low	130	8450	73.79	92.75	1
BeiDou	Low	130	8450	72.91	97.79	2
BeiDou	Low	130	8450	91.43	97.32	3
BeiDou	Low	130	8450	69.90	93.09	4
BeiDou	Low	130	8450	64.95	91.11	5
BeiDou	Low	130	8450	92.84	97.46	6
BeiDou	Mid	130	4420	79.73	94.75	1
BeiDou	Mid	130	4420	79.02	98.60	2
BeiDou	Mid	130	4420	96.81	99.48	3
BeiDou	Mid	130	4420	92.25	96.60	4
BeiDou	Mid	130	4420	84.51	98.52	5
BeiDou	Mid	130	4420	94.83	98.21	6
BeiDou	High	130	2470	81.74	97.22	1
BeiDou	High	130	2470	80.29	100	2
BeiDou	High	130	2470	98.85	100	3
BeiDou	High	130	2470	100	100	4
BeiDou	High	130	2470	99.97	100	5
BeiDou	High	130	2470	95.68	100	6

Table 5.33. FFMJ-DEU station results for dual-frequency GPS observations for the day 25.05.2023

Constellation	**Elevation Angle Boundaries**	**Rep. Number**	**Inserted CS**	**Small CS (1-10)%**	**Large CS (10-100)%**	**Method**
GPS	All	110	9790	74.51	92.04	1
GPS	All	110	9790	73.39	97.43	2
GPS	All	110	9790	92.70	97.32	3
GPS	All	110	9790	88.01	95.53	4
GPS	All	110	9790	81.64	94.39	5
GPS	All	110	9790	94.85	98.03	6
GPS	Low	110	7150	78.78	97.05	1
GPS	Low	110	7150	73.66	99.20	2
GPS	Low	110	7150	94.23	99.16	3
GPS	Low	110	7150	90.01	98.79	4
GPS	Low	110	7150	83.32	98.10	5
GPS	Low	110	7150	96.15	99.35	6
GPS	Mid	110	5720	77.56	95.56	1
GPS	Mid	110	5720	77.34	98.31	2
GPS	Mid	110	5720	96.92	98.32	3
GPS	Mid	110	5720	97.79	98.23	4
GPS	Mid	110	5720	96.19	98.06	5
GPS	Mid	110	5720	95.90	98.02	6
GPS	High	110	3520	78.15	96.74	1
GPS	High	110	3520	79.88	99.82	2
GPS	High	110	3520	98.83	99.85	3
GPS	High	110	3520	99.65	99.88	4
GPS	High	110	3520	99.65	99.88	5
GPS	High	110	3520	96.60	99.50	6

Table 5.34. FFMJ-DEU station results for dual-frequency GLONASS observations for the day 25.05.2023

Constellation	**Elevation Angle Boundaries**	**Rep. Number**	**Inserted CS**	**Small CS (1-10)%**	**Large CS (10-100)%**	**Method**
GLONASS	All	130	8970	74.71	93.60	1
GLONASS	All	130	8970	71.20	94.34	2
GLONASS	All	130	8970	91.56	95.31	3
GLONASS	All	130	8970	87.41	94.20	4
GLONASS	All	130	8970	81.97	93.01	5
GLONASS	All	130	8970	94.84	98.42	6
GLONASS	Low	130	7670	74.72	93.55	1
GLONASS	Low	130	7670	73.17	97.80	2
GLONASS	Low	130	7670	92.53	97.85	3
GLONASS	Low	130	7670	87.72	96.55	4
GLONASS	Low	130	7670	80.28	95.53	5
GLONASS	Low	130	7670	94.83	98.34	6
GLONASS	Mid	130	5590	77.05	95.92	1
GLONASS	Mid	130	5590	78.44	99.12	2
GLONASS	Mid	130	5590	97.53	99.19	3
GLONASS	Mid	130	5590	97.07	98.55	4
GLONASS	Mid	130	5590	94.27	98.26	5
GLONASS	Mid	130	5590	96.23	99.21	6
GLONASS	High	130	3120	78.26	97.59	1
GLONASS	High	130	3120	78.63	100	2
GLONASS	High	130	3120	99	100	3
GLONASS	High	130	3120	99.97	100	4
GLONASS	High	130	3120	99.53	100	5
GLONASS	High	130	3120	96.52	100	6

Table 5.35. FFMJ-DEU station results for dual-frequency Galileo observations for the day 25.05.2023

Constellation	**Elevation Angle Boundaries**	**Rep. Number**	**Inserted CS**	**Small CS (1-10)%**	**Large CS (10-100)%**	**Method**
Galileo	All	180	9180	72.79	94.24	1
Galileo	All	180	9180	72.37	98.12	2
Galileo	All	180	9180	92.92	98.03	3
Galileo	All	180	9180	91.64	97.13	4
Galileo	All	180	9180	86.44	96.13	5
Galileo	All	180	9180	94.97	98.52	6
Galileo	Low	180	7380	79.85	96.15	1
Galileo	Low	180	7380	73.47	98.82	2
Galileo	Low	180	7380	94.51	98.88	3
Galileo	Low	180	7380	94.50	98.61	4
Galileo	Low	180	7380	89.03	97.99	5
Galileo	Low	180	7380	95.33	99.04	6
Galileo	Mid	180	5400	81.03	97.51	1
Galileo	Mid	180	5400	77.01	99.71	2
Galileo	Mid	180	5400	98.12	99.72	3
Galileo	Mid	180	5400	99.69	99.87	4
Galileo	Mid	180	5400	99.04	99.77	5
Galileo	Mid	180	5400	96.17	99.48	6
Galileo	High	180	3240	80.72	97.22	1
Galileo	High	180	3240	76.76	100	2
Galileo	High	180	3240	97.65	100	3
Galileo	High	180	3240	100	100	4
Galileo	High	180	3240	100	100	5
Galileo	High	180	3240	95.78	99.87	6

Table 5.36. FFMJ-DEU station results for dual-frequency BeiDou observations for the day 25.05.2023

Constellation	Elevation Angle Boundaries	Rep. Number	Inserted CS	Small CS (1-10)%	Large CS (10-100)%	Method
BeiDou	All	80	9120	75.50	91.04	1
BeiDou	All	80	9120	70.95	96.19	2
BeiDou	All	80	9120	88.31	94.86	3
BeiDou	All	80	9120	85.79	94.40	4
BeiDou	All	80	9120	77.88	93.13	5
BeiDou	All	80	9120	93.42	97.19	6
BeiDou	Low	80	5440	79.51	97.44	1
BeiDou	Low	80	5440	75.07	99.65	2
BeiDou	Low	80	5440	93.82	99.16	3
BeiDou	Low	80	5440	89.29	98.60	4
BeiDou	Low	80	5440	80.88	97.59	5
BeiDou	Low	80	5440	95.26	99.38	6
BeiDou	Mid	80	4160	79.09	97.28	1
BeiDou	Mid	80	4160	78.92	100	2
BeiDou	Mid	80	4160	97.55	99.98	3
BeiDou	Mid	80	4160	96.62	99.75	4
BeiDou	Mid	80	4160	92.08	99.22	5
BeiDou	Mid	80	4160	95.47	99.68	6
BeiDou	High	80	2000	80.16	97.66	1
BeiDou	High	80	2000	81.41	100	2
BeiDou	High	80	2000	99.11	100	3
BeiDou	High	80	2000	100	100	4
BeiDou	High	80	2000	100	100	5
BeiDou	High	80	2000	96.30	100	6

Table 5.37. MIZU-JPN station results for dual-frequency GPS observations for the day 25.05.2023

Constellation	**Elevation Angle Boundaries**	**Rep. Number**	**Inserted CS**	**Small CS (1-10)%**	**Large CS (10-100)%**	**Method**
GPS	All	110	7480	76.17	93.69	1
GPS	All	110	7480	73.98	97.87	2
GPS	All	110	7480	95.47	98.36	3
GPS	All	110	7480	93.77	97.58	4
GPS	All	110	7480	89.27	96.69	5
GPS	All	110	7480	95.79	98.49	6
GPS	Low	110	6930	76.57	94.69	1
GPS	Low	110	6930	73.08	98.42	2
GPS	Low	110	6930	94.68	98.81	3
GPS	Low	110	6930	91.41	98.09	4
GPS	Low	110	6930	84.78	97.16	5
GPS	Low	110	6930	96.09	98.82	6
GPS	Mid	110	4950	79.11	97.29	1
GPS	Mid	110	4950	78.38	99.9	2
GPS	Mid	110	4950	98.49	99.93	3
GPS	Mid	110	4950	99	99.94	4
GPS	Mid	110	4950	97.21	99.65	5
GPS	Mid	110	4950	96.88	99.67	6
GPS	High	120	3840	79.27	99	1
GPS	High	120	3840	77.85	100	2
GPS	High	120	3840	99.22	100	3
GPS	High	120	3840	100	100	4
GPS	High	120	3840	100	100	5
GPS	High	120	3840	97.23	100	6

Table 5.38. MIZU-JPN station results for dual-frequency GLONASS observations for the day 25.05.2023

Constellation	**Elevation Angle Boundaries**	**Rep. Number**	**Inserted CS**	**Small CS (1-10)%**	**Large CS (10-100)%**	**Method**
GLONASS	All	160	8960	75.94	94.22	1
GLONASS	All	160	8960	63.36	87.47	2
GLONASS	All	160	8960	79.42	95.45	3
GLONASS	All	160	8960	86.07	92.95	4
GLONASS	All	160	8960	80.45	91.80	5
GLONASS	All	160	8960	95.61	98.64	6
GLONASS	Low	160	5760	76.16	95.66	1
GLONASS	Low	160	5760	73.77	98.16	2
GLONASS	Low	160	5760	92.62	96.84	3
GLONASS	Low	160	5760	95.09	98.73	4
GLONASS	Low	160	5760	91.39	97.98	5
GLONASS	Low	160	5760	95.98	99.10	6
GLONASS	Mid	160	4320	72.96	90.81	1
GLONASS	Mid	160	4320	76.03	96.92	2
GLONASS	Mid	160	4320	95.75	97.02	3
GLONASS	Mid	160	4320	91.27	94.52	4
GLONASS	Mid	160	4320	87.31	93.75	5
GLONASS	Mid	160	4320	95.55	98.13	6
GLONASS	High	160	3520	77.17	94.94	1
GLONASS	High	160	3520	78.99	99.94	2
GLONASS	High	160	3520	98.84	99.67	3
GLONASS	High	160	3520	89.82	98.63	4
GLONASS	High	160	3520	84.17	97.77	5
GLONASS	High	160	3520	96.82	99.79	6

Table 5.39. MIZU-JPN station results for dual-frequency Galileo observations for the day 25.05.2023

Constellation	**Elevation Angle Boundaries**	**Rep. Number**	**Inserted CS**	**Small CS (1-10)%**	**Large CS (10-100)%**	**Method**
Galileo	All	200	7200	80.36	96.03	1
Galileo	All	200	7200	77.61	94.76	2
Galileo	All	200	7200	95.31	95.54	3
Galileo	All	200	7200	93.53	96.18	4
Galileo	All	200	7200	90.70	95.50	5
Galileo	All	200	7200	92.81	96.37	6
Galileo	Low	200	4000	80.68	96.18	1
Galileo	Low	200	4000	77.87	98.42	2
Galileo	Low	200	4000	95.84	98.76	3
Galileo	Low	200	4000	97.11	99.08	4
Galileo	Low	200	4000	95.32	98.76	5
Galileo	Low	200	4000	95.21	99.05	6
Galileo	Mid	200	3000	80.68	96.39	1
Galileo	Mid	200	3000	77.75	99.57	2
Galileo	Mid	200	3000	98.75	99.64	3
Galileo	Mid	200	3000	99.14	99.21	4
Galileo	Mid	200	3000	98.43	99.14	5
Galileo	Mid	200	3000	95.68	99.36	6
Galileo	High	200	2800	82.12	96.15	1
Galileo	High	200	2800	77.69	99.69	2
Galileo	High	200	2800	99.50	99.84	3
Galileo	High	200	2800	96.04	99.31	4
Galileo	High	200	2800	92.81	99	5
Galileo	High	200	2800	96.46	99.23	6

Table 5.40. MIZU-JPN station results for dual-frequency BeiDou observations for the day 25.05.2023

Constellation	**Elevation Angle Boundaries**	**Rep. Number**	**Inserted CS**	**Small CS (1-10)%**	**Large CS (10-100)%**	**Method**
BeiDou	All	110	9020	77.61	95.25	1
BeiDou	All	110	9020	75.53	97.44	2
BeiDou	All	110	9020	95.59	97.97	3
BeiDou	All	110	9020	93.91	98.09	4
BeiDou	All	110	9020	88.35	97.27	5
BeiDou	All	110	9020	94.92	98.65	6
BeiDou	Low	110	2750	81.49	97.31	1
BeiDou	Low	110	2750	79.36	100	2
BeiDou	Low	110	2750	94.46	99.32	3
BeiDou	Low	110	2750	98.56	99.89	4
BeiDou	Low	110	2750	97.05	99.58	5
BeiDou	Low	110	2750	96.48	100	6
BeiDou	Mid	110	2200	78.81	97.08	1
BeiDou	Mid	110	2200	80.77	100	2
BeiDou	Mid	110	2200	97.80	99.81	3
BeiDou	Mid	110	2200	98	99.43	4
BeiDou	Mid	110	2200	96.12	99.19	5
BeiDou	Mid	110	2200	95.45	99.67	6
BeiDou	High	110	1760	81.21	98	1
BeiDou	High	110	1760	78.18	100	2
BeiDou	High	110	1760	99.45	100	3
BeiDou	High	110	1760	94.97	100	4
BeiDou	High	110	1760	89.64	100	5
BeiDou	High	110	1760	97.33	100	6

Table 5.41. LPGS-ARG station results for dual-frequency GPS observations for the day 25.05.2023

Constellation	**Elevation Angle Boundaries**	**Rep. Number**	**Inserted CS**	**Small CS (1-10)%**	**Large CS (10-100)%**	**Method**
GPS	All	110	8250	71.76	89.2	1
GPS	All	110	8250	73.28	98.07	2
GPS	All	110	8250	94.25	97.17	3
GPS	All	110	8250	83.33	95.1	4
GPS	All	110	8250	76.9	93.32	5
GPS	All	110	8250	92.79	97.77	6
GPS	Low	110	8030	70.08	84.8	1
GPS	Low	110	8030	73.13	95.14	2
GPS	Low	110	8030	92.05	95.46	3
GPS	Low	110	8030	72.29	89.47	4
GPS	Low	110	8030	62.5	87.93	5
GPS	Low	110	8030	91.35	94.97	6
GPS	Mid	110	5610	78.24	95.53	1
GPS	Mid	110	5610	77.74	99.84	2
GPS	Mid	110	5610	97.58	99.73	3
GPS	Mid	110	5610	92.96	99.05	4
GPS	Mid	110	5610	87.58	98.4	5
GPS	Mid	110	5610	95.69	99.45	6
GPS	High	110	3300	78.06	100	1
GPS	High	110	3300	79.66	100	2
GPS	High	110	3300	98.68	100	3
GPS	High	110	3300	99.84	100	4
GPS	High	110	3300	99.85	100	5
GPS	High	110	3300	95.71	100	6

Table 5.42. LPGS-ARG station results for dual-frequency GLONASS observations for the day 25.05.2023

Constellation	**Elevation Angle Boundaries**	**Rep. Number**	**Inserted CS**	**Small CS (1-10)%**	**Large CS (10-100)%**	**Method**
GLONASS	All	150	7990	74.75	92.11	1
GLONASS	All	150	7990	74.19	95.91	2
GLONASS	All	150	7990	93.27	95.88	3
GLONASS	All	150	7990	80.54	93.08	4
GLONASS	All	150	7990	72.46	91.82	5
GLONASS	All	150	7990	93.62	97.67	6
GLONASS	Low	150	7650	70.98	88.41	1
GLONASS	Low	150	7650	70.86	96.1	2
GLONASS	Low	150	7650	91.02	95.07	3
GLONASS	Low	150	7650	66.3	89.55	4
GLONASS	Low	150	7650	54.75	87.57	5
GLONASS	Low	150	7650	91.28	95.53	6
GLONASS	Mid	150	5610	78.09	97.18	1
GLONASS	Mid	150	5610	77.17	100	2
GLONASS	Mid	150	5610	97.37	99.83	3
GLONASS	Mid	150	5610	87.92	98.58	4
GLONASS	Mid	150	5610	80.94	97.52	5
GLONASS	Mid	150	5610	95.18	99.61	6
GLONASS	High	150	3300	78.49	96.96	1
GLONASS	High	150	3300	79.08	99.9	2
GLONASS	High	150	3300	98.93	99.8	3
GLONASS	High	150	3300	98.51	99.57	4
GLONASS	High	150	3300	96.16	99.18	5
GLONASS	High	150	3300	96.24	99.54	6

Table 5.43. LPGS-ARG station results for dual-frequency Galileo observations for the day 25.05.2023

Constellation	**Elevation Angle Boundaries**	**Rep. Number**	**Inserted CS**	**Small CS (1-10)%**	**Large CS (10-100)%**	**Method**
Galileo	All	140	9380	73.74	88.12	1
Galileo	All	140	9380	72.89	96.61	2
Galileo	All	140	9380	93.72	96.48	3
Galileo	All	140	9380	74.86	91.3	4
Galileo	All	140	9380	65.61	89.77	5
Galileo	All	140	9380	92.33	96.19	6
Galileo	Low	140	7650	70.5	86.27	1
Galileo	Low	140	7650	71.49	95.88	2
Galileo	Low	140	7650	92.12	95.69	3
Galileo	Low	140	7650	67.48	89.87	4
Galileo	Low	140	7650	56.46	88.35	5
Galileo	Low	140	7650	91.36	95.52	6
Galileo	Mid	140	3920	80.5	96.46	1
Galileo	Mid	140	3920	77.46	99.6	2
Galileo	Mid	140	3920	97.99	99.55	3
Galileo	Mid	140	3920	92.59	98.86	4
Galileo	Mid	140	3920	86.98	98.12	5
Galileo	Mid	140	3920	95.61	99.34	6
Galileo	High	140	2520	80.42	96.93	1
Galileo	High	140	2520	78.24	100	2
Galileo	High	140	2520	97.94	100	3
Galileo	High	140	2520	100	100	4
Galileo	High	140	2520	100	100	5
Galileo	High	140	2520	94.96	99.41	6

Table 5.44. LPGS-ARG station results for dual-frequency BeiDou observations for the day 25.05.2023

Constellation	Elevation Angle Boundaries	Rep. Number	Inserted CS	Small CS (1-10)%	Large CS (10-100)%	Method
BeiDou	All	140	9520	73.49	89.31	1
BeiDou	All	140	9520	74.46	97.04	2
BeiDou	All	140	9520	93.89	96.72	3
BeiDou	All	140	9520	75.01	92.33	4
BeiDou	All	140	9520	65.01	90.33	5
BeiDou	All	140	9520	93.01	96.70	6
BeiDou	Low	140	9240	70.70	86.70	1
BeiDou	Low	140	9240	70.68	95.34	2
BeiDou	Low	140	9240	91.09	95.03	3
BeiDou	Low	140	9240	62.53	88.80	4
BeiDou	Low	140	9240	48.49	85.98	5
BeiDou	Low	140	9240	91.04	94.93	6
BeiDou	Mid	140	5740	79.09	96.45	1
BeiDou	Mid	140	5740	76.30	99.80	2
BeiDou	Mid	140	5740	97.25	99.50	3
BeiDou	Mid	140	5740	94.80	98.07	4
BeiDou	Mid	140	5740	75.46	96.89	5
BeiDou	Mid	140	5740	94.88	99.27	6
BeiDou	High	140	3500	78.87	96.46	1
BeiDou	High	140	3500	79.64	99.91	2
BeiDou	High	140	3500	98.36	99.82	3
BeiDou	High	140	3500	98.45	99.58	4
BeiDou	High	140	3500	95.74	99.38	5
BeiDou	High	140	3500	95.30	99.53	6

Using dual-frequency, CSMCT detects almost all artificially inserted Large CS for high-elevation angles. Method 3 and Method 6 has the highest success rate for detecting Small CS. Method 5 is the least successful method for detecting Small CS with low-elevation angles. In low-elevation angles, Method 3 and Method 6 have highest cycle-slip detection success rates. In high-elevation angles, the success rate of detecting cycle-slips are higher than other elevation angle boundaries. When the ionospheric activities are high, Method 5 give better success rates than Method 2. The success rates of all methods are similar for each GNSS constellation with high-elevation angles.

5.2.4. Results for Triple-Frequency Cycle-Slip Detection

A total of three methods have been used for triple-frequency cycle-slip detection. For different elevation angle boundaries have been used for each GNSS constellation. At least 150 repetitions applied to each continuous satellite observation arc. For each method and elevation angle boundaries, sufficient number of artificial cycle-slips have been inserted. The size of artificial cycle-slips insertions for each observation epoch have been divided into groups as (1-10) and (10-100) integer-cycles. The success rates of each station for triple-frequency cycle-slip detection methods for each day and method have been listed from Table 5.45 through Table 5.76:

Table 5.45. PTRF-CAN station results for triple-frequency GPS observations for the day 27.02.2023

Constellation	**Elevation Angle Boundaries**	**Rep. Number**	**Inserted CS**	**Small CS (1-10)%**	**Large CS (10-100)%**	**Method**
GPS	All	150	6150	99.41	100	1
GPS	All	150	6150	99.06	100	2
GPS	All	150	6150	96.44	99.09	3
GPS	Low	150	6150	99.74	99.61	1
GPS	Low	150	6150	99.20	99.59	2
GPS	Low	150	6150	96.86	99.35	3
GPS	Mid	150	4350	99.85	99.77	1
GPS	Mid	150	4350	99.85	99.77	2
GPS	Mid	150	4350	96.87	99.56	3
GPS	High	150	2700	100	100	1
GPS	High	150	2700	100	100	2
GPS	High	150	2700	97.3	100	3

Table 5.46. PTRF-CAN station results for triple-frequency GLONASS observations for the day 27.02.2023

Constellation	**Elevation Angle Boundaries**	**Rep. Number**	**Inserted CS**	**Small CS (1-10)%**	**Large CS (10-100)%**	**Method**
GLONASS	All	150	3750	99.65	99.68	1
GLONASS	All	150	3750	99.25	99.65	2
GLONASS	All	150	3750	96.61	99.33	3
GLONASS	Low	150	3750	99.81	99.73	1
GLONASS	Low	150	3750	99.12	99.63	2
GLONASS	Low	150	3750	97.01	99.52	3
GLONASS	Mid	150	2700	99.44	99.67	1
GLONASS	Mid	150	2700	99.45	99.67	2
GLONASS	Mid	150	2700	97.03	99.33	3
GLONASS	High	150	1350	100	100	1
GLONASS	High	150	1350	100	100	2
GLONASS	High	150	1350	97.04	100	3

Table 5.47 PTRF-CAN station results for triple-frequency Galileo observations for the day 27.02.2023

Constellation	**Elevation Angle Boundaries**	**Rep. Number**	**Inserted CS**	**Small CS (1-10)%**	**Large CS (10-100)%**	**Method**
Galileo	All	150	6750	99.23	99.65	1
Galileo	All	150	6750	98.14	99.50	2
Galileo	All	150	6750	97.38	98.84	3
Galileo	Low	150	6750	99.14	99.27	1
Galileo	Low	150	6750	96.57	99.01	2
Galileo	Low	150	6750	95.58	99.21	3
Galileo	Mid	150	4650	99.57	99.47	1
Galileo	Mid	150	4650	98.84	99.40	2
Galileo	Mid	150	4650	99.01	99.41	3
Galileo	High	150	2400	99.80	100	1
Galileo	High	150	2400	99.63	100	2
Galileo	High	150	2400	99.71	100	3

Table 5.48. PTRF-CAN station results for triple-frequency BeiDou observations for the day 27.02.2023

Constellation	**Elevation Angle Boundaries**	**Rep. Number**	**Inserted CS**	**Small CS (1-10)%**	**Large CS (10-100)%**	**Method**
BeiDou	All	150	2100	96.04	98.14	1
BeiDou	All	150	2100	96.00	98.11	2
BeiDou	All	150	2100	94.19	96.05	3
BeiDou	Low	150	2100	95.62	98.61	1
BeiDou	Low	150	2100	95.52	98.20	2
BeiDou	Low	150	2100	93.53	96.43	3
BeiDou	Mid	150	750	100	100	1
BeiDou	Mid	150	750	100	100	2
BeiDou	Mid	150	750	97.33	99.66	3
BeiDou	High	150	450	100	100	1
BeiDou	High	150	450	100	100	2
BeiDou	High	150	450	98.22	100	3

Table 5.49. FFMJ-DEU station results for triple-frequency GPS observations for the day 27.02.2023

Constellation	**Elevation Angle Boundaries**	**Rep. Number**	**Inserted CS**	**Small CS (1-10)%**	**Large CS (10-100)%**	**Method**
GPS	All	150	5550	99.53	99.51	1
GPS	All	150	5550	99.53	99.51	2
GPS	All	150	5550	96.54	99.17	3
GPS	Low	150	5550	99.55	99.62	1
GPS	Low	150	5550	99.50	99.62	2
GPS	Low	150	5550	97.30	99.14	3
GPS	Mid	150	4500	99.51	99.51	1
GPS	Mid	150	4500	99.51	99.51	2
GPS	Mid	150	4500	97.71	99.36	3
GPS	High	150	2700	99.71	100	1
GPS	High	150	2700	99.71	100	2
GPS	High	150	2700	97.96	99.44	3

Table 5.50. FFMJ-DEU station results for triple-frequency GLONASS observations for the day 27.02.2023

Constellation	**Elevation Angle Boundaries**	**Rep. Number**	**Inserted CS**	**Small CS (1-10)%**	**Large CS (10-100)%**	**Method**
GLONASS	All	150	4050	99.48	99.65	1
GLONASS	All	150	4050	99.43	99.65	2
GLONASS	All	150	4050	97.09	99.38	3
GLONASS	Low	150	2250	99.87	99.91	1
GLONASS	Low	150	2250	99.87	99.91	2
GLONASS	Low	150	2250	97.47	99.69	3
GLONASS	Mid	150	1200	100	100	1
GLONASS	Mid	150	1200	100	100	2
GLONASS	Mid	150	1200	97.08	99.83	3
GLONASS	High	150	2700	99.77	100	1
GLONASS	High	150	2700	99.33	100	2
GLONASS	High	150	2700	96.93	99.59	3

Table 5.51. FFMJ-DEU station results for triple-frequency Galileo observations for the day 27.02.2023

Constellation	**Elevation Angle Boundaries**	**Rep. Number**	**Inserted CS**	**Small CS (1-10)%**	**Large CS (10-100)%**	**Method**
Galileo	All	150	5250	99.16	99.30	1
Galileo	All	150	5250	98.02	99.20	2
Galileo	All	150	5250	97.94	99.26	3
Galileo	Low	150	5250	99.35	99.31	1
Galileo	Low	150	5250	96.50	98.97	2
Galileo	Low	150	5250	96.61	99.26	3
Galileo	Mid	150	4350	99.47	99.56	1
Galileo	Mid	150	4350	98.60	99.56	2
Galileo	Mid	150	4350	98.67	99.55	3
Galileo	High	150	2850	99.37	100	1
Galileo	High	150	2850	99.37	100	2
Galileo	High	150	2850	99.37	100	3

Table 5.52. FFMJ-DEU station results for triple-frequency BeiDou observations for the day 27.02.2023

Constellation	**Elevation Angle Boundaries**	**Rep. Number**	**Inserted CS**	**Small CS (1-10)%**	**Large CS (10-100)%**	**Method**
BeiDou	All	150	3300	99.61	99.39	1
BeiDou	All	150	3300	99.52	99.39	2
BeiDou	All	150	3300	97.70	99.15	3
BeiDou	Low	150	3300	99.42	99.52	1
BeiDou	Low	150	3300	99.36	99.51	2
BeiDou	Low	150	3300	97.85	99.33	3
BeiDou	Mid	150	2100	99.52	99.39	1
BeiDou	Mid	150	2100	99.52	99.39	2
BeiDou	Mid	150	2100	97.29	99.10	3
BeiDou	High	150	450	100	100	1
BeiDou	High	150	450	100	100	2
BeiDou	High	150	450	98.44	100	3

Table 5.53. MIZU-JPN station results for triple-frequency GPS observations for the day 27.02.2023

Constellation	**Elevation Angle Boundaries**	**Rep. Number**	**Inserted CS**	**Small CS (1-10)%**	**Large CS (10-100)%**	**Method**
GPS	All	150	5250	99.37	99.60	1
GPS	All	150	5250	99.22	99.56	2
GPS	All	150	5250	96.65	99.35	3
GPS	Low	150	5250	99.45	99.43	1
GPS	Low	150	5250	99.07	99.39	2
GPS	Low	150	5250	97.16	99.20	3
GPS	Mid	150	3900	99.79	99.69	1
GPS	Mid	150	3900	99.79	99.69	2
GPS	Mid	150	3900	96.92	99.49	3
GPS	High	150	2700	99.74	100	1
GPS	High	150	2700	99.74	100	2
GPS	High	150	2700	97.07	99.56	3

Table 5.54. MIZU-JPN station results for triple-frequency GLONASS observations for the day 27.02.2023

Constellation	Elevation Angle Boundaries	Rep. Number	Inserted CS	Small CS (1-10)%	Large CS (10-100)%	Method
GLONASS	All	150	2850	99.76	99.72	1
GLONASS	All	150	2850	99.58	99.68	2
GLONASS	All	150	2850	96.95	99.47	3
GLONASS	Low	150	2850	99.72	99.65	1
GLONASS	Low	150	2850	99.19	99.61	2
GLONASS	Low	150	2850	97.37	99.47	3
GLONASS	Mid	150	2100	99.86	99.90	1
GLONASS	Mid	150	2100	99.81	99.90	2
GLONASS	Mid	150	2100	97.10	99.62	3
GLONASS	High	150	1650	100	100	1
GLONASS	High	150	1650	100	100	2
GLONASS	High	150	1650	97.15	99.64	3

Table 5.55. MIZU-JPN station results for triple-frequency Galileo observations for the day 27.02.2023

Constellation	Elevation Angle Boundaries	Rep. Number	Inserted CS	Small CS (1-10)%	Large CS (10-100)%	Method
Galileo	All	150	4800	99.21	99.33	1
Galileo	All	150	4800	98.33	98.79	2
Galileo	All	150	4800	97.67	99.09	3
Galileo	Low	150	4800	98.56	98.63	1
Galileo	Low	150	4800	95.05	98.19	2
Galileo	Low	150	4800	94.81	98.56	3
Galileo	Mid	150	3750	99.36	99.63	1
Galileo	Mid	150	3750	98.67	99.60	2
Galileo	Mid	150	3750	98.57	99.63	3
Galileo	High	150	2550	99.73	100	1
Galileo	High	150	2550	99.69	100	2
Galileo	High	150	2550	99.63	100	3

Table 5.56. MIZU-JPN station results for triple-frequency BeiDou observations for the day 27.02.2023

Constellation	**Elevation Angle Boundaries**	**Rep. Number**	**Inserted CS**	**Small CS (1-10)%**	**Large CS (10-100)%**	**Method**
BeiDou	All	150	4350	99.47	99.97	1
BeiDou	All	150	4350	99.47	99.77	2
BeiDou	All	150	4350	97.43	99.20	3
BeiDou	Low	150	3900	99.28	99.33	1
BeiDou	Low	150	3900	99.25	99.32	2
BeiDou	Low	150	3900	96.69	99.03	3
BeiDou	Mid	150	2700	99.74	99.67	1
BeiDou	Mid	150	2700	99.73	99.67	2
BeiDou	Mid	150	2700	97.81	99.52	3
BeiDou	High	150	1800	99.88	100	1
BeiDou	High	150	1800	99.83	100	2
BeiDou	High	150	1800	97.89	99.39	3

Table 5.57. LPGS-ARG station results for triple-frequency GPS observations for the day 27.02.2023

Constellation	**Elevation Angle Boundaries**	**Rep. Number**	**Inserted CS**	**Small CS (1-10)%**	**Large CS (10-100)%**	**Method**
GPS	All	150	5250	99.26	99.43	1
GPS	All	150	5250	98.84	99.37	2
GPS	All	150	5250	96.59	99.24	3
GPS	Low	150	5250	99.26	99.35	1
GPS	Low	150	5250	98.72	99.30	2
GPS	Low	150	5250	97.03	99.01	3
GPS	Mid	150	3600	99.64	99.59	1
GPS	Mid	150	3600	99.58	99.56	2
GPS	Mid	150	3600	97.25	99.36	3
GPS	High	150	2700	99.81	100	1
GPS	High	150	2700	99.80	100	2
GPS	High	150	2700	97.63	99.37	3

Table 5.58. LPGS-ARG station results for triple-frequency GLONASS observations for the day 27.02.2023

Constellation	Elevation Angle Boundaries	Rep. Number	Inserted CS	Small CS (1-10)%	Large CS (10-100)%	Method
GLONASS	All	150	150	100	100	1
GLONASS	All	150	150	100	100	2
GLONASS	All	150	150	97.33	100	3
GLONASS	Low	150	150	99.33	100	1
GLONASS	Low	150	150	98.00	100	2
GLONASS	Low	150	150	97.33	99.63	3
GLONASS	Mid	150	150	100	100	1
GLONASS	Mid	150	150	100	100	2
GLONASS	Mid	150	150	98.66	100	3
GLONASS	High	150	150	100	100	1
GLONASS	High	150	150	100	100	2
GLONASS	High	150	150	99.45	100	3

Table 5.59. LPGS-ARG station results for triple-frequency Galileo observations for the day 27.02.2023

Constellation	Elevation Angle Boundaries	Rep. Number	Inserted CS	Small CS (1-10)%	Large CS (10-100)%	Method
Galileo	All	150	8400	99.33	99.27	1
Galileo	All	150	8400	96.43	98.89	2
Galileo	All	150	8400	96.24	99.21	3
Galileo	Low	150	8250	99.41	99.27	1
Galileo	Low	150	8250	95.08	98.73	2
Galileo	Low	150	8250	95.36	99.19	3
Galileo	Mid	150	4200	99.45	99.62	1
Galileo	Mid	150	4200	97.83	99.45	2
Galileo	Mid	150	4200	97.76	99.57	3
Galileo	High	150	2550	99.80	100	1
Galileo	High	150	2550	99.76	100	2
Galileo	High	150	2550	99.80	100	3

Table 5.60. LPGS-ARG station results for triple-frequency BeiDou observations for the day 27.02.2023

Constellation	**Elevation Angle Boundaries**	**Rep. Number**	**Inserted CS**	**Small CS (1-10)%**	**Large CS (10-100)%**	**Method**
BeiDou	All	150	900	99.56	99.78	1
BeiDou	All	150	900	98.11	99.67	2
BeiDou	All	150	900	98.11	99.67	3
BeiDou	Low	150	900	99.67	100	1
BeiDou	Low	150	900	98.00	99.78	2
BeiDou	Low	150	900	97.89	99.78	3
BeiDou	Mid	150	450	100	99.88	1
BeiDou	Mid	150	450	100	99.87	2
BeiDou	Mid	150	450	98.22	99.34	3
BeiDou	High	150	450	100	100	1
BeiDou	High	150	450	100	100	2
BeiDou	High	150	450	98.44	100	3

Table 5.61. PTRF-CAN station results for triple-frequency GPS observations for the day 25.05.2023

Constellation	**Elevation Angle Boundaries**	**Rep. Number**	**Inserted CS**	**Small CS (1-10)%**	**Large CS (10-100)%**	**Method**
GPS	All	150	6600	99.40	99.44	1
GPS	All	150	6600	99.02	99.42	2
GPS	All	150	6600	96.76	99.26	3
GPS	Low	150	6600	99.50	99.60	1
GPS	Low	150	6600	99.03	99.53	2
GPS	Low	150	6600	96.98	99.41	3
GPS	Mid	150	4350	99.63	99.59	1
GPS	Mid	150	4350	99.63	99.58	2
GPS	Mid	150	4350	96.80	99.45	3
GPS	High	150	2700	99.78	100	1
GPS	High	150	2700	99.78	100	2
GPS	High	150	2700	97.48	100	3

Table 5.62. PTRF-CAN station results for triple-frequency GLONASS observations for the day 25.05.2023

Constellation	**Elevation Angle Boundaries**	**Rep. Number**	**Inserted CS**	**Small CS (1-10)%**	**Large CS (10-100)%**	**Method**
GLONASS	All	150	4650	99.40	99.42	1
GLONASS	All	150	4650	98.56	99.33	2
GLONASS	All	150	4650	96.67	99.18	3
GLONASS	Low	150	4650	99.53	99.51	1
GLONASS	Low	150	4650	98.45	99.40	2
GLONASS	Low	150	4650	97.10	99.23	3
GLONASS	Mid	150	2700	99.63	99.78	1
GLONASS	Mid	150	2700	99.63	99.78	2
GLONASS	Mid	150	2700	96.79	99.59	3
GLONASS	High	150	1350	100	100	1
GLONASS	High	150	1350	100	100	2
GLONASS	High	150	1350	97.63	99.41	3

Table 5.63. PTRF-CAN station results for triple-frequency Galileo observations for the day 25.05.2023

Constellation	**Elevation Angle Boundaries**	**Rep. Number**	**Inserted CS**	**Small CS (1-10)%**	**Large CS (10-100)%**	**Method**
Galileo	All	150	6150	99.35	99.33	1
Galileo	All	150	6150	98.52	99.26	2
Galileo	All	150	6150	98.46	99.32	3
Galileo	Low	150	6150	99.61	99.54	1
Galileo	Low	150	6150	97.73	99.27	2
Galileo	Low	150	6150	97.53	99.53	3
Galileo	Mid	150	4350	99.38	99.52	1
Galileo	Mid	150	4350	99.06	99.47	2
Galileo	Mid	150	4350	99.04	99.52	3
Galileo	High	150	2400	100	100	1
Galileo	High	150	2400	100	100	2
Galileo	High	150	2400	100	100	3

Table 5.64. PTRF-CAN station results for triple-frequency BeiDou observations for the day 25.05.2023

Constellation	Elevation Angle Boundaries	Rep. Number	Inserted CS	Small CS (1-10)%	Large CS (10-100)%	Method
BeiDou	All	150	1800	98.94	99.17	1
BeiDou	All	150	1800	98.94	99.17	2
BeiDou	All	150	1800	97.56	98.83	3
BeiDou	Low	150	1800	98.50	98.72	1
BeiDou	Low	150	1800	98.50	98.72	2
BeiDou	Low	150	1800	96.17	98.50	3
BeiDou	Mid	150	750	100	100	1
BeiDou	Mid	150	750	100	100	2
BeiDou	Mid	150	750	97.07	99.73	3
BeiDou	High	150	450	100	100	1
BeiDou	High	150	450	100	100	2
BeiDou	High	150	450	98.00	100	3

Table 5.65. FFMJ-DEU station results for triple-frequency GPS observations for the day 25.05.2023

Constellation	Elevation Angle Boundaries	Rep. Number	Inserted CS	Small CS (1-10)%	Large CS (10-100)%	Method
GPS	All	150	5250	99.29	99.31	1
GPS	All	150	5250	99.24	99.31	2
GPS	All	150	5250	97.07	99.10	3
GPS	Low	150	5250	99.56	99.50	1
GPS	Low	150	5250	99.55	99.50	2
GPS	Low	150	5250	96.51	99.22	3
GPS	Mid	150	4500	99.59	99.60	1
GPS	Mid	150	4500	99.59	99.59	2
GPS	Mid	150	4500	96.98	99.37	3
GPS	High	150	2700	99.85	100	1
GPS	High	150	2700	99.85	100	2
GPS	High	150	2700	97.04	100	3

Table 5.66. FFMJ-DEU station results for triple-frequency GLONASS observations for the day 25.05.2023

Constellation	**Elevation Angle Boundaries**	**Rep. Number**	**Inserted CS**	**Small CS (1-10)%**	**Large CS (10-100)%**	**Method**
GLONASS	All	150	3450	99.22	99.65	1
GLONASS	All	150	3450	99.07	99.68	2
GLONASS	All	150	3450	96.70	99.42	3
GLONASS	Low	150	2250	99.91	99.91	1
GLONASS	Low	150	2250	99.91	99.96	2
GLONASS	Low	150	2250	96.58	99.69	3
GLONASS	Mid	150	1650	99.88	99.88	1
GLONASS	Mid	150	1650	99.88	99.88	2
GLONASS	Mid	150	1650	97.03	99.64	3
GLONASS	High	150	2400	99.63	100	1
GLONASS	High	150	2400	99.21	100	2
GLONASS	High	150	2400	97.17	99.58	3

Table 5.67. FFMJ-DEU station results for triple-frequency Galileo observations for the day 25.05.2023

Constellation	**Elevation Angle Boundaries**	**Rep. Number**	**Inserted CS**	**Small CS (1-10)%**	**Large CS (10-100)%**	**Method**
Galileo	All	150	6000	99.30	99.05	1
Galileo	All	150	6000	98.63	99.00	2
Galileo	All	150	6000	98.67	99.03	3
Galileo	Low	150	6000	99.37	99.45	1
Galileo	Low	150	6000	97.78	99.20	2
Galileo	Low	150	6000	97.70	99.38	3
Galileo	Mid	150	4350	99.49	99.63	1
Galileo	Mid	150	4350	99.36	99.29	2
Galileo	Mid	150	4350	99.24	99.33	3
Galileo	High	150	2550	100	100	1
Galileo	High	150	2550	100	100	2
Galileo	High	150	2550	100	100	3

Table 5.68. FFMJ-DEU station results for triple-frequency BeiDou observations for the day 25.05.2023

Constellation	Elevation Angle Boundaries	Rep. Number	Inserted CS	Small CS (1-10)%	Large CS (10-100)%	Method
BeiDou	All	150	2400	99.79	99.88	1
BeiDou	All	150	2400	99.79	99.88	2
BeiDou	All	150	2400	97.75	99.80	3
BeiDou	Low	150	2400	99.79	99.58	1
BeiDou	Low	150	2400	99.83	99.58	2
BeiDou	Low	150	2400	97.92	99.38	3
BeiDou	Mid	150	1950	99.79	99.85	1
BeiDou	Mid	150	1950	99.79	99.85	2
BeiDou	Mid	150	1950	97.85	99.69	3
BeiDou	High	150	300	100	100	1
BeiDou	High	150	300	100	100	2
BeiDou	High	150	300	99.05	100	3

Table 5.69. MIZU-JPN station results for triple-frequency GPS observations for the day 25.05.2023

Constellation	Elevation Angle Boundaries	Rep. Number	Inserted CS	Small CS (1-10)%	Large CS (10-100)%	Method
GPS	All	150	5400	99.43	99.27	1
GPS	All	150	5400	99.37	99.28	2
GPS	All	150	5400	96.52	99.04	3
GPS	Low	150	5400	99.06	99.22	1
GPS	Low	150	5400	98.93	99.22	2
GPS	Low	150	5400	96.93	99.02	3
GPS	Mid	150	3600	99.67	99.73	1
GPS	Mid	150	3600	99.67	99.72	2
GPS	Mid	150	3600	97.11	99.64	3
GPS	High	150	2550	99.73	100	1
GPS	High	150	2550	99.73	100	2
GPS	High	150	2550	97.10	99.65	3

Table 5.70. MIZU-JPN station results for triple-frequency GLONASS observations for the day 25.05.2023

Constellation	Elevation Angle Boundaries	Rep. Number	Inserted CS	Small CS (1-10)%	Large CS (10-100)%	Method
GLONASS	All	150	2850	99.51	99.79	1
GLONASS	All	150	2850	99.40	99.79	2
GLONASS	All	150	2850	96.67	99.51	3
GLONASS	Low	150	2850	99.51	99.47	1
GLONASS	Low	150	2850	98.95	99.40	2
GLONASS	Low	150	2850	96.81	99.19	3
GLONASS	Mid	150	2250	99.82	99.99	1
GLONASS	Mid	150	2250	99.81	99.95	2
GLONASS	Mid	150	2250	96.80	99.07	3
GLONASS	High	150	1650	99.96	100	1
GLONASS	High	150	1650	99.96	100	2
GLONASS	High	150	1650	96.67	99.92	3

Table 5.71. MIZU-JPN station results for triple-frequency Galileo observations for the day 25.05.2023

Constellation	Elevation Angle Boundaries	Rep. Number	Inserted CS	Small CS (1-10)%	Large CS (10-100)%	Method
Galileo	All	150	5100	99.51	99.69	1
Galileo	All	150	5100	98.51	99.37	2
Galileo	All	150	5100	98.45	99.53	3
Galileo	Low	150	5100	99.02	99.59	1
Galileo	Low	150	5100	96.78	99.22	2
Galileo	Low	150	5100	96.65	99.51	3
Galileo	Mid	150	3750	99.73	99.89	1
Galileo	Mid	150	3750	99.36	99.39	2
Galileo	Mid	150	3750	99.25	99.44	3
Galileo	High	150	2550	99.80	100	1
Galileo	High	150	2550	99.79	100	2
Galileo	High	150	2550	99.76	100	3

Table 5.72. MIZU-JPN station results for triple-frequency BeiDou observations for the day 25.05.2023

Constellation	Elevation Angle Boundaries	Rep. Number	Inserted CS	Small CS (1-10)%	Large CS (10-100)%	Method
BeiDou	All	150	4350	99.59	100	1
BeiDou	All	150	4350	99.59	99.55	2
BeiDou	All	150	4350	97.40	99.26	3
BeiDou	Low	150	3900	99.64	99.46	1
BeiDou	Low	150	3900	99.63	99.45	2
BeiDou	Low	150	3900	97.90	99.23	3
BeiDou	Mid	150	2550	99.49	99.81	1
BeiDou	Mid	150	2550	99.50	99.80	2
BeiDou	Mid	150	2550	96.90	99.69	3
BeiDou	High	150	1500	99.93	100	1
BeiDou	High	150	1500	99.92	100	2
BeiDou	High	150	1500	98.00	99.60	3

Table 5.73. LPGS-ARG station results for triple-frequency GPS observations for the day 25.05.2023

Constellation	Elevation Angle Boundaries	Rep. Number	Inserted CS	Small CS (1-10)%	Large CS (10-100)%	Method
GPS	All	150	6450	99.29	99.44	1
GPS	All	150	6450	98.70	99.42	2
GPS	All	150	6450	96.60	99.22	3
GPS	Low	150	6300	99.70	99.83	1
GPS	Low	150	6300	98.76	99.65	2
GPS	Low	150	6300	97.27	99.62	3
GPS	Mid	150	4050	99.68	99.88	1
GPS	Mid	150	4050	99.63	99.90	2
GPS	Mid	150	4050	97.19	99.33	3
GPS	High	150	2700	99.81	100	1
GPS	High	150	2700	99.81	100	2
GPS	High	150	2700	97.00	99.63	3

Table 5.74. LPGS-ARG station results for triple-frequency GLONASS observations for the day 25.05.2023

Constellation	**Elevation Angle Boundaries**	**Rep. Number**	**Inserted CS**	**Small CS (1-10)%**	**Large CS (10-100)%**	**Method**
GLONASS	All	150	300	100	100	1
GLONASS	All	150	300	100	100	2
GLONASS	All	150	300	95.33	100	3
GLONASS	Low	150	300	99.67	100	1
GLONASS	Low	150	300	97.67	100	2
GLONASS	Low	150	300	96.33	99.63	3
GLONASS	Mid	150	300	100	100	1
GLONASS	Mid	150	300	100	100	2
GLONASS	Mid	150	300	96.33	99.67	3
GLONASS	High	150	300	100	100	1
GLONASS	High	150	300	100	100	2
GLONASS	High	150	300	95.66	100	3

Table 5.75. LPGS-ARG station results for triple-frequency Galileo observations for the day 25.05.2023

Constellation	**Elevation Angle Boundaries**	**Rep. Number**	**Inserted CS**	**Small CS (1-10)%**	**Large CS (10-100)%**	**Method**
Galileo	All	150	9600	99.06	99.08	1
Galileo	All	150	9600	96.48	98.88	2
Galileo	All	150	9600	96.44	99.04	3
Galileo	Low	150	9600	99.02	99.05	1
Galileo	Low	150	9600	95.58	98.61	2
Galileo	Low	150	9600	95.47	99.00	3
Galileo	Mid	150	4050	99.39	99.46	1
Galileo	Mid	150	4050	99.01	99.43	2
Galileo	Mid	150	4050	98.99	99.46	3
Galileo	High	150	2550	99.77	100	1
Galileo	High	150	2550	99.76	100	2
Galileo	High	150	2550	99.77	100	3

Table 5.76. LPGS-ARG station results for triple-frequency BeiDou observations for the day 25.05.2023

Constellation	**Elevation Angle Boundaries**	**Rep. Number**	**Inserted CS**	**Small CS (1-10)%**	**Large CS (10-100)%**	**Method**
BeiDou	All	150	1650	99.82	99.88	1
BeiDou	All	150	1650	99.15	99.76	2
BeiDou	All	150	1650	97.70	99.58	3
BeiDou	Low	150	1650	99.15	99.94	1
BeiDou	Low	150	1650	98.30	99.82	2
BeiDou	Low	150	1650	97.76	99.94	3
BeiDou	Mid	150	900	100	100	1
BeiDou	Mid	150	900	99.67	100	2
BeiDou	Mid	150	900	97.33	100	3
BeiDou	High	150	450	100	100	1
BeiDou	High	150	450	100	100	2
BeiDou	High	150	450	98.67	100	3

Using triple-frequency, CSMCT detects almost all artificially inserted Large CS. Method 1 has the highest success rate for detecting Small CS. Since Method 1 is not effected from ionospheric activities, the success rates of this method is similar for each day. Method 3 is the least successful method for detecting Small CS. In low-elevation angles, all methods have smaller detection success rates. In high-elevation angles, the success rate of detecting cycle-slips are higher than other elevation angle boundaries. The success rates of all methods are similar for each GNSS constellation.

6. DISCUSSION AND CONCLUSION

The primary goal of this thesis is to compare cycle-slip detection methods for single, dual and triple frequency for multi-GNSS observations. The success rates of the cycle-slip detection methods in different situations were examined. For this purpose, a software named CSMCT has been developed. In addition, the results were evaluated for small (1-10) and large (10-100) integer-cycle intervals with the help of artificially created and randomly inserted cycle-slips into observation arcs and these sizes are determined randomly in accordance with the nature of the cycle-slip. In order to determine the effects of satellite elevation angles on the results of cycle-slip detection methods, satellite elevation angles are divided into 5°-20°, 20°-50°and 50°-90° ranges. In addition, 5°-90° was also evaluated to see the overall performance of the methods without categorizing them according to elevation angles. The overall percentage values of each method were determined and data about the success of the methods were obtained. The conclusions obtained as a result of all this flow and the open-for-discussion areas will be assessed. Recommendations will be given on the fields that are open to development and on the business lines that this field can be integrated in the light of the literature research conducted within the scope of the thesis.

6.1. Conclusion

A software that compares each cycle-slip detection method for single, dual, and triple frequency was seen as a deficiency in the literature for cycle-slip detection; therefore, a software called CSMCT was developed. Areas that are open to development have been determined for this study using MATLAB environment. Within the scope of the study, the GNSS constellations that reached global coverage were selected and these are GPS, GLONASS, Galileo and BeiDou, respectively. CSMCT has a total of five processing stages. These are file import, parameter selection, method selection, artificial cycle-slip insertion and detection analysis, respectively. The interface of CSMCT, which has been designed to respond in accordance with the cycle-slip nature that enables the generation of vastly different test environments, has been carefully developed to be user-friendly. All cycle-slip metadata required for cycle-slip detection are reflected in the result table. The overall performances of the methods according to the frequencies are also added to the result interface.

The data for the two selected dates, 27.02.2023 and 25.05.2023 were compared, respectively, and 4 globally spread GNSS stations, located in Canada, Germany, Japan, and Argentina, respectively, were chosen to collect 24-h observation data for these days in a static mode. Observation data of at least three different frequencies and artificial cycle-slips for single, double, and triple-frequency were added to observation data of each station in four selected GNSS constellations. The results of the algorithm were obtained, which operates by inserting one artificial cycle-slip in each continuous satellite observation arc, to a different epoch chosen by the algorithm each time. Since the total observation epoch of the continuous observation arcs during the day is not the same, the same amount of artificial cycle-slip is not applied to each GNSS constellation for the lengths of the observation arcs to be long enough.

Single-frequency results gave average results in all three constellations, as mentioned in Section 3.3.1. According to the given threshold value, the success rates in the code-phase comparison method generally depend on the code-pseudorange observation noise. If the observation noises are low, it is seen in the results that the success rates are quite high. In addition, the biggest disadvantage of this method is the accuracy of code-pseudorange observations. Since the code-phase comparison algorithm does not give high accuracy between 1-10 cycles, it will not be very accurate to use in applications where precise point positioning is performed without an enhanced method. However, Large CS values can be used to work with low-cost receivers for each constellation, providing high success rate conditions. In single-frequency results, Galileo gives the best values, even on the day 27.02.2023 when ionospheric effects are high. Each constellation performs quite well at high satellite elevation angles, and the effect of low elevation angles mentioned in the cycle-slip occurrence has been confirmed. The approximate results of the algorithms with single-frequency data are 66 seconds for each satellite elevation angle range, 61 seconds for the mid elevation angle, and 55 seconds for the high elevation angle. This is because the number of observation arcs are low for high elevation angles. In summary, it is known that Galileo has the lowest code-pseudorange observation noise, which gives the best success rates. GPS and BeiDou give approximate values compared to each other and lower success rates than Galileo. GLONASS gives the lowest success rates because the code-pseudorange observation noises are quite high compared to Galileo.

In dual-frequency observations, it is seen that all artificial cycle-slips can be found when it comes to high satellite elevation angles with Large CS. In this scenario, methods 2,3,4 and 5 achieved full success rate by finding all cycle-slips. The reason why the values are very close to each other when the satellite elevation angles are kept low is because there are more observation arcs at low elevation angles. Therefore, it is seen that the results are very close to the low satellite elevation angle when satellite elevation angle intervals are not activated. Method 2 and 5 use the same equations but method 5 uses ionospheric correction and it gives better results than method 2. Sometimes, method 5 gives very low success rates when it comes to low elevation angles. It is assumed that as a result of using the MWWL combination of method 5, random artificial cycle-slip sizes are determined by the values chosen by the algorithm between 1-3 cycles and the effect of ionospheric delays on the signal increases. As expected, all methods have reached the maximum success rate where Large CS and elevation angle boundaries are high. However, in low-elevation and Small CS cases, the success rates of method 5 are especially low. When the elevation angle factor was not categorized in dual-frequency observations, method 2 had the lowest success rates. Method 4 and method 6 give the highest values. The reason for this is that the error that affects most observations except ionospheric effects is eliminated. It has been understood that the results obtained according to the nature of the cycle-slip will be quite high if the ionospheric effects are eliminated, but due to the nature of the equation used by methods 2 and 5, high success rates cannot be obtained in very small cycle-slips. The elapsed times of the algorithms with dual-frequency data are 121 seconds for each satellite elevation angle range, 117 seconds for the mid elevation angle, and 110 seconds for the high elevation angle, respectively.

In triple-frequency observations, the success rates are obviously higher than the single and dual-frequency observations. The biggest advantage of triple-frequency is that it gives very high success rates, and these values do not change in all GNSS constellations, except for minor differences. The greatest benefit of triple frequency is that it yields consistent results in both Small and Large CS’s. Not all satellites in each GNSS constellation can send data on three frequencies yet. Therefore, the amount of artificially added cycle-slips was kept slightly lower than in other experiments to prevent too much distortion of the data.

Success rates do not fall below %95 in each method and at all elevation angles. The only exception is the success rate of %93.53 given by method 3 at low elevation angle in BeiDou observations of PTRF-CAN station. Method 1 gives the highest success rates, the most important reason for this is that it is not affected by ionospheric delay. Although Method 2 provides extremely high success rates, it cannot be as consistent as Method 1. Although Method 3 gives relatively lower percentages because of Small CSs compared to other methods, its success rates in Large CSs are very close to the other two methods. Detection success rates in all GNSS constellations are very close to each other and almost all cycle-slips can be detected successfully for each of them. In this case, if triple-frequency can be used, very high success rates can be achieved in cycle-slip detection. In addition, a real-time algorithm was used for triple-frequency and the results obtained are quite satisfactory. Since all cycle-slip values are inserted randomly, the combination used in Method 1 cannot detect some cycle-slip pairs. In fact, these three methods are used as a whole for the detection and repair of cycle-slips in the original observations. The detection success rates of each method influence the success rate of the following method. If a mistake is made in the cycle-slip detection stages and the success rates given by the algorithms are lower than necessary, adequate results will not be obtained from cycle-slip repair in the original observations. The elapsed times of the algorithms with triple-frequency data are 39 seconds for each satellite elevation angle range, 36 seconds for mid-elevation angle range. The elapsed times of the algorithms for high elevation angle ranges vary significantly, from 10 seconds to 32 seconds, respectively.

6.2. Recommendations for Further Studies

- All these methods, whose detections are made, can be repaired in accordance with the cycle-slip nature. These methods can be evaluated by supplying the software with all of the cycle-slip detection and repair steps, as well as by utilizing various statistical tests. Users can develop their own detection techniques, compare them to the software’s traditional algorithms, and test their algorithm.
- Currently, GNSS constellations transmit signals with five frequencies. By developing algorithms that employ more frequencies, both the number of possible combinations and the level of accuracy of detection results can be increased. In this way, CSMCT can be a pioneer together with the innovation of GNSS.

- The artificial cycle-slip insertion process of CSMCT can be updated to save a lot of time by automating it, and it is essential that it be upgraded in terms of data visualization.
- By making all selectable software parameters dynamic, it is possible to test, develop, and optimize traditional cycle-slip detection methods.
- It can be developed in such a way that CSMCT can perform and visualize all the operations required for the cycle-slip, and can be made available to the entire GNSS world to directly use and process data. The software can be enhanced with the data science and machine learning techniques of the developing world, enabling analysis in the data field. By interacting with other programming languages and tools, CSMCT's analysis capabilities can be significantly enhanced.
- For further studies, research on how algorithms react to insensitive cycle-slip pairs can be added. Because these pairs can reduce the success rate of some methods considerably.

7. REFERENCES

[1] E. Hofmann-Wellenhof, Bernhard, Lichtenegger, Herbert, Wasle, GNSS — Global Navigation Satellite Systems, Springer Vienna, Vienna, **2008**.

[2] C.J. Hegarty, E. Chatre, Evolution of the Global Navigation SatelliteSystem (GNSS), Proc. IEEE. 96 (**2008**) 1902–1917.

[3] A. Shabanloui, A new approach for a kinematical dynamical determination of low satellite orbits based on GNSS observations, (**2008**).

[4] J.L. Ta, Global Positioning System, California State University Channel Islands, **2011**.

[5] B. Nejad, Introduction to Satellite Ground Segment Systems Engineering: Principles and Operational Aspects, Springer, **2022**.

[6] P.L.N. Raju, Fundamentals of GPS, Satell. Remote Sens. GIS Appl. Agric. Meteorol. (**2004**) 121.

[7] K.M. Larson, GPS interferometric reflectometry: applications to surface soil moisture, snow depth, and vegetation water content in the western United States, Wiley Interdiscip. Rev. Water. 3 (**2016**) 775–787.

[8] C. Specht, M. Mania, M. Skóra, M. Specht, Accuracy of the GPS Positioning System in the Context of Increasing the Number of Satellites in the Constellation, Polish Marit. Res. 22 (**2015**) 9–14.

[9] E. Ali, Global Positioning System (GPS): Definition, Principles, Errors, Applications & DGPS, No. April. (**2020**).

[10] A. Michalski, J. Czajewski, The accuracy of the global positioning systems, IEEE Instrum. Meas. Mag. 7 (**2004**) 56–60.

[11] J.S. Subirana, J.M.J. Zornoza, M. Hernandez-Pajares, GNSS data processing, Vol. I: fundamentals and algorithms, ESA Commun. (**2013**) 6.

[12] D.N. Koster, A.I.R.F.I.O.F.T.W.-P.A.F.B.O.H.S.O.F. ENGINEERING, A Model of Global Positioning System (GPS) Master Control Station (MCS) Operations, (**1992**).

[13] M.S. Grewal, L.R. Weill, A.P. Andrews, Global positioning systems, inertial navigation, and integration, John Wiley & Sons, **2007**.

[14] P. Kumar, P.K. Srivastava, P. Tiwari, R.K. Mall, Application of GPS and GNSS technology in geosciences, GPS GNSS Technol. Geosci. (**2021**) 415–427.

[15] G.L. Cook, GLONASS Performance, 1995–1997, and GPS-GLONASS Interoperability Issues, Navigation. 44 (**1997**) 291–300.

[16] S. Shanmugam, J. Jones, A. MacAulay, A.J. Van Dierendonck, Evolution to modernized GNSS ionoshperic scintillation and TEC monitoring, in: Proc. 2012 IEEE/ION Position, Locat. Navig. Symp., IEEE, **2012**: pp. 265–273.

[17] S. Revnivykh, A. Bolkunov, A. Serdyukov, O. Montenbruck, Glonass, Springer Handb. Glob. Navig. Satell. Syst. (**2017**) 219–245.

[18] C. Shi, N. Wei, Satellite navigation for digital earth, Man. Digit. Earth. (**2020**) 125–160.

[19] P.J.G. Teunissen, O. Montenbruck, Springer Handbook of Global Navigation Satellite Systems, Springer International Publishing, Cham, **2017**.

[20] D. Odijk, Ionosphere-Free Phase Combinations for Modernized GPS, J. Surv. Eng. 129 (**2003**) 165–173.

[21] R. Warnant, U. Foelsche, M. Aquino, B. Bidaine, V. Gherm, M.M. Hoque, I. Kutiev, S. Lejeune, J.-P. Luntama, J. Spits, Mitigation of ionospheric effects on GNSS, Ann. Geophys. 52 (**2009**).

[22] R. Aoyama, China's dichotomous BeiDou strategy: led by the party for national deployment, driven by the market for global reach, J. Contemp. East Asia Stud. 11 (**2022**) 282–299.

[23] E. Hagt, China's Beidou: Implications for the Individual and the State, SAIS Rev. Int'l Aff. 34 (**2014**) 129.

[24] S. Madry, Global navigation satellite systems and their applications, Springer, **2015**.

[25] N.L. Johnson, Medium Earth Orbits: is there a need for a third protected region?, in: 61st Int. Astronaut. Congr., **2010**.

[26] X. Ma, X. Dong, Y. Hu, Analysis on navigation accuracy of high orbit spacecraft based on BDS GEO and IGSO satellites, Adv. Sp. Res. 71 (2023) 2481–2492.

[27] G. Xu, Y. Xu, GPS: Theory, algorithms and applications, third edition, Springer Berlin Heidelberg, Berlin, Heidelberg, **2016**.

[28] C. Shi, X. Wu, F. Zheng, X. Wang, J. Wang, Modeling of BDS-2/BDS-3 single-frequency PPP with B1I and B1C signals and positioning performance analysis, Measurement. 178 (**2021**) 109355.

[29] R. Li, S. Zheng, E. Wang, J. Chen, S. Feng, D. Wang, L. Dai, Advances in BeiDou Navigation Satellite System (BDS) and satellite navigation augmentation technologies, Satell. Navig. 1 (**2020**) 1–23.

[30] A. Noureldin, T.B. Karamat, J. Georgy, Fundamentals of inertial navigation, satellite-based positioning and their integration, Springer Science & Business Media, **2012**.

[31] Y. Yang, J. Tang, O. Montenbruck, Chinese navigation satellite systems, Springer Handb. Glob. Navig. Satell. Syst. (**2017**) 273–304.

[32] J. Xie, H. Wang, P. Li, Y. Meng, J. Xie, H. Wang, P. Li, Y. Meng, Overview of Navigation Satellite Systems, Satell. Navig. Syst. Technol. (**2021**) 35–66.

[33] Q. Zhang, Z. Chen, Y. Cui, X. Zheng, F. Rong, Y. Sun, L. Gao, A refined metric for multi-GNSS constellation availability assessment in polar regions, Adv. Sp. Res. 66 (**2020**) 655–670.

[34] X. Zhang, M. Wu, W. Liu, X. Li, S. Yu, C. Lu, J. Wickert, Initial assessment of the COMPASS/BeiDou-3: New-generation navigation signals, J. Geod. 91 (**2017**) 1225–1240.

[35] Y. Yang, W. Gao, S. Guo, Y. Mao, Y. Yang, Introduction to BeiDou-3 navigation satellite system, Navigation. 66 (**2019**) 7–18.

[36] Y. Yang, Y. Xu, J. Li, C. Yang, Progress and performance evaluation of BeiDou global navigation satellite system: Data analysis based on BDS-3 demonstration

system, Sci. China Earth Sci. 61 (**2018**) 614–624.

[37] A.E. Süzer, H. Oktal, PRN code correlation in GPS receiver, in: 2017 8th Int. Conf. Recent Adv. Sp. Technol., IEEE, **2017**: pp. 189–193.

[38] Q. Congshan, X. Hualong, T. Ying, Navigation and Positioning System Based on GPS & CDMA, in: 2007 2nd IEEE Conf. Ind. Electron. Appl., IEEE, **2007**: pp. 2843–2846.

[39] S. Zaminpardaz, P.J.G. Teunissen, A. Khodabandeh, GLONASS–only FDMA+CDMA RTK: Performance and outlook, GPS Solut. 25 (**2021**) 96.

[40] Y. Urlichich, V. Subbotin, G. Stupak, V. Dvorkin, A. Povalyaev, S. Karutin, GLONASS modernization, in: Proc. 24th Int. Tech. Meet. Satell. Div. Inst. Navig. (ION GNSS 2011), **2011**: pp. 3125–3128.

[41] H.Z. Abidin, 8 Fundamentals of GPS Signals and Data, Man. Geospatial Sci. Technol. (**2010**) 115.

[42] C.A. Ogaja, Applied GPS for engineers and project managers, American Society of Civil Engineers, Reston, VA, **2011**.

[43] R. Hatch, The synergism of GPS code and carrier measurements, in: Int. Geod. Symp. Satell. Doppler Position., **1983**: pp. 1213–1231.

[44] W.G. Melbourne, The case for ranging in GPS-based geodetic systems, in: Proc. First Int. Symp. Precise Position. with Glob. Position. Syst., US Department of Commerce Rockville, Maryland, **1985**: pp. 373–386.

[45] G. Wübbena, Software developments for geodetic positioning with GPS using TI 4100 code and carrier measurements, in: Proc. First Int. Symp. Precise Position with GPS, Rockville, Maryl., **1985**: pp. 403–412.

[46] C. Xu, Y. Zhu, X. Xu, J. Kong, Y. Yao, J. Shi, X. Li, Regional Tropospheric Correction Model from GNSS–Saastamoinen–GPT2w Data for Zhejiang Province, Atmosphere (Basel). 14 (**2023**) 815.

[47] S.G. Park, D.J. Cho, C. Park, Carrier Phase Based Navigation Algorithm Design Using Carrier Phase Statistics in the Weak Signal Environment, J. Positioning, Navig. Timing. 1 (**2012**) 7–14.

[48] J. Klobuchar, Ionospheric Time-Delay Algorithm for Single-Frequency GPS Users, IEEE Trans. Aerosp. Electron. Syst. AES-23 (**1987**) 325–331.

[49] N. Wang, Y. Yuan, Z. Li, X. Huo, Improvement of Klobuchar model for GNSS single-frequency ionospheric delay corrections, Adv. Sp. Res. 57 (**2016**) 1555–1569.

[50] Y. Yuan, X. Huo, J. Ou, K. Zhang, Y. Chai, D. Wen, R. Grenfell, Refining the Klobuchar ionospheric coefficients based on GPS observations, IEEE Trans. Aerosp. Electron. Syst. 44 (**2008**) 1498–1510.

[51] A. Leick, L. Rapoport, D. Tatarnikov, GPS Satellite Surveying, John Wiley & Sons, Inc, Hoboken, NJ, USA, **2015**.

[52] B. Bidikar, G. Sasibhushana Rao, L. Ganesh, M. Santosh Kumar, Satellite Clock Error and Orbital Solution Error Estimation for Precise Navigation Applications, Positioning. 05 (**2014**) 22–26.

[53] H. Ge, B. Li, T. Wu, S. Jiang, Prediction models of GNSS satellite clock errors:

Evaluation and application in PPP, Adv. Sp. Res. 68 (**2021**) 2470–2487.

[54] K. Maciuk, Determination of GNSS receiver elevation-dependent clock bias accuracy, Measurement. 168 (**2021**) 108336.

[55] M.S. Braasch, Multipath, Springer Handb. Glob. Navig. Satell. Syst. (**2017**) 443–468.

[56] T. Kos, I. Markezic, J. Pokrajcic, Effects of multipath reception on GPS positioning performance, in: Proc. ELMAR-2010, IEEE, **2010**: pp. 399–402.

[57] L. Urquhart, Analysis of multi-frequency carrier phase linear combinations for GNSS, (**2023**).

[58] M. Rabah, G. El-Fiky, A. Mousa, A. Elhattab, A. Tealeb, DEVELOPING A REAL-TIME APPROACH FOR DETECTING AND REPAIRING CYCLE-SLIPS IN DIFFERENCE MODE BASED UPON IONOSPHERIC RESIDUALS AND EXTRA WIDE-LANING TECHNIQUE COMBINATION, (**2002**).

[59] Z. Liu, A new automated cycle slip detection and repair method for a single dual-frequency GPS receiver, J. Geod. 85 (**2011**) 171–183.

[60] A. Yastrebova, M. Höyhtyä, S. Boumard, E.S. Lohan, A. Ometov, Positioning in the Arctic region: State-of-the-art and future perspectives, IEEE Access. 9 (**2021**) 53964–53978.

[61] H. Lichtenegger, B. Hofmann-Wellenhof, GPS-Data Preprocessing for Cycle-Slip Detection, (**1990**) 57–68.

[62] G. Blewitt, GPS data processing methodology: From theory to applications, in: GPS Geod., Springer, **1998**: pp. 231–270.

[63] Z. Dai, MATLAB software for GPS cycle-slip processing, GPS Solut. 16 (**2012**) 267–272.

[64] Q. Chen, H. Chen, W. Jiang, X. Zhou, P. Yuan, A New Cycle Slip Detection and Repair Method for Single-Frequency GNSS Data, J. Navig. 71 (2018) 1492–1510.

[65] W. Liang, Z. Liao, W. Fu, B. Pan, A Cycle slip Detection Method Based on Single-frequency Dual-mode, in: 2022 IEEE 12th Symp. Comput. Appl. Ind. Electron., IEEE, **2022**: pp. 38–43.

[66] P. Silva, Cycle slip detection and correction for precise point positioning, in: Proc. Inst. Navig. ION GNSS, **2013**: p. 47.

[67] G. Blewitt, An automatic editing algorithm for GPS data, Geophys. Res. Let. 17 (**1990**) 199–202.

[68] C. Cai, Z. Liu, P. Xia, W. Dai, Cycle slip detection and repair for undifferenced GPS observations under high ionospheric activity, GPS Solut. 17 (**2013**) 247–260.

[69] L. Van Hieu, V.G. Ferreira, X. He, X. Tang, Study on cycle-slip detection and repair methods for a single dual-frequency global positioning system (GPS) receiver, Bol. Ciências Geodésicas. 20 (**2014**) 984–1004.

[70] M. Deo, A. El-Mowafy, A. Professor, Cycle Slip and Clock Jump Repair with Multi-Frequency Multi-Constellation GNSS data for Precise Point Positioning, in: **2015.**

[71] S. Chandra Bharadwaj, A. Vidyarthi, Process of Detection, Determination and

Correction Cycle Slip Error:A Review, in: 2020 6th Int. Conf. Signal Process. Commun., IEEE, **2020**: pp. 331–336.

[72] H.-J. Eueler, C.C. Goad, On optimal filtering of GPS dual frequency observations without using orbit information, Bull. Géodésique. 65 (**1991**) 130–143.

[73] B. Bahadur, M. Nohutcu, PPPH: a MATLAB-based software for multi-GNSS precise point positioning analysis, GPS Solut. 22 (**2018**) 113.

[74] O. Montenbruck, A. Hauschild, P. Steigenberger, U. Hugentobler, P. Teunissen, S. Nakamura, Initial assessment of the COMPASS/BeiDou-2 regional navigation satellite system, GPS Solut. 17 (**2013**) 211–222.

[75] Y. Feng, GNSS three carrier ambiguity resolution using ionosphere-reduced virtual signals, J. Geod. 82 (**2008**) 847–862.

[76] X. Gu, B. Zhu, Detection and correction of cycle slip in triple-frequency GNSS positioning, Ieee Access. 5 (**2017**) 12584–12595.

[77] X. Feng, C. Liu, C. Liu, L. Xu, Y. Du, The detection and repair of cycle-slip based on the combination of beidou triple-frequency observations, Lect. Notes Electr. Eng. 439 (**2017**) 467–479.

[78] X. Fan, R. Tian, X. Dong, W. Shuai, Y. Fan, Cycle slip detection and repair for BeiDou-3 triple-frequency signals, Int. J. Adv. Robot. Syst. 17 (**2020**) 172988142092640.

[79] S.J. Chapman, MATLAB programming for engineers, Cengage Learning, 2015.

[80] A.E. Ragheb, A. Zekry, M. Elhabiby, GNSS Cycle Slip Detection and Estimation Using LSTM-based Autoencoder Model., MEJ. Mansoura Eng. J. 46 (**2021**) 31–40.

[81] Y. Hatanaka, A compression format and tools for GNSS observation data, (2008).

[82] J. Matzka, C. Stolle, Y. Yamazaki, O. Bronkalla, A. Morschhauser, The Geomagnetic *Kp* Index and Derived Indices of Geomagnetic Activity, Sp. Weather. 19 (**2021**).

[83] C. Cai, C. He, R. Santerre, L. Pan, X. Cui, J. Zhu, A comparative analysis of measurement noise and multipath for four constellations: GPS, BeiDou, GLONASS and Galileo, Surv. Rev. 48 (**2016**) 287–295.

[84] H. Zhang, S. Ji, Z. Wang, W. Chen, Detailed assessment of GNSS observation noise based using zero baseline data, Adv. Sp. Res. 62 (**2018**) 2454–2466.